

The shapes of spiral arms in the S⁴G survey and their connection with stellar bars

S. Díaz-García^{1,2}, H. Salo³, J. H. Knapen^{1,2,4}, and M. Herrera-Endoqui⁵

¹ Instituto de Astrofísica de Canarias, E-38205, La Laguna, Tenerife, Spain
e-mail: simondiazgar@gmail.com

² Departamento de Astrofísica, Universidad de La Laguna, E-38205, La Laguna, Tenerife, Spain

³ Astronomy Research Unit, University of Oulu, FI-90014 Finland

⁴ Astrophysics Research Institute, Liverpool John Moores University, IC2, Liverpool Science Park, 146 Brownlow Hill, Liverpool, L3 5RF, UK

⁵ Instituto de Astronomía, Universidad Nacional Autónoma de México, Apdo. Postal 877, Ensenada, Baja California 22800, México

Received 31 May 2019 / Accepted 12 August 2019

ABSTRACT

Context. Spiral galaxies are very common in the local Universe, but their formation, evolution, and interplay with bars remain poorly understood after more than a century of astronomical research on the topic.

Aims. We use a sample of 391 nearby galaxies from the S⁴G survey to characterise the winding angle and amplitude of spiral arms as a function of disc properties, such as bar strength, in all kinds of spirals (grand-design, multi-armed, and flocculent).

Methods. We derived global pitch angles in 3.6 μm de-projected images from i) average measurements of individual logarithmic spiral segments, and ii) for a subsample of 32 galaxies, from 2-D Fourier analyses. The strength of spirals was quantified from the tangential-to-radial force ratio and from the normalised $m = 2$ Fourier density amplitudes.

Results. In galaxies with more than one measured logarithmic segment, the spiral pitch angle varies on average by $\sim 10^\circ$ between segments, but by up to $\gtrsim 15 - 20^\circ$. The distribution of the global pitch angle versus Hubble type (T) is very similar for barred and non-barred galaxies when $1 \lesssim T \lesssim 5$. Most spiral galaxies ($> 90\%$) are barred for $T > 5$. The pitch angle is not correlated with bar strength, and only weakly with spiral strength. The amplitude of spirals is correlated with bar strength (and less tightly, with bar length) for all types of spirals. The mean pitch angle is hardly correlated with the mass of the supermassive black hole (estimated from central stellar velocity dispersion), with central stellar mass concentration, or with shear, questioning previous results in the literature using smaller samples.

Conclusions. We do not find observational evidence that spiral arms are driven by stellar bars or by invariant manifolds. Most likely, discs that are prone to the development of strong bars are also reactive to the formation of prominent spirals, explaining the observed coupling between bar and spiral amplitudes.

Key words. galaxies: structure - galaxies: evolution - galaxies: statistics - galaxies: spiral - galaxies: fundamental parameters - galaxies: photometry

1. Introduction

The most conspicuous stellar structures of spiral galaxies are the arms that sweep out from the centre of the disc in unbarred galaxies, or from near the ends of the stellar bar. Spiral arms are sites rich in gas with intense star formation, H II regions, and dust (e.g. Schweizer 1976; Elmegreen et al. 2011). This makes them more prominent in blue bands of the spectrum, but their backbone is typically composed of old stars (e.g. Elmegreen 1981; Elmegreen & Elmegreen 1989; Knapen & Beckman 1996; Eskridge et al. 2002). Roughly two thirds of all massive galaxies are spirals (e.g. Lintott et al. 2011; Willett et al. 2013).

There are three main types of spiral arms (e.g. Elmegreen 1990): grand-design, flocculent, and multi-armed. The fraction of each of these classes in disc galaxies is $\sim 18\%$, $\sim 50\%$, and $\sim 32\%$, respectively, based on the morphological classifications made by Elmegreen et al. (2011) and Buta et al. (2015) to the Spitzer Survey of Stellar Structure in Galaxies (S⁴G; Sheth et al. 2010), that comprises over 2000 nearby galaxies. Grand-design galaxies (Lin & Shu 1966) are characterised by two long and well-defined arms. Flocculent spirals (Elmegreen 1981) present

short and fragmented spiral arm sections. They are more common in faint galaxies (Elmegreen & Elmegreen 1985). The fairly symmetric multi-armed spirals constitute a category between grand-design and flocculent, closer to the former, characterised by a central two-armed pattern that develops long ramifications in the outer parts of the optical disc. In this work we analyse the shapes of these three types of spirals in the S⁴G survey.

How spiral arms are formed in galactic discs remains a matter of debate. One of the most widely accepted explanations of the formation and maintenance of spirals is the density wave theory (Lin & Shu 1964). The arms are considered as density waves that rotate with a radius-independent angular speed through the stars and gas in a shearing, differentially rotating galactic disc. In this scenario, the stars in the inner parts of the disc rotate faster than the spiral and can overtake it, whereas in the outer parts they lag with respect to the spiral pattern.

Spirals might also be tidally triggered in interactions with companion galaxies (Kormendy & Norman 1979), as it is the case of the Whirlpool Galaxy (or M51) (see e.g. Salo & Laurikainen 2000a; Watkins et al. 2015, and references therein), the

first identified spiral nebula in history (Rosse 1850) using the *Leviathan of Parsonstown* telescope (1.8 m aperture).

In the swing amplification mechanism (Goldreich & Lynden-Bell 1965a,b; Toomre 1981), shear and self-gravity transform initially leading waves into trailing ones, so that the wave is amplified when the stabilising effects of random motions are negligible. A constraint on the theory of the formation of spirals is the number of arms expected by swing amplification. D’Onghia (2015) showed that the total number of spiral arms anticorrelates with the disc-to-total mass fraction at 2.2 disc scalelengths: submaximal discs are expected to be multi-armed galaxies. High resolution N -body simulations by Fujii et al. (2018) confirm that the disc-mass fraction controls the number of spirals.

Grand-design spiral arms and the symmetric inner parts of multi-armed galaxies have been interpreted as long-lived spiral density waves, while flocculent galaxies and the outer parts of multi-armed galaxies have been associated to random local gravitational instabilities in the disc, swing amplified into transient spiral arms (e.g. Elmegreen et al. 2011, and references therein). According to numerical models (e.g. Sellwood 2011, and references therein), the spiral arms in flocculent galaxies are short-lived (of the order of ~ 100 Myr), whereas grand-design spirals exhibit arms that last longer (~ 1 Gyr). High-resolution N -body simulations by D’Onghia et al. (2013) showed that ragged spiral structure can survive long after the original perturbing influence has been removed.

How tightly wound the spiral arms can be quantified by measuring the pitch angle (Binney & Tremaine 1987), defined as the angle subtended by the tangent to the spiral arm, relative to the tangent to a circle at a point at a given galactocentric radius. By definition, it lies between -90° and 90° . In theoretical modelling, positive (negative) pitch angles indicate trailing (leading) pattern with respect to rotation.

The pitch angle is not necessarily constant, regardless of the class of the spiral arms (e.g. Kennicutt 1981). It has been claimed that pitch angles depend on the central mass concentration and atomic gas density (e.g. Kennicutt 1981; Block et al. 1994; Davis et al. 2015; Yu & Ho 2019), on the galactic shear rate (e.g. Seigar et al. 2006; Grand et al. 2013), or on the steepness of the rotation curves (Seigar et al. 2005, 2014): spiral arms have been found to be more open in galaxies with rising rotation curves, whereas those with falling rotation curves are generally tightly wound. Recent work by Davis et al. (2017) reports a very tight scaling relation between the mass of the central supermassive black hole and the spiral pitch angle which, if true, hints at a surprisingly intimate link between the large-scale structure of discs and the mass in the nucleus (see also Seigar et al. 2008; Berrier et al. 2013).

Spiral arms are known to contribute to the rearrangement of gas that leads to the formation of disc-like bulges (e.g. Kormendy & Kennicutt 2004). This makes them important agents for the secular evolution of disc galaxies, a process in which bars also play a fundamental role. Whether spirals are bar-driven or not has been debated over the past decades, ever since Kormendy & Norman (1979) suggested that stellar bars can lead the formation of spiral density waves. The latter has been mainly tested from the correlations between gravitational torques and density amplitudes associated to bars and the spirals (e.g. Seigar et al. 2003; Block et al. 2004; Buta et al. 2005, 2009; Durbala et al. 2009; Salo et al. 2010).

A strong coupling between bars and spirals is also expected from the manifold theory, which is a relatively new paradigm for the formation of spirals and rings (e.g. Romero-Gómez et al. 2006; Patsis 2006; Voglis et al. 2006; Romero-Gómez et al.

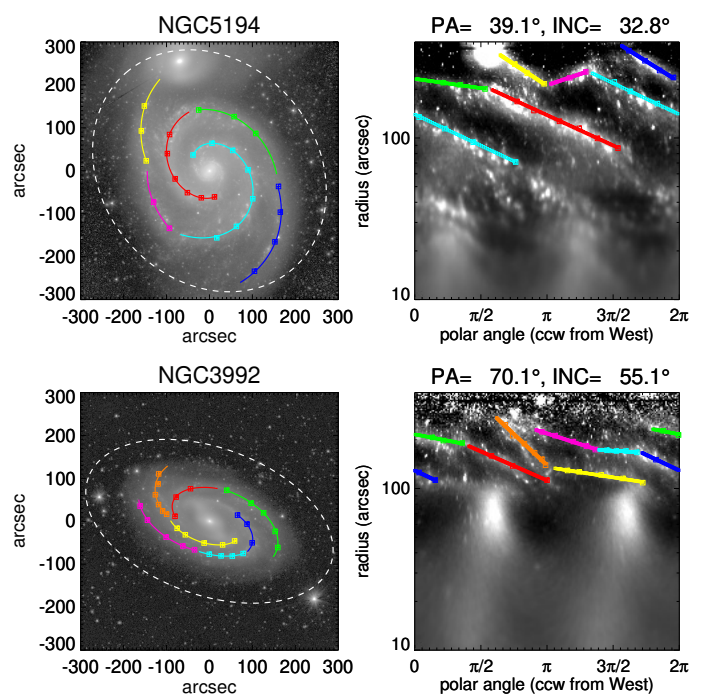


Fig. 1. 3.6 μm image of NGC 5194 (*upper panels*) and NGC 3992 (*lower panels*) in sky plane (*left*), with fitted spiral arm segments, and logarithmic polar plot of the same galaxies de-projected to the disc plane (*right*). Images and measurements are taken from Herrera-Endoqui et al. (2015).

2007; Athanassoula et al. 2009b). Numerical simulations show that galactic material gets confined in tubes (invariant manifolds) that extend from the two unstable Lagrangian points at the end of the bar (L_1 and L_2). This theory predicts a dependence of the pitch angle of spirals on the bar perturbation strength (Athanassoula et al. 2009a).

The main goals of this paper are i) to reassess the existence of scaling relations involving the pitch angle of the arms in the S^4G , ii) to analyse the coupling between the amplitudes of bars and spiral arms in all kinds of spirals galaxies with unprecedented sample size, iii) to test the predicted correlation between bar strength and pitch angle, and iv) to check if there is any difference in the distribution of the pitch angles for barred and non-barred galaxies.

The paper is organised as follows: in Sect. 2 we present the sample and the data used in this work. In Sect. 3 and 4 we explain our methodology to derive the global pitch angle of the galaxies as well as the strength of spirals and bars. In Sect. 5 we study the distribution of the pitch angle across the Hubble sequence, as well as the distribution of spiral types and bar frequency in our sample versus T -type. In Sect. 6 we assess the radial variation of the pitch angle, in Sect. 7 we test whether the pitch angle and amplitude of spirals are controlled by the strength of the bar, and in Sect. 8 we analyse the dependence of the pitch angle of the spirals on the central stellar mass concentration and on the mass of the central supermassive black hole. In Sect. 9 we discuss the properties of spiral arms, their dependence on disc fundamental parameters, and their hypothetical coupling with bars. Sect. 10 summarises the most important results of this work.

2. Data and sample selection

2.1. The S⁴G survey

The S⁴G survey (Sheth et al. 2010) consists of 2352 nearby galaxies (distance $\lesssim 40$ Mpc) observed in the $3.6\ \mu\text{m}$ and $4.5\ \mu\text{m}$ bands with the InfraRed Array Camera (IRAC; Fazio et al. 2004) installed on board the *Spitzer Space Telescope* (Werner et al. 2004). Data taken from HyperLEDA were used to define the S⁴G sample, which is composed of bright and large galaxies (extinction-corrected total blue magnitude $m_{B,\text{corr}} < 15.5$ mag and blue light isophotal angular diameter $D_{25} > 1'$) located away from the Milky Way plane (Galactic latitude $|b| > 30^\circ$).

The S⁴G is not complete in any quantitative sense, but it is comprised of galaxies of all Hubble types (T) with stellar masses spanning ~ 5 orders of magnitude. Due to selection based on H I recessional velocities, it is deficient in gas-poor early-type galaxies: this is not a serious drawback for the current study because we are not interested in S0s, that lack spiral arms. In addition, the S⁴G missed around 400 late-type galaxies without 21 cm systemic velocity measurements listed in HyperLEDA: we are currently obtaining i -band photometry with ground-based telescopes for the $\sim 50\%$ of those galaxies that lack high-resolution deep near-IR and optical archival imaging. The current work is based on the original S⁴G.

Bulge-to-total mass ratios (B/T) and disc scale-lengths (h_R) of S⁴G galaxies are available from the 2-D photometric decomposition models by Salo et al. (2015). We take the $3.6\ \mu\text{m}$ isophotal radii at the surface brightness $25.5\ \text{mag arcsec}^{-2}$ ($R_{25.5}$) from Muñoz-Mateos et al. (2015).

2.2. Morphological classification

We use the morphological classification of the galaxies in the S⁴G sample made by Buta et al. (2015), that includes families (SB, SAB, SAB, SAB, SA) and the revised Hubble stages (T). We also use arm classes from Buta et al. (2015) and Elmegreen et al. (2011).

2.3. Pitch angles of spiral arms

Herrera-Endoqui et al. (2015) measured the pitch angles of spiral arm segments in S⁴G galaxies using $3.6\ \mu\text{m}$ photometry, which are analysed in this paper. Only measurements with "ok" quality flags ($= 1 - 2$) are used.

Herrera-Endoqui et al. (2015) identified the different spiral segments in unsharp-masked images, created by dividing the original images by their smoothed versions. In unsharp-masked images one can easily identify subtle galactic structures that appear against a bright and diffuse background. These images were displayed in different scales to make the spiral arms stand out. They visually marked points tracing the spiral segments (and thus there are uncertainties in the parametrisation associated to human errors). Then, they performed a linear fit in the disc plane using polar coordinates $\log(r)$ versus θ , where logarithmic arms appear as straight lines. Thus, several measurements of the pitch angle can appear for a single galaxy, corresponding to logarithmic segments at different radial distances. In Fig. 1 we illustrate these measurements for M 51 and NGC 3992. For further details, the reader is referred to Herrera-Endoqui et al. (2015).

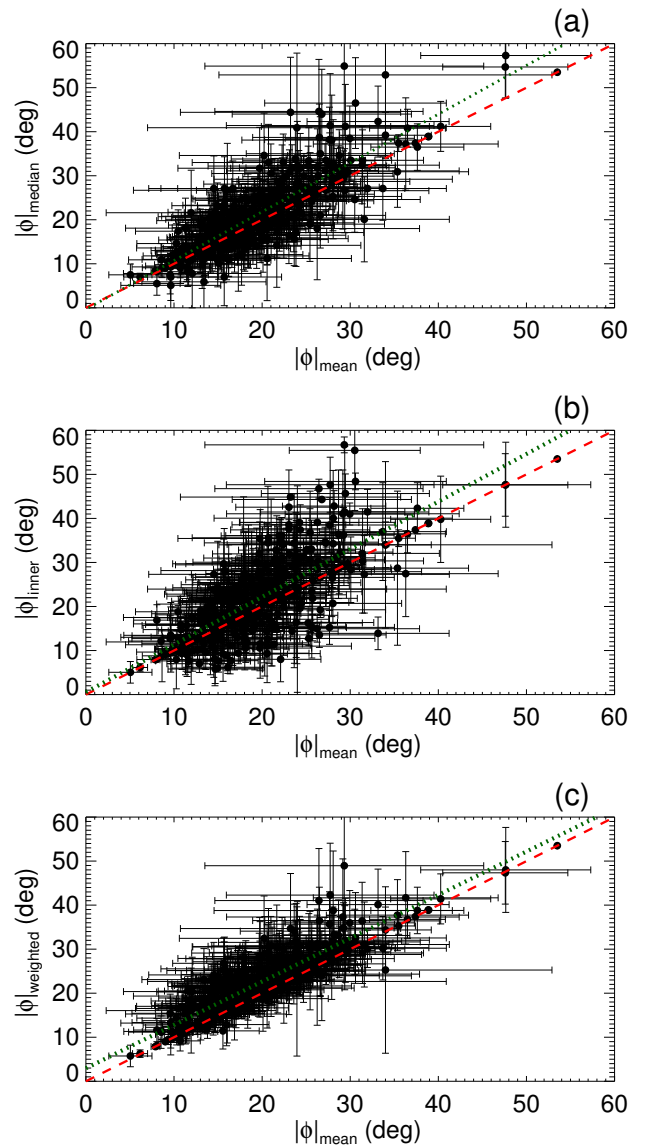


Fig. 2. Comparison between mean and a) median pitch angle, b) mean of the innermost logarithmic segments, and c) mean weighted by the arc length of the arms. The $y = x$ straight line is shown in red, and the dotted green line shows the linear fit to the cloud of points. Error bars indicate the standard deviation of the mean calculated from the segments fitted in each galaxy.

2.4. Sample of not-highly inclined spiral galaxies

For this study, we use a sample of 391 galaxies with inclinations lower than 65° (according to Salo et al. 2015), with reliable measurements of pitch angles of individual spiral segments¹ (from Herrera-Endoqui et al. 2015), and classified spiral types (from Buta et al. 2015). Of these, 269 galaxies are barred (i.e. classified as SB, SAB, SAB, or SAB), 76 are grand-design, 157 are multi-armed, and 158 host flocculent spirals.

¹ Only six galaxies in our sample (1.5%) have a single measurement of the pitch angle, 74 galaxies (18.9%) have two measured logarithmic segments, 86 (22.0%) have three, 105 (26.9%) have four, 58 (14.8%) have five, and 62 galaxies (15.9%) have more than five (with two cases having a maximum of nine segments).

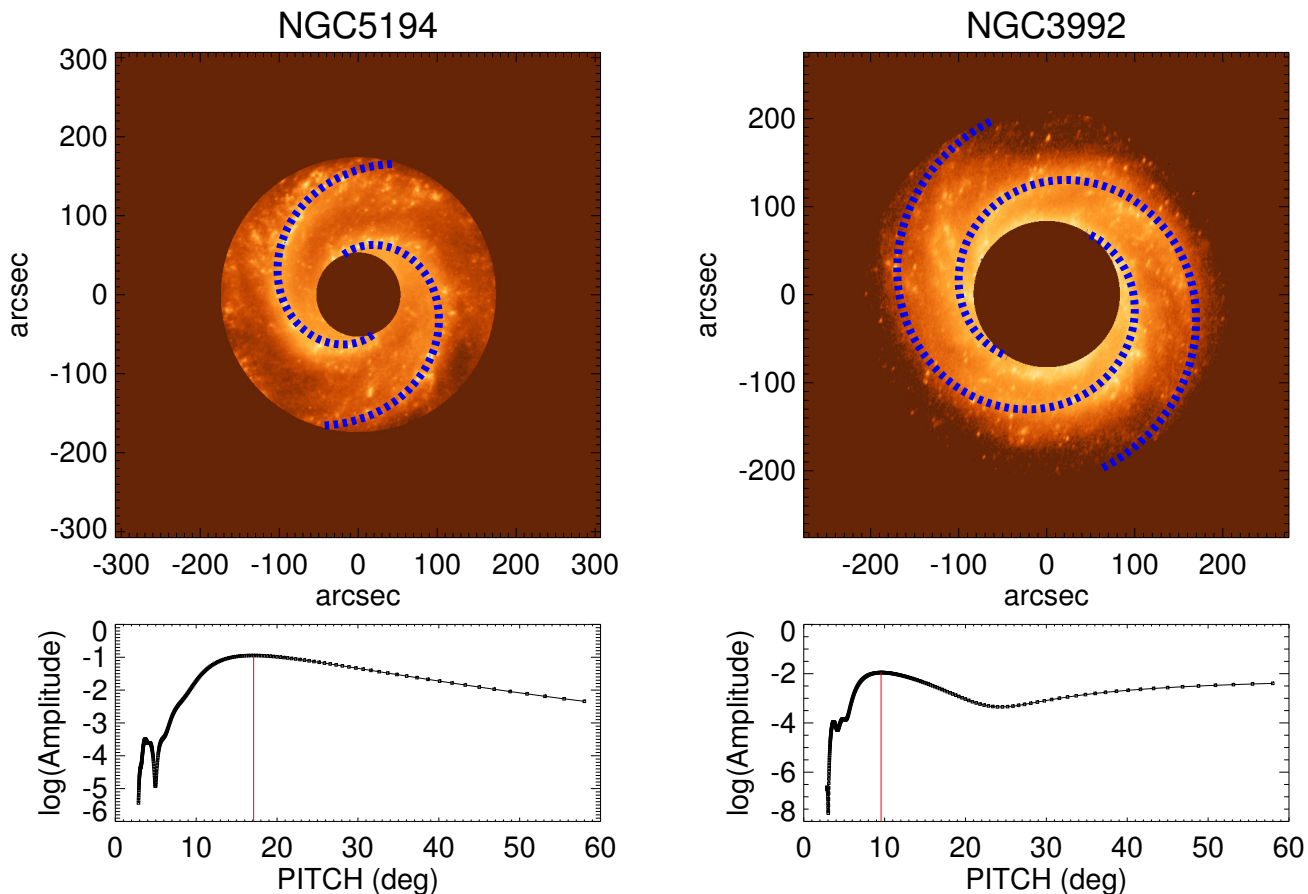


Fig. 3. *Upper panels:* Logarithmic fit to the spiral arms in the de-projected $3.6 \mu\text{m}$ image of NGC 5194 (*left*) (18-23 $\mu_{3.6\mu\text{m}}(AB)$ magnitude scale) and NGC 3992 (*right*) (21-25 $\mu_{3.6\mu\text{m}}(AB)$ magnitude scale), using 2-D Fourier transform spectral analysis (see text). *Lower panels:* Logarithm of the $m = 2$ Fourier amplitude as a function of the pitch angle for the two galaxies shown above. The vertical line denotes the maximum value, that determines the global pitch angle assigned to the galaxy.

3. Global pitch angles of spirals

In order to parameterise the winding of the spirals, so that it can be studied as a function of galaxy parameters, we need to determine the global pitch angle of the galaxies (ϕ hereafter). We will assume that the spiral segments are all trailing, and will therefore treat ϕ always as a positive quantity. Also, we do not care whether the apparent spiral opening angles in sky are clockwise or counter-clockwise (the winding direction of arms in spiral galaxies is distributed at random in the local Universe, see e.g. Hayes et al. 2017).

3.1. Mean pitch angle of individual logarithmic segments

We first calculate the mean and median of the absolute value of the pitch angle measurements of logarithmic segments ($|\phi|_{\text{mean}}$ and $|\phi|_{\text{median}}$, respectively). Uncertainties in the determination of $|\phi|$ are estimated by computing the standard deviation of the mean of the measurements of different segments. We compare $|\phi|_{\text{mean}}$ and $|\phi|_{\text{median}}$ in the top panel of Fig. 2: the mean absolute difference is $3.49^\circ \pm 0.17^\circ$.

We also calculate the mean of the absolute value of the two innermost spiral segments (or one for the 6 galaxies with a single measurement), $|\phi|_{\text{inner}}$, to trace the pitch angle in the central parts of galaxies and in the vicinity of the bar. The mean absolute dif-

ference between $|\phi|_{\text{mean}}$ and $|\phi|_{\text{inner}}$ is $4.70^\circ \pm 0.24^\circ$ (central panel of Fig. 2).

In addition, we propose a measurement of the global pitch angle of disc galaxies by weighting the average by the relative arc length of the logarithmic segments, $|\phi|_{\text{weighted}}$. The equation for a logarithmic spiral in polar coordinates (r, θ) can be written as follows (e.g. Lin & Shu 1964; Elmegreen & Elmegreen 1987):

$$r(\theta) = R \cdot e^{\theta \tan \phi}, \quad (1)$$

where $\theta = 0$ at $r = R \in \mathbb{R}$ and ϕ refers to the pitch angle. For a given galaxy, the arc length (s) of the logarithmic spiral segment i extending between (r_i, θ_i) and (r'_i, θ'_i) with pitch angle ϕ_i can be approximated as (e.g. Zwicker 1963):

$$s_i = \int_{\theta_i}^{\theta'_i} \sqrt{r^2 + (dr/d\theta)^2} \cdot d\theta \approx |r'_i - r_i| \cdot \frac{\sqrt{1 + \tan^2 \phi_i}}{\tan |\phi_i|}, \quad (2)$$

and then

$$|\phi|_{\text{weighted}} = \frac{1}{S} \sum_{i=1}^n |\phi_i| \cdot s_i, \quad (3)$$

where n is the total number of measured spiral arm segments, and $S = \sum_{i=1}^n s_i$. This is in practice very close to weighting with the

relative radial extent of the spirals segments over which measurements were performed. The mean absolute difference between $|\phi|_{\text{mean}}$ and $|\phi|_{\text{weighted}}$ is $2.9^\circ \pm 0.14^\circ$ (see bottom panel of Fig. 2).

The global pitch angles of each of the galaxies in our sample² are listed in Table A.1. Hereafter, we will use all proxies of $|\phi|$ for the analysis in this paper.

3.2. Pitch angles from 2-D Fourier analysis

In order to test the sensitivity of the pitch angle determination to the employed methodology, we also fit the spiral structure using Fourier transform spectral analyses of the de-projected 3.6 μm images. We apply a similar method as in Puerari & Dottori (1992) and Puerari et al. (2000), who had in turn followed the approach by Kalnajs (1975) and Considere & Athanassoula (1982) (for a more sophisticated determination, see Puerari et al. 2014).

Images are decomposed into a flux-weighted superposition of m -armed logarithmic spirals of different pitch angles (see e.g. Puerari et al. 2000; Ma 2001; Davis et al. 2012), whose amplitudes are calculated as:

$$A(p, m) = \frac{1}{D} \int_{-\pi}^{+\pi} \int_{R_{\text{inner}}}^{R_{\text{outer}}} I(u, \theta) e^{-i(m\theta + pu)} du d\theta, \quad (4)$$

where $u = \ln(r)$, $I(u, \theta)$ refers to the intensity distribution in polar coordinates, the variable $p \in \mathbb{R}$ defines the pitch angle of the spiral as $\arctan(-m/p)$, $D = \int_{R_{\text{inner}}}^{R_{\text{outer}}} \int_{-\pi}^{+\pi} I(r, \theta) dr d\theta$ is the normalisation factor, and R_{inner} and R_{outer} are the limits in the radial range for the fit.

Choosing R_{inner} and R_{outer} is the greatest source of human error for the fit (Davis et al. 2012). Where available, we use the minimum and maximum radii where Herrera-Endoqui et al. (2015) fit the logarithmic segments. By doing so, the central bulge is excluded from the fit and the outer radius reaches the limit of the arms in the images. Whenever clear outer arm breaks are seen (e.g. M51), we limit the fit to the inner segments. When the galaxies are barred, the masked region has a radius $\geq r_{\text{bar}}$ (at times, we mask regions well beyond the bar radius to avoid short spurious spiral segments that can contaminate the fit). Occasionally, when the spiral pattern presents multiple breaks, we limit the fit to the range $[r_{\text{bar}}, 2r_{\text{bar}}]$. By visual inspection of the images, we also choose the range of pitch angles for the fit (positive or negative depending on winding direction).

We use the limits $p \in [-50, 50]$ and step-size (0.25) advocated by Puerari et al. (2000). Finally, for $m = 2$, we select the value of p with the highest amplitude, which defines the final pitch angle of the spiral arms, called as $|\phi|_{\text{Fourier}}$ (for NGC 5054 we used $m = 3$ to fit the three arms). Examples of the resulting fits for M51 and NGC 3992 are shown in Fig. 3.

We could reliably identify the maximum of the pitch angle p associated to the spiral pattern ($|\phi|_{\text{Fourier}}$) for a subsample of 32 of the galaxies in our master sample ($\sim 10\%$), of which most (25) are barred (i.e. they are not SA) according to Buta et al. (2015). In Table 1 we list the measurements of the pitch angle using the 2-D Fourier method. We also indicate the radial range where the fit was done. A rough estimate of the uncertainties in $|\phi|_{\text{Fourier}}$ is calculated by reducing by an arbitrary 20% the radial range for the fit: an offset of $(R_{\text{outer}} - R_{\text{inner}})/10$ is added (subtracted) to R_{inner} (from R_{outer}).

² Preliminary analysis of these measurements (and the properties of barred and non-barred galaxies) using unsupervised machine learning techniques (self-organising maps) has been done by Díaz-García et al. (2019).

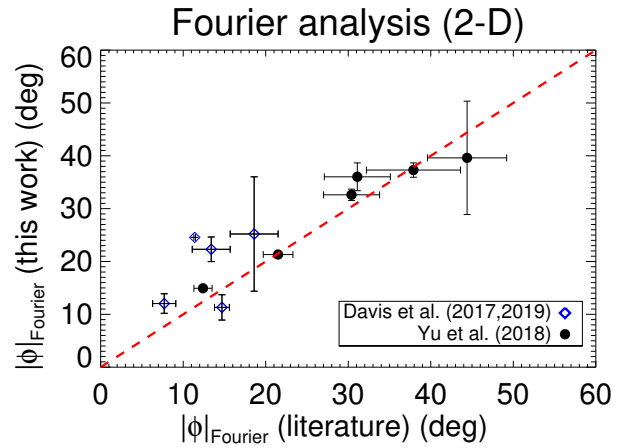


Fig. 4. For a subsample of 11 S⁴G galaxies, comparison between the pitch angles obtained in this work and in the literature (see legend) applying Fourier analysis (see text). The $y = x$ straight line is shown in red.

Galaxy	R_{inner} (")	R_{outer} (")	$ \phi _{\text{Fourier}}$ (°)	Error $ \phi _{\text{Fourier}}$ (°)
ESO027-001	15.9	90.0	18.1	± 2.4
IC0167	14.8	80.2	48.8	± 2.1
IC0769	12.7	68.2	14.7	± 0.4
IC2627	9.0	82.6	36.0	± 2.6
NGC2543	29.2	71.0	13.8	± 16.8
NGC2710	10.1	55.9	33.7	0.0
NGC2712	26.8	53.2	9.2	± 1.5
NGC2750	14.7	72.5	17.1	± 1.4
NGC3031	260.4	654.0	22.3	± 2.3
NGC3227	54.8	127.5	12.0	± 1.9
NGC3310	13.2	69.1	41.6	0.0
NGC3507	23.0	72.8	14.7	± 0.4
NGC3513	17.8	71.2	21.3	0.0
NGC3583	24.1	70.2	18.8	± 3.1
NGC3627	61.8	215.4	25.2	± 10.8
NGC3893	10.6	112.5	20.0	0.0
NGC3953	48.5	173.6	8.5	± 0.2
NGC3992	82.3	205.1	9.5	0.0
NGC4303	38.1	175.8	11.3	± 2.4
NGC4430	27.9	73.1	17.4	± 0.3
NGC4902	27.1	74.1	14.9	± 0.2
NGC5054	25.1	152.2	39.6	± 10.7
NGC5194	53.2	174.0	17.1	± 0.6
NGC5247	21.9	152.1	37.3	± 1.4
NGC5364	17.0	186.3	9.7	± 0.1
NGC5430	33.0	59.9	12.9	± 0.2
NGC5668	12.8	91.6	29.7	± 3.9
NGC5774	17.1	88.2	14.7	0.0
NGC5921	39.1	112.6	26.6	± 4.8
NGC5970	17.2	72.4	23.4	± 3.4
NGC7412	20.4	103.6	32.6	± 1.1
NGC7741	48.7	113.5	18.1	± 5.4

Table 1. Pitch angle of a subsample of S⁴G galaxies determined based on 2-D Fourier analysis. We also indicate the uncertainty in the measurement and the radial boundaries (in the disk plane) used for the fit.

3.3. Comparison between methods and with values in the literature

Recent work by Yu et al. (2018) characterised the pitch angle of the spiral arms in the Carnegie-Irvine Galaxy Survey (Ho et al.

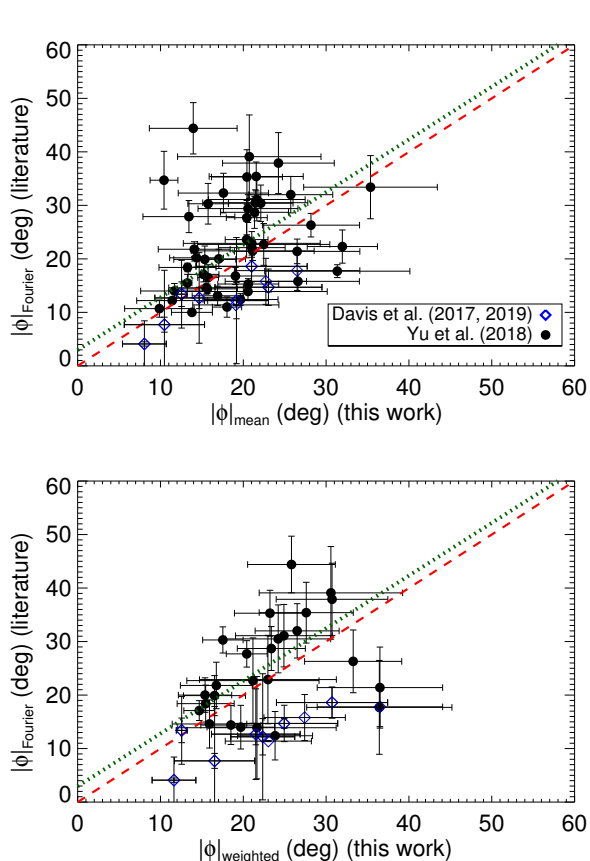


Fig. 5. Comparison between mean and weighted mean pitch angles calculated in this work, and the pitch angle obtained by Yu et al. (2018) (black) and Davis et al. (2017) (blue diamonds) via Fourier analysis (see the text). The dashed red line corresponds to the straight line $y = x$, while the dotted green line shows the linear fit to the data cloud.

2011) using Fourier methods³: there is an overlap of 49 galaxies between their survey and our sample of 391 galaxies. In addition, there are seven S⁴G galaxies from our sample with measurements available from Davis et al. (2017)⁴. Of those 56 galaxies with pitch angle measurements in the literature, we could reliably apply the Fourier method to 11 (Sect. 3.2): in Fig. 4 we show a comparison of the obtained values, showing a good agreement.

In general, there is also good agreement between the average pitch angle obtained in this work - based on the measurements of individual logarithmic segments - and the values of $|\phi|_{\text{Fourier}}$ from the literature (Fig. 5): we obtain a mean absolute difference of $3.9^\circ \pm 1.0^\circ$ and $8.4^\circ \pm 1.4^\circ$ for $|\phi|_{\text{mean}}$ and $|\phi|_{\text{weighted}}$, respectively. The scatter and outliers in the comparison are, most likely, due to the employed methodology to estimate the pitch angle.

Differences in $|\phi|$ for the two methods applied in this paper (Fourier analysis and average of the pitch angles of individual logarithmic segments) over $3.6 \mu\text{m}$ images for a subsample of 32 galaxies are shown in Fig. 6. We compare $|\phi|_{\text{Fourier}}$ with $|\phi|_{\text{mean}}$,

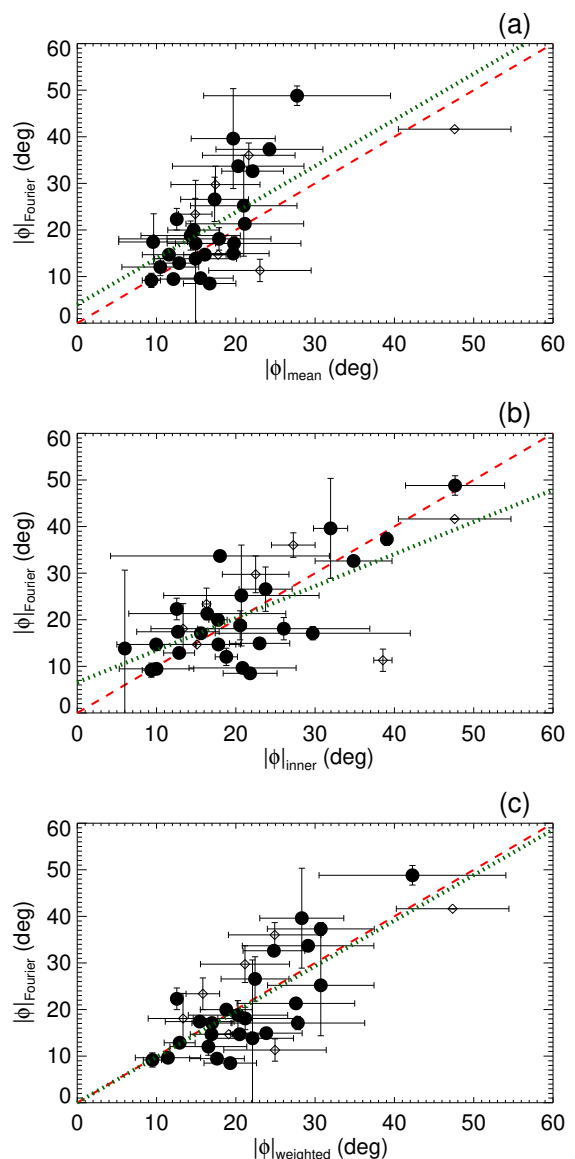


Fig. 6. For a subsample of S⁴G galaxies, comparison between the pitch angles determined with Fourier methods (from this work, see text) and a) mean pitch angle, b) inner mean pitch angles, and c) mean pitch angle weighted by the arc length of the segments. We show measurements with very reliable (= 1, filled circle) and acceptable (= 2, empty diamonds) flags in Herrera-Endoqui et al. (2015). As in Fig. 5, the red dashed line corresponds to the straight line $y = x$, while the green dotted line shows the linear fit to the cloud of points.

$|\phi|_{\text{inner}}$, and $|\phi|_{\text{weighted}}$, obtaining mean absolute differences of $6.8^\circ \pm 1.0^\circ$, $10.0^\circ \pm 2.2^\circ$, and $5.9^\circ \pm 0.7^\circ$, respectively. Discrepancies are associated to decoupled spiral modes that are not fitted with the Fourier method.

³ We note that the mean difference between the pitch angles obtained at $3.6 \mu\text{m}$ and from I -band images by Yu et al. (2018) is very small: $\approx 0.1^\circ$ for the 2-D method and $\approx 0.3^\circ$ for the 1-D method (Yu & Ho 2018).

⁴ These measurements were performed using using the software *Spirality* (Shields et al. 2015a,b), 2DFFT software (Davis et al. 2012, 2016), and compared to computer vision software (Davis & Hayes 2014).

Obtaining a single value that characterises the winding of the spirals is not straightforward, and it is sensitive to the utilised methodology and its drawbacks (see also discussion in e.g. Elmegreen et al. 1992). Given the uncertainties inherent to the various methodologies, the analysis of the possible dependence of pitch angle on bar strength (Sect. 7.1) is done based on visual measurements of $|\phi|$ as well as with the Fourier transform (using values from this work and from the literature).

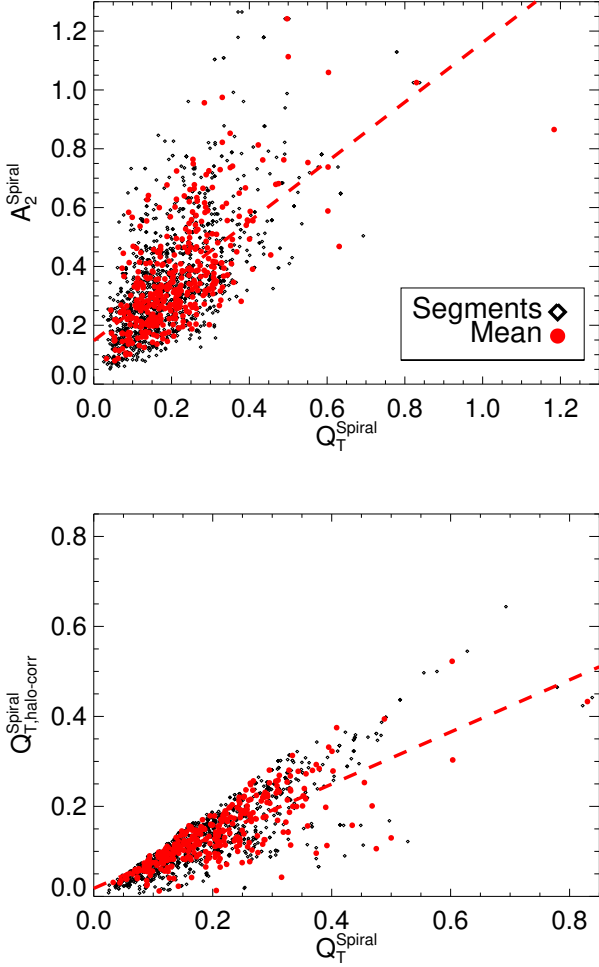


Fig. 7. Comparison between the proxies of the amplitude of the spirals used in this work (Eqs. 9, 10, and 11). We show the mean value per galaxy, and measurements over individual segments. The Spearman's rank correlation coefficients (significances) are 0.62 ($4.14 \cdot 10^{-43}$) and 0.82 (0.0) for the upper and lower panels, respectively. With a red dashed line we show the linear fit to the red data points.

4. Amplitude of non-axisymmetries

4.1. Bar strength and size

We use deprojected visual measurements of bar sizes (r_{bar}) and ellipticities (ϵ) from Herrera-Endoqui et al. (2015). We use normalised Fourier amplitudes $A_m = I_m/I_0$, where I_0 indicates the $m = 0$ surface density component, calculated by Díaz-García et al. (2016b) by applying the NIR-QB code (Salo et al. 1999; Laurikainen & Salo 2002) to $3.6 \mu\text{m}$ S⁴G images. They also derived radial profiles of tangential forces normalised to the mean radial force field (Combes & Sanders 1981):

$$Q_T(r) = \frac{\max(|F_T(r, \phi)|)}{\langle |F_R(r, \phi)| \rangle}. \quad (5)$$

The maximum of A_2 and Q_T at the bar region are used as proxies of the bar strength and named A_2^{max} and Q_b , respectively (e.g. Buta & Block 2001; Laurikainen et al. 2002, 2004).

In addition, Díaz-García et al. (2016b) obtained a first-order model of the dark matter halo rotation curve and implemented a correction on Q_T for the contribution of the halo to the radial forces ($Q_T^{\text{halo-corr}}$), following Buta et al. (2004).

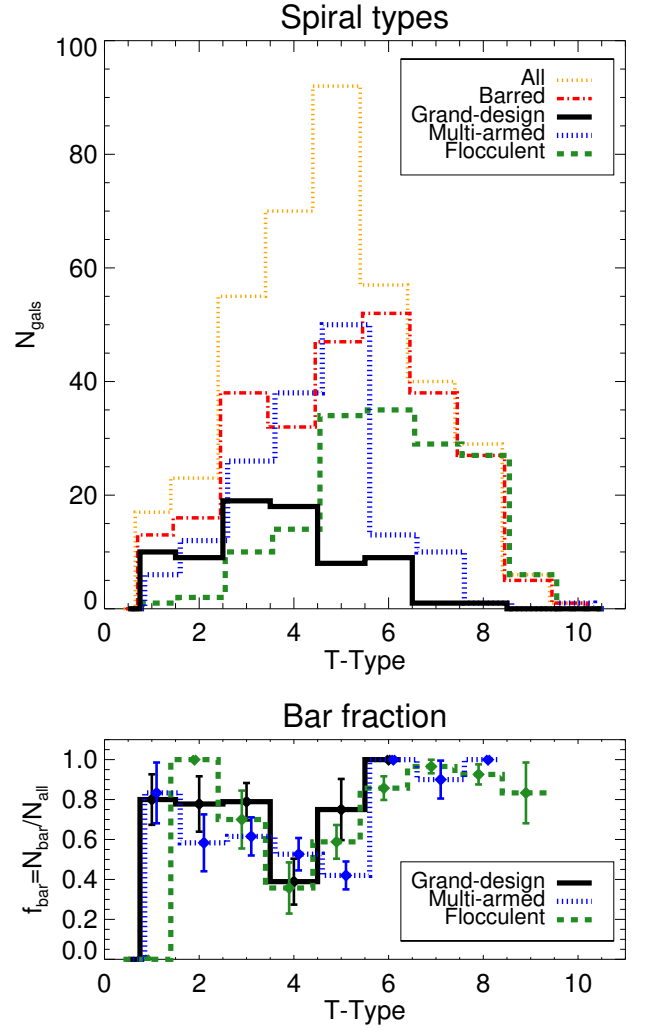


Fig. 8. *Upper panel:* Histograms of the distributions of the galaxies in our sample (showing the barred galaxies separately) and of the different arm classes (grand-design, multi-armed, and flocculent) as a function of revised Hubble stage. Small offsets (≤ 0.1) have been added in the x -axis for the sake of avoiding line overlapping. *Lower panel:* Bar fraction for the different spiral types. With vertical lines we represent binomial counting errors.

Finally, Díaz-García et al. (2016b) eliminated the spiral contribution to the bar local force by setting to zero the Fourier density amplitudes beyond the bar radius for $m > 0$, as done in Salo et al. (2010). We use the maximum at the bar region ($Q_b^{\text{bar-only}}$) as an intrinsic measure on the bar-only force.

4.2. Spiral strength

Here we define a method to calculate the strength of spiral arms in the same regions $[r_i, r_i']$ where the pitch angles of logarithmic segments were measured:

$$Q_T^{\text{Segment } i} = \max_{r_i \leq r \leq r_i'} Q_T(r), \quad (6)$$

$$Q_{T,\text{halo-corr}}^{\text{Segment } i} = \max_{r_i \leq r \leq r_i'} Q_T^{\text{halo-corr}}(r), \quad (7)$$

$$A_2^{\text{Segment } i} = \max_{r_i \leq r \leq r_i'} A_2(r). \quad (8)$$

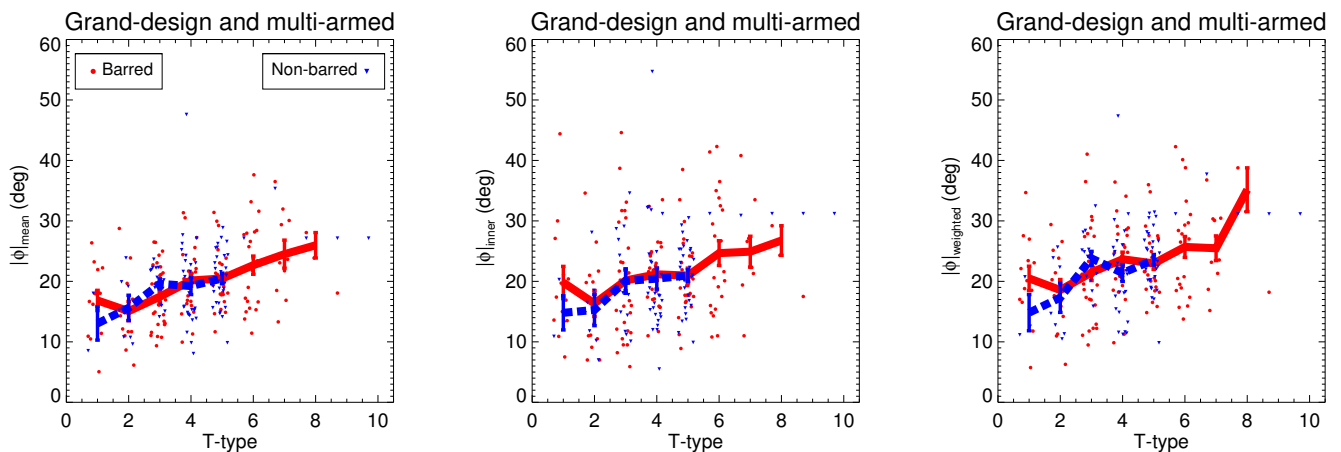


Fig. 9. Mean pitch angle (*left panel*), mean of the two innermost spiral segments (*middle panel*), and weighted mean pitch angle (*right panel*) as a function of the integer value of the revised numerical Hubble stage, for all the grand-design and multi-armed spirals in our sample. The running mean and standard deviation of the mean are shown for the barred (red) and non-barred (blue) galaxies separately, whenever more than one data point lies within the bin (i.e. when $T \leq 8$ for barred galaxies and $T \leq 5$ for non-barred ones). We have added small random offsets (≤ 0.3) to the T values in the x -axis (integers) to avoid point overlapping.

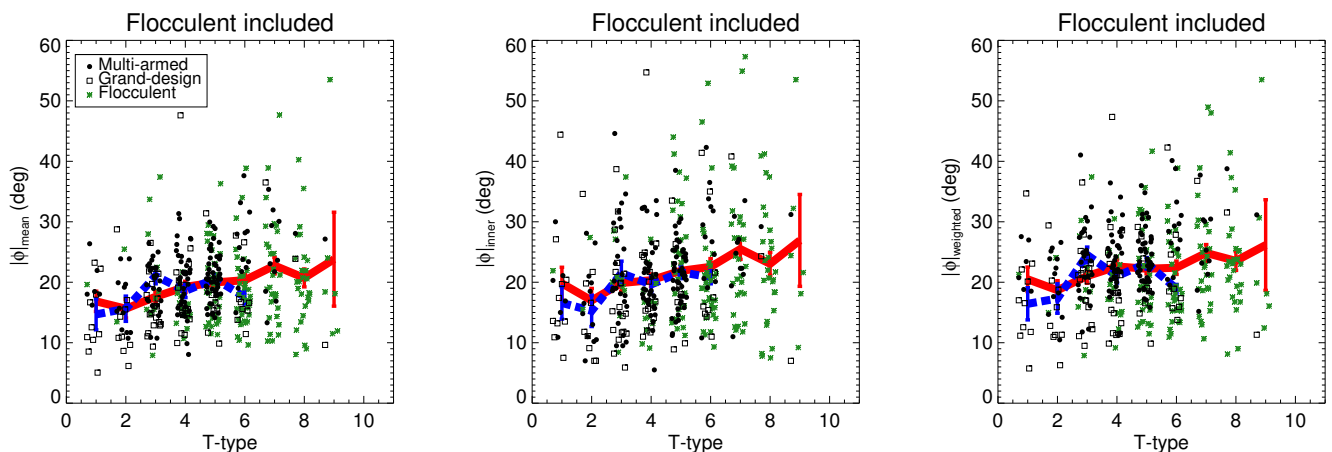


Fig. 10. As in Fig. 9, but including flocculent spirals (green). The running mean and standard deviation of the mean are shown for the galaxies that are either barred (red) or non-barred (blue, covering only the T -type range $1 \leq T \leq 6$ where they appear).

For each galaxy, we then calculate the mean of the amplitude of the spiral segments:

$$Q_T^{\text{Spiral}} = \langle Q_T^{\text{Segment } i} \rangle_{i \in [1, n]}, \quad (9)$$

$$Q_{T, \text{halo-corr}}^{\text{Spiral}} = \langle Q_{T, \text{halo-corr}}^{\text{Segment } i} \rangle_{i \in [1, n]}, \quad (10)$$

$$A_2^{\text{Spiral}} = \langle A_2^{\text{Segment } i} \rangle_{i \in [1, n]}, \quad (11)$$

where n refers to the number of logarithmic segments fitted by Herrera-Endoqui et al. (2015). In Appendix B we also make use of the mean amplitude of the two innermost and two outermost spiral segments.

There is a clear correlation between all the proxies of the spiral strength (Fig. 7)⁵. At the radii at which these segments

⁵ Díaz-García et al. (2016b) reported a bimodality in the comparison between Q_b and A_2^{max} , which might be due to the sensitivity of Q_b to the enhanced radial forces by galactic bulges (Block et al. 2001; Laurikainen & Salo 2002; Díaz-García et al. 2016b). As a matter of fact, no bimodality is present when A_2^{Spiral} is plotted versus Q_T^{Spiral} , which are measured at a radii where the bulge dilution should be much smaller.

were measured the contribution of the dark matter halo to the overall radial force field might be significant, and thus it may be important to perform the halo correction: this explains the scatter in the comparison of $Q_T^{\text{Spiral, halo-corr}}$ versus Q_T (lower panel of Fig. 7).

5. Spiral arms across the Hubble sequence

5.1. Frequency of spiral types versus T -type

The distribution of the different arm classes as a function of the Hubble stage in our sample is shown in Fig. 8 (upper panel). Flocculent arms are mainly found among late-type spirals (peak for Scd, i.e. $T = 6$), multi-armed spirals mainly have intermediate T -types (peak for Sc, i.e. $T = 5$), while grand-design galaxies are typically early-types (peak for Sb, i.e. $T = 3$). All types of spirals are found for $3 \leq T \leq 6$.

In the lower panel of Fig. 8 we show the bar fraction (f_{bar}) for the different spiral types. f_{bar} is known to have a bimodal distribution versus T in the S⁴G, with a minimum (40-45 %) for $T \approx 4$ (Sbc galaxies) (Buta et al. 2015; Díaz-García et al.

	Sample	$T \in [0, 2)$	$T \in [2, 4)$	$T \in [4, 6)$	$T \in [6, 8)$	$T \in [8, 10]$
$ \phi _{\text{mean}}$	All	15.9 ± 1.3 (19)	17.8 ± 0.7 (80)	19.7 ± 0.4 (159)	21.2 ± 0.8 (97)	21.3 ± 1.5 (36)
	Barred	16.7 ± 1.6 (14)	17.2 ± 0.8 (55)	19.7 ± 0.6 (77)	21.4 ± 0.8 (90)	21.4 ± 1.6 (33)
	Non-barred	13.7 ± 2.2 (5)	19.1 ± 1.2 (25)	19.8 ± 0.7 (82)	19.0 ± 3.0 (7)	19.7 ± 0.7 (3)
	Grand-design	13.6 ± 1.6 (12)	15.3 ± 1.0 (27)	18.1 ± 1.5 (26)	19.7 ± 2.5 (10)	-
	Multi-armed	19.8 ± 1.5 (6)	18.5 ± 0.7 (41)	20.8 ± 0.5 (85)	25.3 ± 1.3 (23)	28.4 ± 0.3 (2)
	Flocculent	-	20.8 ± 2.5 (12)	18.7 ± 0.8 (48)	19.9 ± 1.0 (64)	20.8 ± 1.6 (33)
$ \phi _{\text{inner}}$	All	21.3 ± 2.3 (19)	19.7 ± 1.0 (80)	21.5 ± 0.7 (159)	23.5 ± 1.0 (97)	23.2 ± 1.7 (36)
	Barred	22.5 ± 3.0 (14)	18.6 ± 1.3 (55)	21.7 ± 1.1 (77)	23.9 ± 1.1 (90)	23.0 ± 1.8 (33)
	Non-barred	17.7 ± 3.2 (5)	22.0 ± 1.6 (25)	21.3 ± 1.0 (82)	19.2 ± 2.3 (7)	24.6 ± 3.3 (3)
	Grand-design	18.3 ± 3.3 (12)	16.0 ± 1.7 (27)	20.8 ± 1.9 (26)	21.9 ± 3.7 (10)	-
	Multi-armed	26.8 ± 2.5 (6)	21.1 ± 1.4 (41)	22.2 ± 1.0 (85)	27.1 ± 1.8 (23)	38.2 ± 1.8 (2)
	Flocculent	-	23.0 ± 3.0 (12)	20.7 ± 1.2 (48)	22.5 ± 1.2 (64)	22.4 ± 1.7 (33)
$ \phi _{\text{weighted}}$	All	19.2 ± 1.5 (19)	21.0 ± 0.8 (80)	22.3 ± 0.5 (159)	23.3 ± 0.8 (97)	24.1 ± 1.5 (36)
	Barred	20.5 ± 1.9 (14)	20.6 ± 1.0 (55)	22.3 ± 0.7 (77)	23.4 ± 0.9 (90)	24.2 ± 1.7 (33)
	Non-barred	15.8 ± 2.2 (5)	22.0 ± 1.3 (25)	22.3 ± 0.7 (82)	21.0 ± 2.9 (7)	22.8 ± 1.5 (3)
	Grand-design	17.4 ± 2.2 (12)	18.5 ± 1.3 (27)	19.9 ± 1.6 (26)	23.2 ± 3.1 (10)	-
	Multi-armed	22.7 ± 1.6 (6)	22.6 ± 1.0 (41)	23.9 ± 0.5 (85)	27.2 ± 1.4 (23)	35.9 ± 2.8 (2)
	Flocculent	-	21.3 ± 2.3 (12)	20.8 ± 1.0 (48)	21.8 ± 1.0 (64)	23.2 ± 1.6 (33)

Table 2. Average pitch angles (in degrees) as a function of Hubble stage. It is presented the mean, the standard deviation of the mean, and the number of galaxies within the different T -type bins. We study separately barred and non-barred galaxies, and also grand-design, multi-armed, and flocculent spirals.

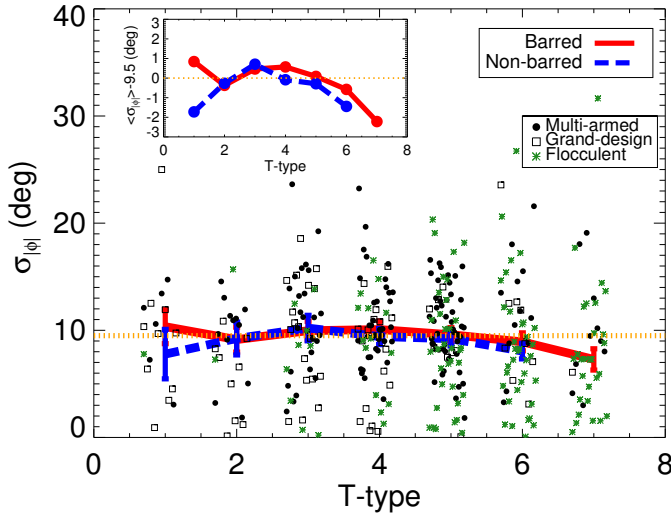


Fig. 11. As in Fig. 10, but for the standard deviation of $|\phi|$ in each of the galaxies. The lines indicate the running median per T -type for barred and non-barred galaxies, and the vertical lines correspond to the standard deviation of the mean. The horizontal orange dotted line traces the mean $\sigma_{|\phi|}$ ($\approx 9.5^\circ$). Mean residual differences with respect to this value for each T bin (typically $\lesssim 2^\circ$) are shown in the inner panel on the upper left corner.

$R_{\text{pitch}}/R_{25.5}$	$\langle \phi \rangle$ ($^\circ$) (Barred)	$\langle \phi \rangle$ ($^\circ$) (Non-barred)
0.1-0.2	22.72 ± 0.80	20.75 ± 0.70
0.2-0.3	20.91 ± 0.61	20.30 ± 0.89
0.3-0.4	18.37 ± 0.58	16.76 ± 0.82
0.4-0.5	18.08 ± 0.79	17.15 ± 0.84
0.5-0.6	18.65 ± 0.71	19.01 ± 1.03
0.6-0.7	18.50 ± 0.80	20.91 ± 1.12
0.7-0.8	20.37 ± 0.90	18.76 ± 1.16
0.8-0.9	17.73 ± 1.36	21.53 ± 2.60

Table 3. Average pitch angles as a function of radius. It is presented the mean and the standard deviation of the mean in different radial ranges, normalized by the isophotal radii at the surface brightness $25.5 \text{ mag arcsec}^{-2}$ in the $3.6 \mu\text{m}$ images ($R_{25.5}$). We study separately barred and non-barred galaxies.

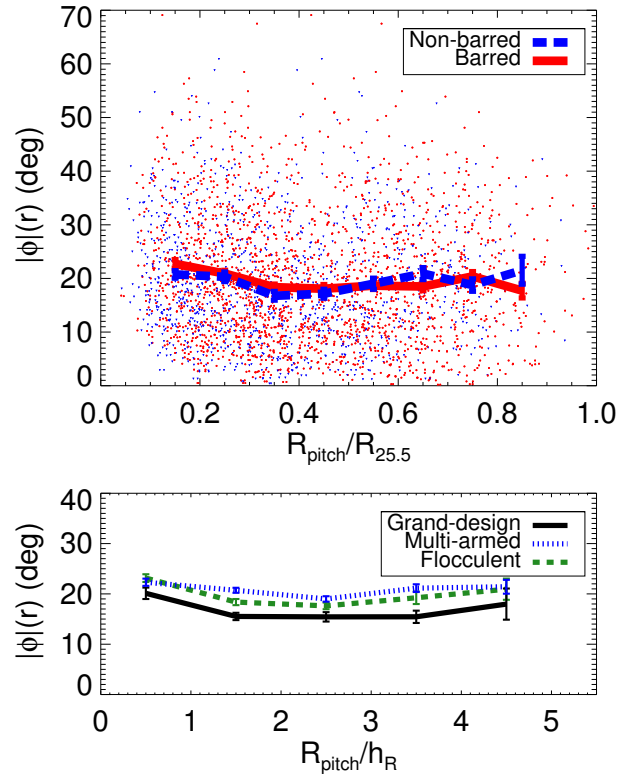


Fig. 12. *Upper panel:* Radial variation of the pitch angle based on the individual measurements of logarithmic segments by Herrera-Endoqui et al. (2015). In the x -axis we plot the boundaries of the radial interval where the pitch was measured, normalised by the $25.5 \text{ mag arcsec}^{-2}$ isophotal radius. The lines correspond to the running mean (bin size of 0.1), and the error bars are the standards deviation of the mean (the values appear listed in Table 3). Barred and non-barred galaxies are plotted separately. *Lower panel:* Same as above but using the disc scale-length for the normalization, and showing only the running mean (bin size of 1, see Table 4). The colours indicate flocculent, multi-armed, and grand-design galaxies, as indicated in the legend.

$R_{\text{pitch}}/h_{\text{R}}$	$\langle \phi \rangle$ (°) (Grand-design)	$\langle \phi \rangle$ (°) (Multi-armed)	$\langle \phi \rangle$ (°) (Flocculent)
0-1	20.12 ± 1.14	22.32 ± 0.72	23.14 ± 0.76
1-2	15.52 ± 0.73	20.72 ± 0.50	18.37 ± 0.61
2-3	15.43 ± 0.93	19.00 ± 0.54	17.61 ± 0.66
3-4	15.45 ± 1.22	21.14 ± 0.77	19.23 ± 1.24
4-5	17.97 ± 3.10	21.42 ± 1.38	20.93 ± 2.10

Table 4. As in Table. 3, but defining the radial ranges with respect to the disk scale-length (h_{R}).

2016b). This trend is maintained when different classes of spirals are studied separately.

The global bar fraction in our sample of spiral galaxies is $69 \pm 2.3\%$ ⁶. It is slightly lower for multi-armed spirals ($59 \pm 3.9\%$) and gets higher for grand-design ($71 \pm 5.2\%$) and flocculent galaxies ($77 \pm 3.3\%$). Among the 133 galaxies with $T > 5$, which are known to be faint ($M_* \lesssim 10^{10} M_{\odot}$) (see e.g. Fig. 1 in Laine et al. 2016), the fraction of barred galaxies is very high for all kinds of spirals, namely 100% for grand-design, $96.0 \pm 3.9\%$ for multi-armed, and $90.7 \pm 2.9\%$ for flocculent spirals.

5.2. Pitch angles versus T -type

For grand-design and multi-armed spirals, the global pitch angle increases with increasing T (Fig. 9), as expected, but a large scatter is found. The pitch angle is independent of T for flocculent spirals (Fig. 10), slightly flattening out the global distribution (see also Table 2). We do not find statistical and significant differences in the distribution of the pitch angle for barred and non-barred galaxies, regardless of spiral type or method used to estimate the average $|\phi|$.

In Fig. 11 we show the internal scatter of $|\phi|$ versus T for all types of spirals in our sample. We note that $\sigma_{|\phi|}$ is calculated, for each galaxy, from the pitch angle of the segments, whenever the host has more than one reliable measurement of $|\phi|$ (98.5% of the galaxies in our sample). The distribution is fairly flat. The mean $\sigma_{|\phi|}$ is $9.5^{\circ} \pm 0.3^{\circ}$, regardless of the presence of a bar, with a mild decrease in the end of the Hubble sequence.

6. Pitch angle as a function of radius

Pitch angles in individual spiral galaxies are not necessarily constant as a function of galactocentric radius (e.g. Kennicutt 1981) (see also Fig. 1), and spiral arms are often asymmetric (e.g. Elmegreen et al. 2011). In Fig. 12 we study the radial variation of the pitch angle for all the galaxies in our sample, showing all the individual measurements on logarithmic spiral segments (see also Tables 3 and 4). Pitch angles that were measured within the radial interval $[r_i, r_i']$ are represented as a function of the boundaries r_i and r_i' , normalised by the disc size (traced by $R_{25.5}$ and h_{R}).

On average, the distribution of pitch angles barely change with radius (Fig. 12), regardless of spiral class (lower panel). The statistical trend is the same for barred and non-barred galaxies (upper panel).

⁶ We calculate binomial counting errors: $\Delta f_{\text{bar}} = \sqrt{f_{\text{bar}} \cdot (1 - f_{\text{bar}}) / N_{\text{gals}}}$, where f_{bar} refers to the bar fraction and N_{gals} to the total number of galaxies.

7. Spiral properties as a function of bar strength

7.1. Pitch angle versus bar strength

In Fig. 13 we probe a possible dependence of winding of the arms on the bar-induced gravitational torque, which is expected from the manifold theory (see Sect. 9.3.1). We compare $|\phi|_{\text{weighted}}$ and $|\phi|_{\text{inner}}$ to the tangential-to-radial forcing evaluated at the bar radius: $Q_{\text{T}}(r_{\text{bar}})$ (upper and central panels). We also use measurements of $|\phi|_{\text{Fourier}}$ (lower panel), from this work and from the literature, to make sure that the results are not biased by the employed methodology. Overlaid in the upper panels of Fig. 13 is the expected correlation (roughly traced from their Fig. 5) from the numerical models by Athanassoula et al. (2009a), but we note that they evaluated tangential-to-radial forces exactly at the L_1 point (typically an unstable saddle point, Binney & Tremaine 1987). L_1 and L_2 are hard to determine accurately in our images, since the kinematic data for our sample of galaxies is scarce and their dynamical modelling is beyond the scope of this paper.

The average values of $|\phi|$ for a given $Q_{\text{T}}(r_{\text{bar}})$ -bin obtained in this work are consistent with those in the simulations by Athanassoula et al. (2009a). However, we hardly find any dependence (statistical tests⁷ confirm a very weak correlation: $\rho \approx 0.18 - 0.2$, $p < 0.01$ for $|\phi|_{\text{weighted}}$, $|\phi|_{\text{mean}}$, and $|\phi|_{\text{inner}}$). For a better comparison with the aforementioned models, we analyse separately the eight galaxies in our sample hosting R_1 or R_1R_2 outer rings. Their morphology is reproduced with manifold calculations (see Fig. 2 in Athanassoula et al. 2009a) and their L_1 point location is most likely close to r_{bar} . In spite of this, we do not find a clear trend between pitch angle and bar torque⁸. $|\phi|_{\text{Fourier}}$ is not found to correlate with bar strength either. We confirmed the lack of a strong correlation between bar strength and pitch angles when the maximum bar torque - Q_{b} - or the halo-corrected forces evaluated at the bar end - $Q_{\text{T}}^{\text{halo-corr}}(r_{\text{bar}})$ - are used instead of $Q_{\text{T}}(r_{\text{bar}})$: we obtain correlation coefficients (significances) of 0.18 (0.006) and 0.17 (0.01), respectively, when using $|\phi|_{\text{mean}}$ (and roughly the same values for $|\phi|_{\text{weighted}}$ and $|\phi|_{\text{inner}}$).

7.2. Spiral strength versus bar strength

In order to shed more light on the coupling between bars and spirals, here we assess, with unprecedented sample size, the possible dependence between their strengths, which has been extensively debated in the literature to this day (see Sect. 9.3.2). The amplitude of spirals in the S⁴G is correlated with bar strength (Fig. 14). This is clear for all proxies of the strength of spirals (A_2^{Spiral} , $Q_{\text{T}}^{\text{Spiral}}$, $Q_{\text{T,halo-corr}}^{\text{Spiral}}$), shown in the different panels (see Spearman's correlation coefficient and significance above

⁷ The Spearman's rank correlation assesses the existence of a monotonic relation between two variables. $\rho = (-1) + 1$ implies perfect (anti)correlation. Small p-values (< 0.01) indicate significant correlation.

⁸ The low number of rings of type R_1 , R_2 , or R_1R_2 is most likely due to the bias of the S⁴G towards late-type galaxies. We note that we do not sample galaxies hosting rings of type R_2 exclusively.

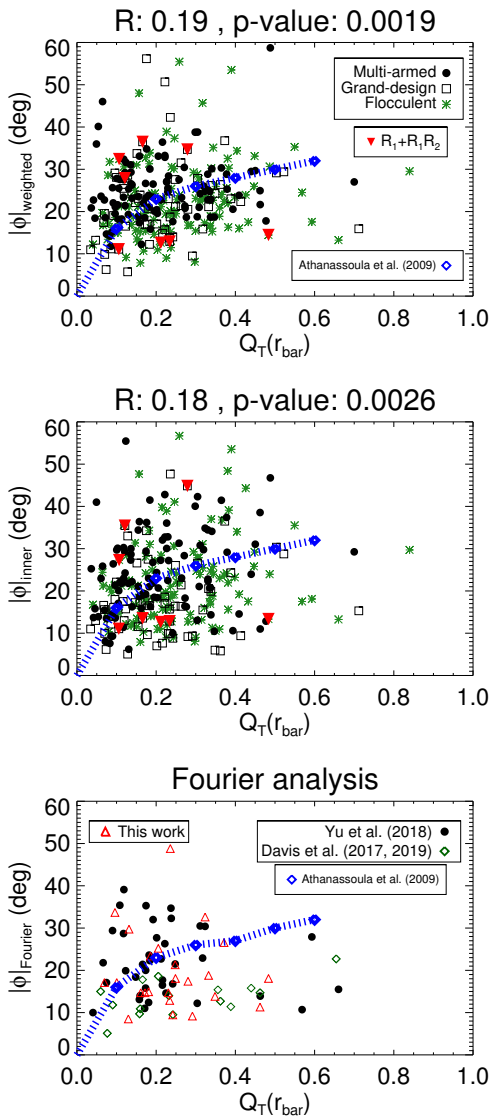


Fig. 13. Weighted mean pitch angle (*upper panel*) and mean of the innermost spiral segments (*middle panel*) versus tangential-to-radial forces evaluated at the bar radius. The blue diamonds and line outline the trend in the simulations by Athanassoula et al. (2009a) for $Q_T(L_1)$. With red triangles we show the few galaxies in our sample hosting outer rings of type R_1 or R_1R_2 . On the *lower panel* we show the same plot but using pitch angles obtained via 2-D Fourier analysis from this work and from the literature, using the measurements from Yu et al. (2018) (black points), and from Davis et al. (2017, 2019) (green diamonds).

the panels). In Fig. 15 we show that the correlation is clear when the bar strength is estimated from $Q_b^{\text{bar-only}}$ (spiral contribution to bar forcing suppressed).

The correlation between bars and spirals holds true when different types of spirals are studied separately. Interestingly, when using Q_T and A_2 , the trend for flocculent spirals is fairly similar as for grand-design and multi-armed. We note that the effect of the correction for the halo-dilution on the force profiles is slightly larger for $T \gtrsim 5$ (Díaz-García et al. 2016b). Thus, the difference between $Q_{T,\text{halo-corr}}^{\text{Spiral}}$ and Q_T^{Spiral} is more pronounced in flocculent spirals (typically hosted by late-type galaxies, see previous Sect. 5.1) than in other types of spirals.

Likewise, we find that the strength of the spirals increases with increasing bar size (Fig. 16), regardless of whether r_{bar} is

measured in physical units or relative to the disc size. In addition, the gravitational torques associated with the spirals (with and without halo-correction) increase with increasing pitch angle (Fig. 17, see also Fig. E.1): this is somehow expected, as more tightly-wrapped spirals tend to be more axisymmetric than loosely-wound arms.

8. Pitch angle and central mass concentration

The winding of the spiral arms has been claimed to depend on the prominence of the bulge (e.g. Kennicutt 1981), the steepness of the rotation curve (e.g. Seigar et al. 2005), and on the mass of the central supermassive black holes (M_{BH}) (Davis et al. 2017). The small scatter in the latter scaling relation would make the pitch angle suitable for the prediction of M_{BH} even in bulgeless galaxies. Here we assess these scaling relations in the S⁴G survey.

8.1. Pitch angle versus M_{BH}

We estimate M_{BH} from the central velocity dispersion (σ_*) from HyperLEDA (available for 117 galaxies in our sample) and the calibration from Gültekin et al. (2009):

$$\log_{10}(M_{\text{BH}}) = 8.12 + 4.24 \cdot \log_{10}(\sigma_*/200). \quad (12)$$

In order to have an estimate of the uncertainties in M_{BH} , for a subsample of S⁴G galaxies with disc inclinations lower than 65° , we checked that the inferred black hole masses are consistent with other measurements in the literature (e.g. compilations by Cisternas et al. 2013; Graham & Scott 2013; Sahu et al. 2019; Davis et al. 2019), using direct measurements and also the $M_{\text{BH}} - \sigma_*$ relation (Fig. 18), but we find scatter and outliers (e.g. NGC 5055) in the comparison that emphasise the uncertainties in our analysis.

We do not find a strong dependence between pitch angle and M_{BH} (Fig. 19): correlation coefficients (significances) of -0.24 (0.008), -0.10 (0.27), and -0.03 (0.78) for $|\phi|_{\text{mean}}$, $|\phi|_{\text{inner}}$, and $|\phi|_{\text{weighted}}$, respectively. Only a weak correlation is detected with $|\phi|_{\text{mean}}$, that becomes slightly stronger ($\rho = -0.34$ and $p = 0.0008$) when only grand-design and multi-armed galaxies are considered (for the flocculent spirals alone, no correlation is seen whatsoever). Since the correlation is weak, the scatter in M_{BH} for a given $|\phi|$ (about two decades) is much too large for this relation to yield any useful predictions concerning black hole mass. This contradicts previous reports in the literature (e.g. Davis et al. 2017): this could be explained by their use of smaller samples, but we note the lack of clear correlation can be due to the uncertainty in $|\phi|$ or to the use of indirect estimates of M_{BH} .

8.2. Pitch angle versus $d_R v_*(0)$

Díaz-García et al. (2016b) calculated the inner gradient of the stellar component of the rotation curve ($d_R v_*(0)$ hereafter). They performed a polynomial fit to the inner part of the disc+bulge component of the rotation curve ($V_{3.6\mu\text{m}}$) and took the linear term as an estimate of the inner slope, following Lelli et al. (2013).

Here, we use $d_R v_*(0)$ as a proxy of the central stellar mass concentration⁹ (e.g. Erroz-Ferrer et al. 2016; Díaz-García et al.

⁹ Díaz-García (2016) showed that $d_R v_*(0)$ tightly correlates with M_* (and thus with the maximum circular velocity), T , and the bulge-to-total mass ratio (see their Figure 4.6). This was also shown by Erroz-Ferrer et al. (2016) for a subsample of 29 S⁴G galaxies.

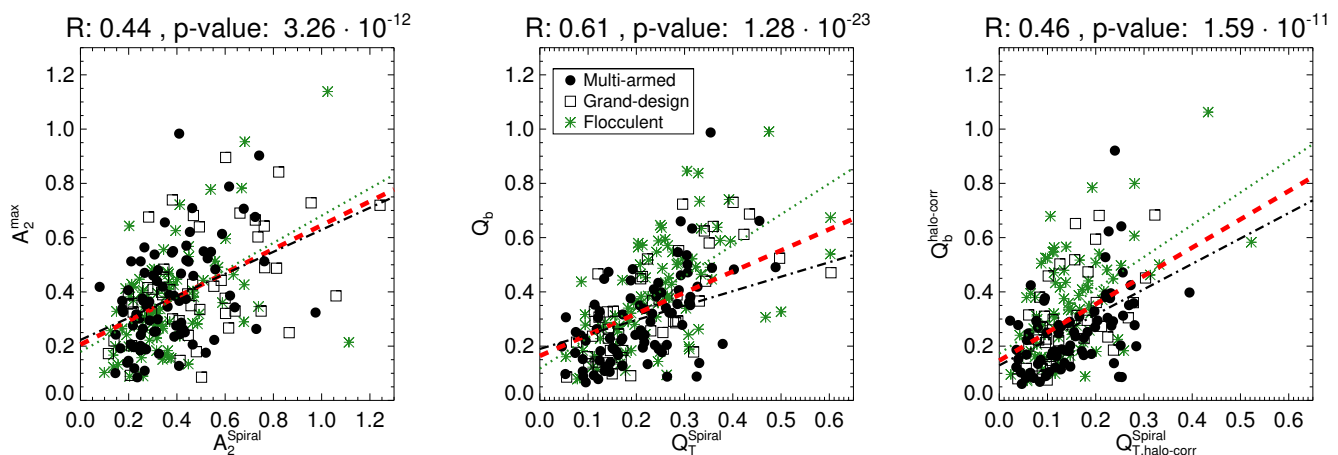


Fig. 14. Bar strength (from Díaz-García et al. 2016b) as a function of spiral strength, measured from $m = 2$ Fourier amplitudes (Eq. 11) (*left*), from tangential-to-radial forces (Eq. 9) (*middle*), also including the correction for the halo dilution (Eq. 10) (*right*). Different types of spirals are plotted with different symbols, as indicated in the legend. The red dashed line shows the linear fit to the cloud of points (in green and black we show the fit for flocculent and grand-design+multi-armed, respectively).

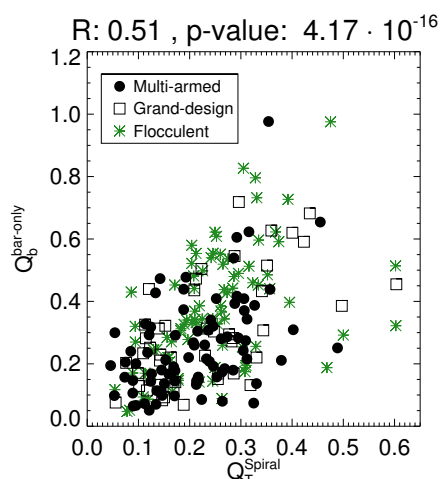


Fig. 15. Bar-only force versus spiral strength (Eq. 9). The colour palette and symbols are the same as in Fig. 14.

2016b; Salo & Laurikainen 2017). We show that the pitch angle of the galaxy is not dependent on $d_{R}v_{*}(0)$ (right panel of Fig. 19).

9. Discussion

Here we discuss the properties of spiral arms based on the study of their pitch angles and amplitudes in the S⁴G survey, as presented in previous sections. Particular attention is given to the theoretical coupling between bars and spirals, which is assessed with observations. All types of spirals are included in our analysis. We take advantage of the wealth in late-type galaxies hosting flocculent arms in the S⁴G.

In this work we use near-IR ($3.6 \mu\text{m}$) imaging, which is known to be an excellent tracer of the old stellar populations. The pitch angle of a galaxy can vary depending on the used wavelength (e.g. Martínez-García et al. 2014). According to Pour-Imani et al. (2016), the typical difference between the pitch angle measured at $3.6 \mu\text{m}$ and $7 \mu\text{m}$ is $\sim 3.75^\circ$. Recent work by Yu & Ho (2018) reported a mild decrease of the pitch from red (in-

cluding $3.6 \mu\text{m}$) to blue passbands, which is in agreement with the expectations from the density wave theory.

The classification of spiral types is not strongly dependent on wavelength: for instance, Kendall et al. (2011) showed that there is a correspondence between galaxies being grand-design in infrared and optical passbands. Elmegreen & Elmegreen (1984) had claimed that old stellar waves could not be found in patchy spirals, proposing that flocculent spirals are mainly built of star-forming regions (Seiden & Gerola 1979; Elmegreen 1981). Recent work by Elmegreen et al. (2011) studied 46 galaxies in the S⁴G and showed that most of the galaxies that are flocculent in optical wavelengths can also be classified as flocculent at $3.6 \mu\text{m}$. They also showed that, in the S⁴G, early-type spiral galaxies tend to be multi-armed and grand-design, having underlying stellar waves, whereas their late-type counterparts host flocculent spirals. We confirm this in Sect. 5 using a factor of ~ 8 bigger sample (see also Bittner et al. 2017). These trends in the Hubble sequence are probably linked to the report by Hart et al. (2016) that galaxies hosting many arms - typically multi-armed and flocculent spirals - in the Galaxy Zoo 2 (Willett et al. 2013) have bluer colours than their two-armed counterparts (i.e. the grand-design).

It is well known that the majority of galaxies present spiral arms that cannot be fitted with a single pitch angle (e.g. Savchenko & Reshetnikov 2013; Herrera-Endoqui et al. 2015). In fact, in Sect. 5.1 we showed that the internal variation of $|\phi|$ in galaxies is approximately 10° on average, and the differences in certain cases can be larger, even by a factor of two. Thus, by estimating global winding angles one misses information on individual segments, in the present paper and in most of the work in the literature.

In Sect. 6 we also showed that the distribution of $|\phi|$ does not change with increasing radius, in a statistical sense, for all types of spirals. This implies that in discs with many logarithmic spiral segments $|\phi|$ can either get larger or smaller with increasing radius, and thus the arms do not systematically wind up or loosen in the galaxy outskirts. We are in an eclectic position regarding the radial variation of $|\phi|$ discussed in the literature: Savchenko & Reshetnikov (2013) and Davis et al. (2015) showed that the spiral pitch angles increase with decreasing radius, but an opposite trend was found by Davis & Hayes (2014).

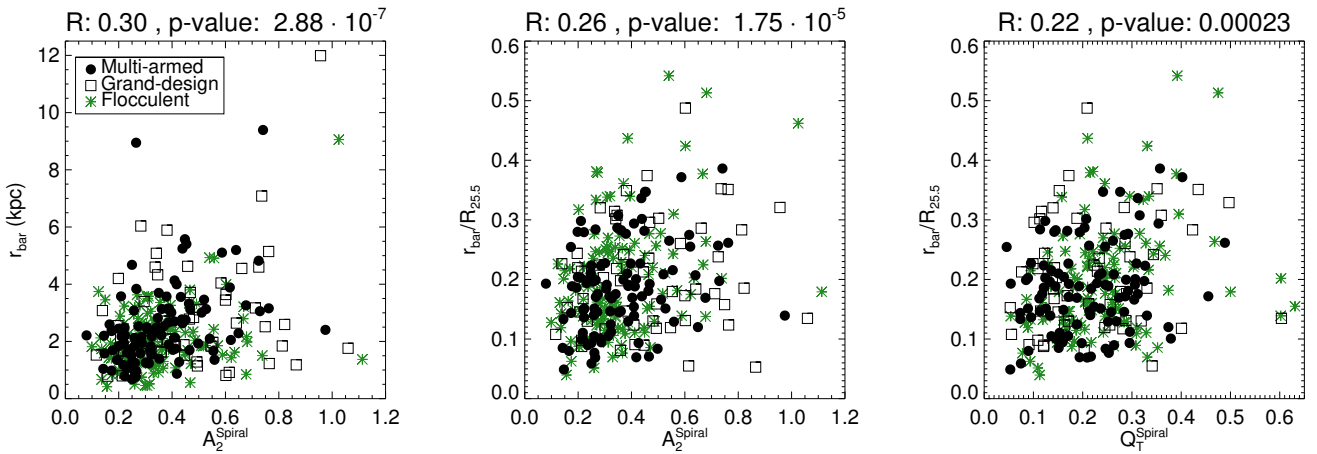


Fig. 16. Bar size, in physical units (*left*) and normalised to the disc size (*central and right panels*), as a function of the spiral strength, measured from the $m = 2$ Fourier amplitude and from the tangential-to-radial forces. The colour palette and symbols are the same as in Fig 14.

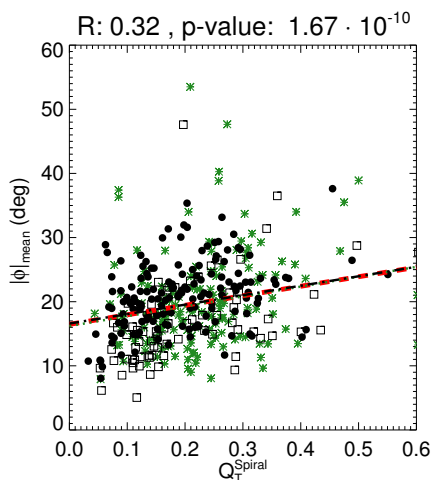


Fig. 17. Mean pitch angle as a function of spiral strength, measured from tangential-to-radial forces (Eq. 6). The colour palette and symbols are the same as in Fig 14. The red dashed line represents the linear fit to the data cloud, while the green and black lines show the fit for flocculent and grand-design+multi-armed galaxies, respectively.

In this work we propose the average pitch angle of galaxies as a global measure of the global winding angle, including a weighting for the relative arc length of the logarithmic segments (Sect. 3), so that we can study its dependence on global properties of the host galaxies. Overall, we find a good agreement between the values of the global $|\phi|$ determined with different methods (Fig. 6) and from the literature (Fig. 4 and Fig. 5). However, we also show scatter and outliers in the comparison, mainly caused by the differences in the employed methodology and its sensitivity to radial variations of $|\phi|$, and to asymmetrical or decoupled spiral arms.

9.1. Observational constraints on spiral formation: pitch angle and disc properties

The pitch angle of the spirals in the S⁴G increases with increasing T for grand-design and multi-armed galaxies, on average, unlike in the case of flocculent galaxies (Sect. 5.2). The disper-

sion for each T -type is quite large: this is somewhat unexpected, since the winding angle of the arms is a criterion for morphological classification in the de Vaucouleurs Hubble-Sandage system (de Vaucouleurs 1959), applied by Buta et al. (2015) to our sample. The lack of strong correlation might be due to uncertainties in the T -type determination or the asymmetry of the spiral arms. It might also be a consequence of the larger weight given to other criteria to classify galaxies (e.g. smoothness or bulge prominence). The weak, or missing, correlation between pitch angle and T -type has been previously reported in the literature, and is reviewed in this section.

Early-type galaxies are expected to host more tightly wound spirals on average (e.g. Considere & Athanassoula 1988; Puerari & Dottori 1992; García Gómez & Athanassoula 1993), but counterexamples are known. Using K -band imaging for 45 face-on spirals, Seigar & James (1998b) found that their measurements of arm pitch angle did not correlate with Hubble type (obtained from optical images). They argued that this was due to the fact that the morphology of the old stellar population bears little resemblance to the optical morphology used to classify galaxies. In this work we find that the relation between the global pitch angle and the T -type has a lot of scatter and is not very tight, even when $3.6 \mu\text{m}$ imaging was used for both the morphological classification and the pitch angle measurements.

Early work by Kennicutt (1981) using 113 galaxies showed that the pitch angle correlates only in an average sense with T -type, and there is a large spread in the values. Kennicutt (1981) also reported that the shape of the spirals is mainly determined by kinematic parameters (absolute rotation velocity). A correlation of pitch angle and the fraction of light in the disc component has been predicted by theoreticians (e.g. Lin & Shu 1964; Roberts et al. 1975). Also, Block et al. (2004) discussed that open spirals imply high disc-to-halo mass ratios. Nevertheless, we checked and confirmed that the pitch angle does not depend on the total dynamical mass or halo-to-stellar mass ratio, derived from inclination-corrected 21 cm line widths (see Fig. 11. and Fig. C.1. in Díaz-García et al. 2019).

Kennicutt (1981) also showed that the spiral arms might not be either purely logarithmic (associated to a density wave origin) or hyperbolic (linked to a tidal origin). The environment cannot explain the formation of all spirals in all disc galaxies in the local universe, since spiral structure in the near-IR has been found in isolated galaxies (Kendall et al. 2011). However, Seigar & James

(1998b) argued that tidal effects from near neighbours seem to have the effect of enhancing the amplitude of spirals. Analysis of Fig. 11. and Fig. C.1. in Díaz-García et al. (2019) reveals that the pitch angle in the S⁴G does not depend on the tidal interaction strength between galaxies or with the projected surface density of galaxies, taken from Laine et al. (2014) (see also Hart et al. 2016). In itself this does not rule out the influence of tidal perturbations on spiral formation: Salo & Laurikainen (2000b) showed in terms of *N*-body simulations of M51 that, excluding the outer bridge and tail, the transient spiral density waves excited by interaction were very similar to those the model would generate in isolation.

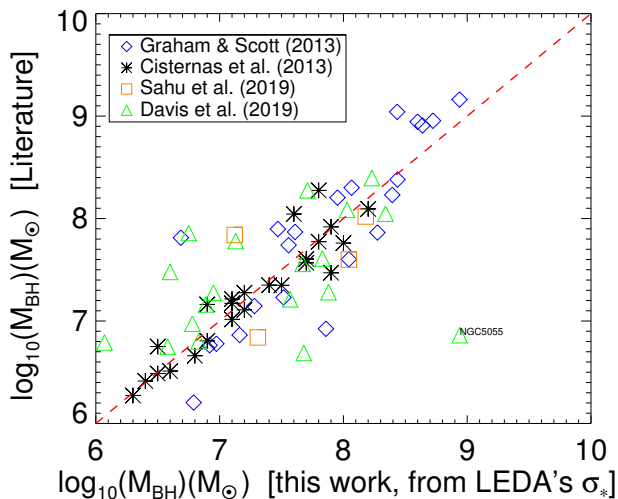


Fig. 18. For a sample of S⁴G disc galaxies with inclinations lower than 65°, we show a comparison of direct measurements of black hole masses from the compilations by Graham & Scott (2013); Sahu et al. (2019); Davis et al. (2019) - and also from Cisternas et al. (2013) (obtained via $M_{\text{BH}} - \sigma_*$ relation and using direct measurements) - with the ones estimated using LEDA's central velocity dispersions. In red, we show the straight line $y = x$.

Observations of disc galaxies at 2.1 μm by Block et al. (1994) lead the authors to conclude that large-scale structure of spirals is mainly intrinsic (i.e. not caused by tidal interactions or by the environment). They claimed that the stellar disc temperature, the gas content, and the disc mass are the main agents determining the spiral morphology. In addition, Davis et al. (2015) reported the existence of a fundamental plane of spiral structure in disc galaxies, determined by the pitch angle, the density of H I within the disc, and the mass of the stellar bulge.

A dependence between spiral arm pitch angles and the central mass concentration is expected from the density wave theory (Lin & Shu 1964, 1966). Kennicutt (1981) found that the spiral winding angle correlates only weakly with bulge-to-disc ratio. Recent work by Yu & Ho (2019) using 79 galaxies from the CALIFA survey (Sánchez et al. 2012) shows a dependence of pitch angles on the prominence of bulges, the galaxy concentration, and the total stellar mass, with a large scatter. Masters et al. (2019) performs the analysis of the spiral arms in the Galaxy Zoo project (Lintott et al. 2011; Willett et al. 2013) and reports a lack of strong correlation between bulge prominence and spiral arm tightness: galaxies with small bulges show a wide range of winding angles, while those with prominent bulges host more tightly wound arms. The authors speculate that the spiral arms are not

static density waves, but rather re-formed structures that tend to wind-up in time. A link between $|\phi|$ and the relative bulge mass would also imply a correlation of the former with the disc mass fraction: such a correlation was not found by Font et al. (2019), based on the analysis of a sample of 79 disc galaxies with estimates of the corotation radius and the pattern speed of bars and spirals.

In this paper we do not find a dependence of the pitch angle on central stellar mass concentration (Sect. 8, Fig. 19). We checked and confirmed that the pitch angle does not depend on bulge-to-total mass ratio and bulge mass, estimated from 2-D decompositions models by Salo et al. (2015). We also reassessed the dependence of the pitch on gas fraction and gas density (Appendix C), finding a weak correlation that holds for grand-design and multi-armed galaxies, but vanishes for flocculent spirals.

A correlation between spiral arm pitch angle and galactic shear rate has been found in *N*-body simulations by Grand et al. (2013) and recently confirmed by Fujii et al. (2018)¹⁰. Possible observational confirmation was provided by Seigar et al. (2006), who claimed that the dark matter halo profiles could be constrained using spiral arm morphology. Recent work by Yu et al. (2018) shows that the pitch angle correlates weakly, if at all, with the shear rate. Yu et al. (2018) actually reproduced the same plot from Seigar et al. (2006) using the same sample and the same shear rate estimates, but their own measurements of pitch angle, finding no clear correlation. We note that Seigar et al. (2006) found a connection between pitch and shear only when the latter was measured at a certain physical radius (10 kpc). The connection vanished when such radii were chosen as a function of the disc scale length. A correlation between spiral pitch angle and shear would imply an intimate link between spiral winding, central mass concentration, and dark matter haloes, which we cannot confirm in the S⁴G. In Appendix F we checked and confirmed the lack of correlation between shear and pitch angle for a subsample of 17 galaxies with available high-resolution rotation curves.

The whole picture for the formation of spiral arms remains unclear. An interpretation that disentangles the physical mechanisms that drive the formation and evolution of spiral arms when several observational parameters come into play is far from established. We conclude that, in the S⁴G, the pitch angle of spirals does not obey any definite scaling relation involving disc fundamental properties such as bulge prominence, relative dark matter content, gas fraction, stellar and dynamical mass, or environmental parameters.

9.2. Relation between the mass of the central supermassive black hole and the pitch angle of the spiral arms

Supermassive black holes are present in the centres of massive galaxies (see e.g. Lynden-Bell & Rees 1971; Kormendy & Richstone 1995; Schödel et al. 2002; Gillessen et al. 2009), with masses spanning several orders of magnitude. Recent pioneering work by the Event Horizon Telescope Collaboration et al. (2019) produced the first image of the event horizon of a supermassive black hole in the centre of M87, caught in the act of swallowing material.

¹⁰ A similar dependence between local shear rate and pitch angle has also been demonstrated in collisional *N*-body simulation of Saturn ring's self-gravity wake structures, which arise from superposition of swing amplified noise in a disc with Toomre parameter $Q < 2 - 3$ (Salo et al. 2018): such structures agree very well with the stellar dynamical predictions of Julian & Toomre (1966) and can be viewed as analogous of flocculent spiral segments.

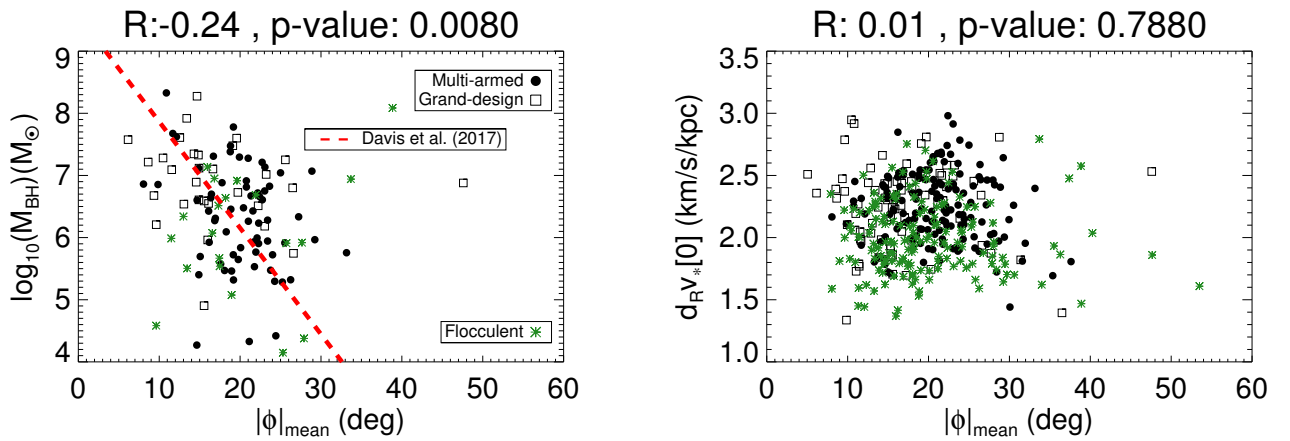


Fig. 19. Mass of supermassive black holes (*left*) (estimated from central stellar velocity dispersions) and inner slope of the stellar component of the rotation curve (*right*) (tracer of central stellar mass concentration) as a function of mean pitch angle. The red dashed straight line (left panel) corresponds to the fit from the tight correlation presented by Davis et al. (2017): their values are consistent with ours, but we do not find such a strong dependence of the pitch angle on M_{BH} . Different colours correspond to different spiral types, as indicated in the legend.

Seigar et al. (2008) found a relationship between spiral arm pitch angle and central supermassive black hole mass (M_{BH}). Further evidence was provided by Berrier et al. (2013) and, more recently, by Davis et al. (2017), who studied 44 spiral galaxies with measurements of M_{BH} , and reported a surprisingly tight correlation between M_{BH} and $|\phi|$. If real, this could potentially explain previous findings in the literature of the dependence of the pitch and the bulge mass (e.g. Yoshizawa & Wakamatsu 1975), given the known scaling relation between central black holes and bulges (e.g. Kormendy & Richstone 1995). The tight correlation between $|\phi|$ and M_{BH} would allow for the prediction of supermassive black hole mass even in bulge-less galaxies.

In Sect. 8 we used measurements in the literature of central stellar velocity dispersions to estimate the mass of the supermassive black hole hosted by the spiral galaxies in our sample. Although these are less direct estimates of M_{BH} , we have a factor of 2 bigger sample. For a subsample of galaxies, we confirmed the fairly good agreement between direct and indirect estimates of black hole masses. Our values are consistent with the aforementioned trend, but we find no clear link between black hole mass and pitch angle (only a weak correlation is found for $|\phi|_{\text{mean}}$, confirmed by statistical tests). Recent work by Graham et al. (2019) reassessed the trend between ϕ and central velocity dispersion of the same sample of galaxies (see open black stars and circles in their Fig. 5), and the resulting scaling relation seems to be weaker.

Although the mean pitch angle correlates weakly with supermassive black hole mass (inferred from σ_*) we conclude that no tight scaling relation between $|\phi|$ and M_{BH} is found in the S⁴G. This questions previous studies in the literature that were based on smaller samples (e.g. Seigar et al. 2008; Davis et al. 2017). However, we note that part of the scatter in the relation might be due to the uncertainty in the determination of both parameters.

9.3. Interplay between bars and spirals

The effect of bar-induced secular evolution on mixing and reshaping discs is subtle, but its importance is becoming consolidated. For instance, by analysing average stellar density profiles, Díaz-García et al. (2016a) showed that barred galaxies have larger disc scale-lengths and fainter extrapolated surface brightness ($\sim 15\%$ difference) than their non-barred counterparts, in

agreement with Sánchez-Janssen & Gadotti (2013). This proved the effect of bars pushing out the material that lies beyond corotation, in agreement with various simulation models (e.g. Athanassoula & Misiriotis 2002; Minchev et al. 2011; Athanassoula 2012). To further support this scenario, Seidel et al. (2015) showed that the flattening of the outer stellar velocity dispersion profiles increases with increasing bar strength. The next question is whether bars play a role in driving the formation of spirals.

Kendall et al. (2011) claimed that there is no evidence that bars trigger spirals (see also Seigar & James 1998b), since there is no connection between a galaxy being barred and having spiral structure. However, we confirm that grand-design spirals are more frequently barred than non-barred (in agreement with Elmegreen & Elmegreen 1982), and we find that this is also the case for multi-armed and flocculent galaxies (Sect. 5). Among late-type galaxies, most of the spiral galaxies are barred.

Nonetheless, non-axisymmetries cannot explain the formation of spirals in all the disc galaxies in the local universe, since spiral structure in the near-IR has been found in non-barred galaxies. In particular, nearly 30% of the spirals in our sample are non-barred, regardless of the type. In these cases, it seems unlikely that the spiral pattern could have been excited by bars that dissolved afterwards, since bars are believed to be long-lasting (e.g. Athanassoula 2003; Shen & Sellwood 2004; Villa-Vargas et al. 2010; Athanassoula et al. 2013; Sánchez-Blázquez et al. 2011; Gadotti et al. 2015) unless the disc is very gas rich (e.g. Bournaud & Combes 2002).

Masters et al. (2019) reports that, at a given bulge size, strongly barred galaxies have more loosely wound arms than non-barred galaxies: this is linked by the authors to the effect of bars slowing the winding speed of the arms. In this work we do not find any difference in the distribution of the pitch angles for barred and non-barred galaxies when $1 \leq T \leq 5$ (Sect. 5): this questions the role of bars in the formation and evolution of spirals.

9.3.1. The hypothetical link between pitch angle and bar strength: expectations from the manifold theory

The manifold theory (e.g. Romero-Gómez et al. 2006; Patsis 2006; Voglis et al. 2006; Romero-Gómez et al. 2007; Athanassoula et al. 2009b) makes specific predictions for the shape of

spirals and their coupling with bars. The models by Athanassoula et al. (2009a) show a tight correlation between the pitch angle and the tangential-to-radial forces evaluated at the unstable L_1 point (see their Fig. 5). Recent observational work by Font et al. (2019) does not confirm this causality. We find a very weak correlation between gravitational torques evaluated at the bar end - $Q_T(r_{\text{bar}})$ - and the pitch angle (Sect. 7.1).

We also checked that no clear dependence of $|\phi|$ on bar strength is found when other proxies of the latter are used – such as the maximum bar torque (Q_b), the intrinsic ellipticity, or the $m = 2$ Fourier amplitude – or when the dilution of bar gravitational torques by the halo contribution to the overall radial force field was modelled. For a more direct comparison, we additionally checked a possible dependence between bar strength and the average pitch angle of the innermost spiral segments, which are closest to the unstable Lagrangian points in barred galaxies, confirming the negative result. We also analysed this trend with other Fourier-based measurements of pitch angles, both taken from the literature or from this work, to make sure that the lack of a strong correlation cannot be attributed to the employed methodology to characterise the spiral winding in observations.

We conclude that the formation of the majority of the spiral arms in the S^4G cannot be explained with the manifold theory. Likewise, Díaz-García et al. (2019) did not confirm the manifold origin of rings in the S^4G from the predicted correlation between the ratio of outer-to-inner ring semi-major axes and the bar strength.

9.3.2. Coupling of bars and spirals analysed from their amplitudes

The observational test of the coupling between bars and spirals has been controversial for years. Based on the comparison of equivalent angles of arms and bars (measured as in Seigar & James 1998a), Seigar et al. (2003) did not find evidence for the role of bars driving spiral structure in a sample of 17 inclined galaxies. Based on the Fourier analysis of near-IR K_S -band imaging, Block et al. (2004) and Buta et al. (2009) noted that stronger bars are associated with stronger arms. Buta et al. (2005) removed the spiral contribution to the bar torque (following Buta et al. 2003) in the OSUBSGS sample (Eskridge et al. 2002) and showed a correlation between the bar and spiral torques.

On the other hand, Durbala et al. (2009) did not find a correlation between the strengths of bars and spirals in their sample of isolated galaxies. Buta et al. (2009) found the relation to be rather weak using K_S -band images from the Anglo-Australian Telescope (AAT) for 23 galaxies, and concluded that some arms might be genuine bar-driven (i.e. bars and spirals are formed from the same disc instability) but other factors might explain their formation as well.

Salo et al. (2010) reassessed the bar-spiral coupling in the above-referred OSUBSGS and AAT samples and showed a correlation between the local spiral density amplitude and the local bar-only forcing - the bar-induced tangential-to-radial forces after the effect of the spirals is suppressed - out to ≈ 1.6 bar radii. Within this radius, the authors interpret that spirals are a long-lasting continuation of the bar mode, whereas beyond the radius the spirals might be decoupled (e.g. Sellwood & Sparke 1988) or transient (e.g. Sellwood & Kahn 1991; Laurikainen & Salo 2002).

More recently, Díaz-García et al. (2016a) showed that A_2 amplitudes are larger across the discs of barred galaxies than

those of their non-barred counterparts (see their Fig. 9) when $0 \leq T < 5$. Likewise, the amplitude of non-axisymmetries beyond the bar radius were more pronounced for the strongly barred galaxies than for the weakly barred ones: this is consistent with bars exciting the spiral pattern. In addition, Elmegreen et al. (2011) found that longer bars with larger $m = 2$ density amplitudes (more evolved) appear together with stronger arms. Bittner et al. (2017) showed that galaxies with high bar contrasts tend to have higher arm contrasts as well. Lately, Sánchez-Menguiano et al. (2017) studied the oxygen abundance of spiral arms and interarm regions and found small differences for barred galaxies, not detected in their unbarred counterparts, suggesting that bars may have a subtle effect on the chemical distribution of these galaxies.

In Sect. 7.2 we showed a clear correlation between the strength of spiral arms and bars, as well as a moderate dependency between spiral strength and bar length. In addition, the mean amplitude of the arms was found to increase with increasing pitch angle (this is also confirmed in Appendix E, for all proxies of spiral strength, using all spiral segments instead of the mean). Altogether, the analysis of the amplitudes of spirals and bars supports a coupling between these stellar structures, even though the details of this connection are far from clear.

As discussed in Elmegreen et al. (2011, and references therein), grand-design spiral arms and the symmetric inner parts of multi-armed galaxies are thought to be the result of spiral density waves, that could have been driven by bars. On the other hand, properties of flocculent galaxies and the outer parts of multi-armed galaxies can in principle be explained with random local gravitational instabilities in the stellar and gaseous component (e.g. Goldreich & Lynden-Bell 1965b; Julian & Toomre 1966), swing amplified into spiral arms (e.g. Toomre 1981). Thus, it is meaningful that the correlation between the strength of bars and spirals is fairly similar for all types of spirals. Most likely, bars are not responsible for exciting flocculent spiral structure or the outer spiral modes of multi-armed galaxies. Thus, the correlation between the amplitudes of bars and spirals may not necessarily imply causation. In fact, in Appendix B we show that the correlation holds even when the mean amplitude of the two outermost spiral segments is considered (only slightly smaller correlation coefficients than for the innermost ones).

We conclude that the correlation between bar and spiral amplitudes might simply indicate that discs that are prone to the development of bars with large amplitudes are also reactive to the formation of prominent spirals, as discussed in Salo et al. (2010). Bars might play a role in creating spirals (Sanders & Huntley 1976), but mainly in strongly barred galaxies (e.g. Sellwood & Sparke 1988).

10. Summary and conclusions

In this paper we characterise the winding angle and amplitude of the spirals arms of 391 not-highly inclined galaxies ($i < 65^\circ$) from the Spitzer Survey of Stellar Structure in Galaxies (S^4G ; Sheth et al. 2010). We study barred and non-barred galaxies separately. We analyse all types of spirals, that is, grand-design, multi-armed, and flocculent.

We determine the pitch angle of the arms using the human-supervised measurements of spiral segments from Herrera-Endoqui et al. (2015) (Fig. 1). When multiple spiral segments appear for individual galaxies (98.5% of the cases), the global pitch angle ($|\phi|$) is obtained from the mean ($|\phi|_{\text{mean}}$), median ($|\phi|_{\text{median}}$), the mean of innermost logarithmic segments ($|\phi|_{\text{inner}}$), and the

mean weighted by the arc length of the segments ($|\phi|_{\text{weighted}}$) (Figs. 2, 4, 5, and 6). Values of $|\phi|$ are listed in Table A.1. In addition, for a subsample of 32 galaxies we could reliably determine the pitch angle using 2-D Fourier analysis ($|\phi|_{\text{Fourier}}$) (Fig. 3, Table 1).

Pitch angles are analysed as a function of galaxy properties – such as morphological type (T) or the estimated mass of the central supermassive black hole – and the strength of non-axisymmetries. The latter is estimated from gravitational torques (Q_T) and $m = 2$ Fourier amplitudes (A_2) from Díaz-García et al. (2016b) evaluated at the bar region (bar strength), and also at the radial ranges where the pitch angle of logarithmic segments were fitted (spiral strength) (Fig. 7).

The main results of this paper are the following:

- The distribution of grand-design, multi-armed, and flocculent spirals peaks at $T = 3$ (Sb), $T = 5$ (Sc), and $T = 6$ (Scd), respectively (Fig. 8). Roughly 2/3 of the spirals in our sample are barred (i.e. classified as SB, SAB, SAB, or SAB by Buta et al. 2015), and for $T > 5$ the bar fraction is larger than 90%.
- In galaxies with more than one measured spiral segment, $|\phi|$ has a dispersion of $\sigma = 9.5 \pm 0.3^\circ$ on average, but the differences on individual galaxies can be $\geq 15 - 20^\circ$ (Fig. 11).
- The distribution of the pitch angles as a function of galactocentric radius is flat (Fig. 12). Hence, statistically speaking, the pitch angles can either increase or decrease with radius.
- On average, the pitch angle increases with increasing Hubble stage for grand-design and multi-armed spirals (Fig. 9), as expected by the definition of T , but the scatter in this relation is large. Among flocculent spirals, $|\phi|$ is not correlated with T (Fig. 10).
- We confirm that the strengths of bars and spirals are correlated (Fig. 14). This either supports the role of bars driving the formation of spirals (Sanders & Huntley 1976) or indicates that the discs that are prone to the formation of stronger bars are also more reactive to the formation of spirals of larger amplitudes (see e.g. Salo et al. 2010). The latter interpretation is favoured by the observed coupling of the amplitudes of bar and arms even in flocculent spirals, which are implausible to be excited by bars, or when only the outermost segments of multi-armed galaxies are analysed.
- We confirm that long bars (in physical size or relative to the disc size) tend to be hosted by discs with prominent spirals (Fig. 16), in agreement with Elmegreen et al. (2011).
- The pitch angle of the spiral arms is not controlled by the bar-induced perturbation strength (Fig. 13). This questions the manifold origin of spiral arms (e.g. Athanassoula et al. 2009a).
- The distribution of pitch angles for barred and non-barred galaxies is roughly the same when $1 \leq T \leq 5$ (Figs. 9, 10, and 12). This questions the role of bars driving spiral density waves.
- The mean pitch angle is not strongly correlated with the mass of the supermassive black hole (Fig. 19), estimated from central stellar velocity dispersion (Fig. 18), and does not depend on the central concentration of stellar mass or shear (Fig. F.1). This questions previous results in the literature using smaller samples (e.g. Kennicutt 1981; Davis et al. 2015) and casts doubt on the validity of predicting M_{BH} from $|\phi|$ (e.g. Davis et al. 2017).

Acknowledgements. We thank the anonymous referee for comments that improved this paper. We acknowledge financial support from the European Union's Horizon 2020 research and innovation programme under Marie Skłodowska-Curie grant agreement No 721463 to the SUNDIAL ITN network, and from

the Spanish Ministry of Economy and Competitiveness (MINECO) under grant number AYA2016-76219-P. S.D. acknowledges the financial support from the visitor and mobility program of the Finnish Centre for Astronomy with ESO (FINCA), funded by the Academy of Finland grant nr 306531. J.H.K. acknowledges support from the Fundación BBVA under its 2017 programme of assistance to scientific research groups, for the project "Using machine-learning techniques to drag galaxies from the noise in deep imaging", and from the Leverhulme Trust through the award of a Visiting Professorship at LJMU. H.S. acknowledges financial support from the Academy of Finland (grant no: 297738). M.H.E. thanks CONACyT for supporting his postdoctoral position through the grant No. 252531. We thank Sébastien Comeron for excellent comments on the manuscript. We thank the S⁴G team for their work on the different pipelines and the data release. We thank Si Yue-Yu for providing their measurements of pitch angles for a subsample of S⁴G galaxies. We thank Joachim Janz, Aaron Watkins, and Elena D'Onghia for useful discussions. *Facilities:* Spitzer (IRAC).

References

- Athanassoula, E. 2003, MNRAS, 341, 1179
Athanassoula, E. 2012, MNRAS, 426, L46
Athanassoula, E., Machado, R. E. G., & Rodionov, S. A. 2013, MNRAS, 429, 1949
Athanassoula, E. & Misiriotis, A. 2002, MNRAS, 330, 35
Athanassoula, E., Romero-Gómez, M., Bosma, A., & Masdemont, J. J. 2009a, MNRAS, 400, 1706
Athanassoula, E., Romero-Gómez, M., & Masdemont, J. J. 2009b, MNRAS, 394, 67
Berrier, J. C., Davis, B. L., Kenefick, D., et al. 2013, ApJ, 769, 132
Binney, J. & Tremaine, S. 1987, Galactic dynamics
Bittner, A., Gadotti, D. A., Elmegreen, B. G., et al. 2017, MNRAS, 471, 1070
Block, D. L., Bertin, G., Stockton, A., et al. 1994, A&A, 288, 365
Block, D. L., Buta, R., Knapen, J. H., et al. 2004, AJ, 128, 183
Block, D. L., Puerari, I., Knapen, J. H., et al. 2001, A&A, 375, 761
Bournaud, F. & Combes, F. 2002, A&A, 392, 83
Buta, R. & Block, D. L. 2001, ApJ, 550, 243
Buta, R., Block, D. L., & Knapen, J. H. 2003, AJ, 126, 1148
Buta, R., Laurikainen, E., & Salo, H. 2004, AJ, 127, 279
Buta, R., Vasylyev, S., Salo, H., & Laurikainen, E. 2005, AJ, 130, 506
Buta, R. J., Knapen, J. H., Elmegreen, B. G., et al. 2009, AJ, 137, 4487
Buta, R. J., Sheth, K., Athanassoula, E., et al. 2015, ApJS, 217, 32
Cisternas, M., Gadotti, D. A., Knapen, J. H., et al. 2013, ApJ, 776, 50
Combes, F. & Sanders, R. H. 1981, A&A, 96, 164
Considered, S. & Athanassoula, E. 1982, A&A, 111, 28
Considered, S. & Athanassoula, E. 1988, A&AS, 76, 365
Davis, B. L., Berrier, J. C., Shields, D. W., et al. 2012, ApJS, 199, 33
Davis, B. L., Berrier, J. C., Shields, D. W., et al. 2016, 2DFFT: Measuring Galactic Spiral Arm Pitch Angle, Astrophysics Source Code Library
Davis, B. L., Graham, A. W., & Cameron, E. 2019, ApJ, 873, 85
Davis, B. L., Graham, A. W., & Seigar, M. S. 2017, MNRAS, 471, 2187
Davis, B. L., Kenefick, D., Kenefick, J., et al. 2015, ApJ, 802, L13
Davis, D. R. & Hayes, W. B. 2014, ApJ, 790, 87
de Vaucouleurs, G. 1959, Handbuch der Physik, 53, 275
Díaz-García, S. 2016, PhD thesis, University of Oulu
Díaz-García, S., Díaz-Suárez, S., Knapen, J. H., & Salo, H. 2019, A&A, 625, A146
Díaz-García, S., Salo, H., & Laurikainen, E. 2016a, A&A, 596, A84
Díaz-García, S., Salo, H., Laurikainen, E., & Herrera-Endoqui, M. 2016b, A&A, 587, A160
Díaz-García, S., Salo, H., Laurikainen, E., & Leaman, R. 2016c, ArXiv e-prints [arXiv:1611.01844]
D'Onghia, E. 2015, ApJ, 808, L8
D'Onghia, E., Vogelsberger, M., & Hernquist, L. 2013, ApJ, 766, 34
Durbala, A., Buta, R., Sulentic, J. W., & Verdes-Montenegro, L. 2009, MNRAS, 397, 1756
Elmegreen, B. G. 1990, Annals of the New York Academy of Sciences, 596, 40
Elmegreen, B. G. & Elmegreen, D. M. 1985, ApJ, 288, 438
Elmegreen, B. G. & Elmegreen, D. M. 1989, ApJ, 342, 677
Elmegreen, B. G., Elmegreen, D. M., & Montenegro, L. 1992, ApJS, 79, 37
Elmegreen, D. M. 1981, ApJS, 47, 229
Elmegreen, D. M. & Elmegreen, B. G. 1982, MNRAS, 201, 1021
Elmegreen, D. M. & Elmegreen, B. G. 1984, ApJS, 54, 127
Elmegreen, D. M. & Elmegreen, B. G. 1987, ApJ, 314, 3
Elmegreen, D. M., Elmegreen, B. G., Yau, A., et al. 2011, ApJ, 737, 32
Erroz-Ferrer, S., Knapen, J. H., Leaman, R., et al. 2016, MNRAS, 458, 1199
Erwin, P. 2018, MNRAS, 474, 5372
Eskridge, P. B., Frogel, J. A., Pogge, R. W., et al. 2002, ApJS, 143, 73
Event Horizon Telescope Collaboration, Akiyama, K., Alberdi, A., et al. 2019, ApJ, 875, L1

- Fazio, G. G., Hora, J. L., Allen, L. E., et al. 2004, *ApJS*, 154, 10
- Font, J., Beckman, J. E., James, P. A., & Patsis, P. A. 2019, *MNRAS*, 482, 5362
- Fujii, M. S., Bédorf, J., Baba, J., & Portegies Zwart, S. 2018, *MNRAS*, 477, 1451
- Gadotti, D. A., Seidel, M. K., Sánchez-Blázquez, P., et al. 2015, *A&A*, 584, A90
- García Gómez, C. & Athanassoula, E. 1993, *A&AS*, 100, 431
- Gillessen, S., Eisenhauer, F., Trippe, S., et al. 2009, *ApJ*, 692, 1075
- Giovanelli, R. & Haynes, M. P. 1988, *Extragalactic neutral hydrogen*, ed. K. I. Kellermann & G. L. Verschuur, 522–562
- Goldreich, P. & Lynden-Bell, D. 1965a, *MNRAS*, 130, 97
- Goldreich, P. & Lynden-Bell, D. 1965b, *MNRAS*, 130, 125
- Graham, A. W. & Scott, N. 2013, *ApJ*, 764, 151
- Graham, A. W., Soria, R., & Davis, B. L. 2019, *MNRAS*, 484, 814
- Grand, R. J. J., Kawata, D., & Cropper, M. 2013, *A&A*, 553, A77
- Gültekin, K., Richstone, D. O., Gebhardt, K., et al. 2009, *ApJ*, 698, 198
- Hart, R. E., Bamford, S. P., Willett, K. W., et al. 2016, *MNRAS*, 461, 3663
- Hayes, W. B., Davis, D., & Silva, P. 2017, *MNRAS*, 466, 3928
- Herrera-Endoqui, M., Díaz-García, S., Laurikainen, E., & Salo, H. 2015, *A&A*, 582, A86
- Ho, L. C., Li, Z.-Y., Barth, A. J., Seigar, M. S., & Peng, C. Y. 2011, *ApJS*, 197, 21
- Julian, W. H. & Toomre, A. 1966, *ApJ*, 146, 810
- Kalnajs, A. J. 1975, in *La Dynamique des galaxies spirales*, ed. L. Weliachew, Vol. 241, 103
- Kendall, S., Kennicutt, R. C., & Clarke, C. 2011, *MNRAS*, 414, 538
- Kennicutt, Jr., R. & Hodge, P. 1982, *ApJ*, 253, 101
- Kennicutt, Jr., R. C. 1981, *AJ*, 86, 1847
- Knapen, J. H. & Beckman, J. E. 1996, *MNRAS*, 283, 251
- Kormendy, J. & Kennicutt, Jr., R. C. 2004, *ARA&A*, 42, 603
- Kormendy, J. & Norman, C. A. 1979, *ApJ*, 233, 539
- Kormendy, J. & Richstone, D. 1995, *ARA&A*, 33, 581
- Laine, J., Laurikainen, E., & Salo, H. 2016, *A&A*, 596, A25
- Laine, J., Laurikainen, E., Salo, H., et al. 2014, *MNRAS*, 441, 1992
- Laurikainen, E. & Salo, H. 2002, *MNRAS*, 337, 1118
- Laurikainen, E., Salo, H., & Buta, R. 2004, *ApJ*, 607, 103
- Laurikainen, E., Salo, H., & Rautiainen, P. 2002, *MNRAS*, 331, 880
- Lelli, F., Fraternali, F., & Verheijen, M. 2013, *MNRAS*, 433, L30
- Lelli, F., McGaugh, S. S., & Schombert, J. M. 2016, *AJ*, 152, 157
- Lin, C. C. & Shu, F. H. 1964, *ApJ*, 140, 646
- Lin, C. C. & Shu, F. H. 1966, *Proceedings of the National Academy of Science*, 55, 229
- Lintott, C., Schawinski, K., Bamford, S., et al. 2011, *MNRAS*, 410, 166
- Lynden-Bell, D. & Rees, M. J. 1971, *MNRAS*, 152, 461
- Ma, J. 2001, *Chinese J. Astron. Astrophys.*, 1
- Martínez-García, E. E., Puerari, I., Rosales-Ortega, F. F., et al. 2014, *ApJ*, 793, L19
- Masters, K. L., Lintott, C. J., Hart, R. E., et al. 2019, *MNRAS*[arXiv:1904.11436]
- Minchev, I., Famaey, B., Combes, F., et al. 2011, *A&A*, 527, A147
- Moster, B. P., Somerville, R. S., Maulbetsch, C., et al. 2010, *ApJ*, 710, 903
- Muñoz-Mateos, J. C., Sheth, K., Regan, M., et al. 2015, *ApJS*, 219, 3
- Patsis, P. A. 2006, *MNRAS*, 369, L56
- Pour-Imani, H., Kennefick, D., Kennefick, J., et al. 2016, *ApJ*, 827, L2
- Puerari, I., Block, D. L., Elmegreen, B. G., Frogel, J. A., & Eskridge, P. B. 2000, *A&A*, 359, 932
- Puerari, I. & Dottori, H. A. 1992, *A&AS*, 93, 469
- Puerari, I., Elmegreen, B. G., & Block, D. L. 2014, *AJ*, 148, 133
- Roberts, Jr., W. W., Roberts, M. S., & Shu, F. H. 1975, *ApJ*, 196, 381
- Romero-Gómez, M., Athanassoula, E., Masdemont, J. J., & García-Gómez, C. 2007, *A&A*, 472, 63
- Romero-Gómez, M., Masdemont, J. J., Athanassoula, E., & García-Gómez, C. 2006, *A&A*, 453, 39
- Rosse, T. E. O. 1850, *Philosophical Transactions of the Royal Society of London Series I*, 140, 499
- Sahu, N., Graham, A. W., & Davis, B. L. 2019, arXiv e-prints [arXiv:1903.04738]
- Salo, H. & Laurikainen, E. 2000a, *MNRAS*, 319, 377
- Salo, H. & Laurikainen, E. 2000b, *MNRAS*, 319, 393
- Salo, H. & Laurikainen, E. 2017, *ApJ*, 835, 252
- Salo, H., Laurikainen, E., Buta, R., & Knapen, J. H. 2010, *ApJ*, 715, L56
- Salo, H., Laurikainen, E., Laine, J., et al. 2015, *ApJS*, 219, 4
- Salo, H., Ohtsuki, K., & Lewis, M. C. 2018, in *Planetary Ring Systems*, ed. M. S. Tiscareno & C. D. Murray, 434–493
- Salo, H., Rautiainen, P., Buta, R., et al. 1999, *AJ*, 117, 792
- Sánchez, S. F., Kennicutt, R. C., Gil de Paz, A., et al. 2012, *A&A*, 538, A8
- Sánchez-Blázquez, P., Ocvirk, P., Gibson, B. K., Pérez, I., & Peletier, R. F. 2011, *MNRAS*, 415, 709
- Sánchez-Janssen, R. & Gadotti, D. A. 2013, *MNRAS*, 432, L56
- Sánchez-Menguiano, L., Sánchez, S. F., Pérez, I., et al. 2017, *A&A*, 603, A113
- Sanders, R. H. & Huntley, J. M. 1976, *ApJ*, 209, 53
- Savchenko, S. S. & Reshetnikov, V. P. 2013, *MNRAS*, 436, 1074
- Schödel, R., Ott, T., Genzel, R., et al. 2002, *Nature*, 419, 694
- Schweizer, F. 1976, *ApJS*, 31, 313
- Seidel, M. K., Falcón-Barroso, J., Martínez-Valpuesta, I., et al. 2015, *MNRAS*, 451, 936
- Seiden, P. E. & Gerola, H. 1979, *ApJ*, 233, 56
- Seigar, M. S., Block, D. L., Puerari, I., Chorney, N. E., & James, P. A. 2005, *MNRAS*, 359, 1065
- Seigar, M. S., Bullock, J. S., Barth, A. J., & Ho, L. C. 2006, *ApJ*, 645, 1012
- Seigar, M. S., Chorney, N. E., & James, P. A. 2003, *MNRAS*, 342, 1
- Seigar, M. S., Davis, B. L., Berrier, J., & Kennefick, D. 2014, *ApJ*, 795, 90
- Seigar, M. S. & James, P. A. 1998a, *MNRAS*, 299, 672
- Seigar, M. S. & James, P. A. 1998b, *MNRAS*, 299, 685
- Seigar, M. S., Kennefick, D., Kennefick, J., & Lacy, C. H. S. 2008, *ApJ*, 678, L93
- Sellwood, J. A. 2011, *MNRAS*, 410, 1637
- Sellwood, J. A. & Kahn, F. D. 1991, *MNRAS*, 250, 278
- Sellwood, J. A. & Sparke, L. S. 1988, *MNRAS*, 231, 25P
- Shen, J. & Sellwood, J. A. 2004, *ApJ*, 604, 614
- Sheth, K., Regan, M., Hinz, J. L., et al. 2010, *PASP*, 122, 1397
- Shields, D. W., Boe, B., Pfountz, C., et al. 2015a, *ArXiv e-prints* [arXiv:1511.06365]
- Shields, D. W., Boe, B., Pfountz, C., et al. 2015b, *Spirality: Spiral arm pitch angle measurement*, Astrophysics Source Code Library
- Toomre, A. 1981, in *Structure and Evolution of Normal Galaxies*, ed. S. M. Fall & D. Lynden-Bell, 111–136
- Villa-Vargas, J., Shlosman, I., & Heller, C. 2010, *ApJ*, 719, 1470
- Voglis, N., Tsoutsis, P., & Efthymiopoulos, C. 2006, *MNRAS*, 373, 280
- Watkins, A. E., Mihos, J. C., & Harding, P. 2015, *ApJ*, 800, L3
- Werner, M. W., Roellig, T. L., Low, F. J., et al. 2004, *ApJS*, 154, 1
- Willett, K. W., Lintott, C. J., Bamford, S. P., et al. 2013, *MNRAS*, 435, 2835
- Yoshizawa, M. & Wakamatsu, K. 1975, *A&A*, 44, 363
- Yu, S.-Y. & Ho, L. C. 2018, *ApJ*, 869, 29
- Yu, S.-Y. & Ho, L. C. 2019, *ApJ*, 871, 194
- Yu, S.-Y., Ho, L. C., Barth, A. J., & Li, Z.-Y. 2018, *ApJ*, 862, 13
- Zwicker, C. 1963, *The Advanced Geometry of Plane Curves and Their Applications*, ed. Dover Phoenix Editions

Appendix A: Tabulated pitch angles and spiral amplitudes

The following data are listed in Table A.1 for the 391 spiral galaxies in our sample:

- *Column 1*: galaxy identification.
- *Column 2*: spiral types according to Buta et al. (2015): grand-design (G), multi-armed (M), and flocculent (F).
- *Column 3*: quality flag for the spiral fit from Herrera-Endoqui et al. (2015): good=1 and acceptable=2.
- *Column 4*: number of logarithmic segments fitted by Herrera-Endoqui et al. (2015).
- *Column 5*: mean pitch angle ($|\phi|_{\text{mean}}$) and standard deviation of the mean, computed from all the fitted logarithmic segments.
- *Column 6*: standard deviation of the pitch angle of the different spiral segments ($\sigma_{|\phi|}$).
- *Column 7*: median pitch angle ($|\phi|_{\text{median}}$)¹¹.
- *Column 8*: mean pitch angle of innermost spiral segments ($|\phi|_{\text{inner}}$) and standard deviation of the mean.
- *Column 9*: mean pitch angle weighted by the arc length of the logarithmic segments ($|\phi|_{\text{weighted}}$) and weighted standard deviation¹² (in parenthesis).
- *Column 10*: mean gravitational torque of the spiral arms ($Q_{\text{T}}^{\text{Spiral}}$), followed by the uncertainty associated with the disc thickness determination (for details, see Díaz-García et al. 2016b), and the internal dispersion (σ) computed from the maximum values of Q_{T} associated to the different spiral segments (when ≥ 0.01 , in parenthesis).
- *Column 11*: mean gravitational torque of the spiral arms corrected for the dark matter halo dilution ($Q_{\text{T,halo-corr}}^{\text{Spiral}}$), and internal dispersion of the maximum of $Q_{\text{T}}^{\text{halo-corr}}$ associated to the different spiral segments (when ≥ 0.01 , in parenthesis).
- *Column 12*: mean $m = 2$ Fourier amplitude of the spiral arms (A_2^{Spiral}), and internal dispersion of the maximum of A_2 associated to the different spiral segments (when ≥ 0.01 , in parenthesis).

Galaxy	Type	Flag	N	$ \phi _{\text{mean}}$ (°)	$\sigma_{ \phi }$ (°)	$ \phi _{\text{median}}$ (°)	$ \phi _{\text{inner}}$ (°)	$ \phi _{\text{weighted}}$ (°)	$Q_{\text{T}}^{\text{Spiral}}$	$Q_{\text{T,halo-corr}}^{\text{Spiral}}$	A_2^{Spiral}
ESO012-010	G	1	2	36.5 ± 4.3	6.1	40.8	36.5 ± 4.3	36.8 (4.3)	0.36 ± 0.03 (0.01)	0.16 (0.01)	0.35
ESO026-001	F	2	2	12.6 ± 0.7	0.9	13.3	12.6 ± 0.7	12.6 (0.6)	0.20 ± 0.02	0.09	0.20
ESO027-001	G	1	5	17.9 ± 6.6	14.7	15.2	26.1 ± 10.9	21.2 (9.2)	0.25 ± 0.02 (0.05)	–	0.76 (0.34)
ESO054-021	F	2	2	29.2 ± 0.4	0.5	29.6	29.2 ± 0.4	29.3 (0.3)	0.33 ± 0.03	0.23 (0.03)	0.33 (0.03)
ESO238-018	F	2	2	24.0 ± 17.0	24.0	40.9	24.0 ± 17.0	22.7 (16.9)	0.21 ± 0.02	–	0.22
ESO287-037	F	2	2	8.1 ± 0.1	0.2	8.2	8.1 ± 0.1	8.1 (0.1)	0.25 ± 0.02	0.11	0.37
ESO288-013	F	2	3	12.1 ± 7.8	13.5	7.8	17.5 ± 9.7	20.4 (9.6)	0.22 ± 0.03	–	0.27
ESO289-026	F	2	2	34.0 ± 5.2	7.4	39.2	34.0 ± 5.2	34.4 (5.2)	0.39 ± 0.05	0.11	0.54
ESO340-042	F	2	4	26.3 ± 8.8	17.7	31.8	39.1 ± 7.3	30.3 (9.7)	0.37 ± 0.04 (0.12)	0.28 (0.12)	0.45 (0.01)
ESO342-050	M	1	4	25.2 ± 4.5	9.0	32.2	32.9 ± 0.7	25.6 (7.6)	0.14 ± 0.02 (0.01)	0.12 (0.01)	0.27 (0.07)
ESO355-026	M	2	4	26.2 ± 11.6	23.2	18.0	14.9 ± 3.1	24.3 (19.1)	0.13 ± 0.02	0.09	0.18 (0.02)
ESO440-011	F	2	3	25.4 ± 8.5	14.7	19.0	30.6 ± 11.6	30.1 (12.6)	0.26 ± 0.03 (0.11)	0.22 (0.10)	0.39 (0.09)
ESO443-069	F	2	4	20.0 ± 7.5	15.0	26.7	23.2 ± 14.9	23.4 (12.8)	0.26 ± 0.03 (0.03)	–	0.34 (0.13)
ESO443-085	F	2	2	18.8 ± 0.9	1.3	19.8	18.8 ± 0.9	18.9 (0.9)	0.32 ± 0.02	0.17	0.27
ESO485-021	F	2	4	30.6 ± 10.3	20.6	46.5	48.4 ± 1.9	32.5 (17.7)	0.32 ± 0.02 (0.07)	0.04 (0.03)	0.51 (0.03)
ESO502-020	F	2	3	10.3 ± 4.5	7.8	14.6	8.0 ± 6.7	14.3 (2.1)	0.13 ± 0.02	0.04 (0.01)	0.36 (0.08)
ESO504-028	F	2	3	18.4 ± 4.6	8.0	13.8	20.7 ± 6.9	16.7 (5.6)	0.23 ± 0.03 (0.05)	0.14 (0.05)	0.20 (0.05)
ESO508-007	F	2	1	38.9	–	38.9	38.9	38.9	0.50 ± 0.04	0.13	1.11
ESO508-024	F	1	3	28.1 ± 6.3	11.0	31.9	34.2 ± 2.3	31.3 (7.5)	0.29 ± 0.04 (0.12)	0.18 (0.09)	0.49 (0.12)
ESO509-026	F	2	2	18.4 ± 6.0	8.5	24.4	18.4 ± 6.0	19.9 (5.8)	0.21 ± 0.03 (0.03)	–	0.63 (0.09)
ESO510-059	F	2	4	26.8 ± 10.2	20.3	44.0	44.3 ± 0.3	23.9 (17.0)	0.31 ± 0.03 (0.03)	0.19 (0.04)	0.67 (0.15)
ESO532-022	F	2	2	25.8 ± 1.5	2.1	27.3	25.8 ± 1.5	26.0 (1.5)	0.39 ± 0.03	0.20	0.67
ESO533-028	M	2	4	27.7 ± 7.4	14.9	32.3	38.5 ± 6.2	30.2 (11.9)	0.07 ± 0.02 (0.02)	0.05 (0.02)	0.11 (0.01)
ESO541-004	M	2	5	14.6 ± 2.9	6.4	17.4	8.1 ± 1.5	18.5 (3.9)	0.07 ± 0.01 (0.01)	0.04	0.14 (0.05)
ESO549-018	G	1	2	11.1 ± 1.1	1.5	12.1	11.1 ± 1.1	11.1 (1.0)	0.10 ± 0.01	0.06	0.14
ESO576-001	G	2	4	10.9 ± 5.2	10.3	13.6	9.6 ± 4.0	17.0 (6.8)	0.11 ± 0.01	0.06	0.34
ESO576-050	F	2	2	15.6 ± 3.4	4.8	19.0	15.6 ± 3.4	16.3 (3.3)	0.20 ± 0.02	0.11	0.37
ESO580-030	F	2	2	22.4 ± 0.6	0.9	23.0	22.4 ± 0.6	22.2 (0.6)	0.16 ± 0.02	0.16	0.23 (0.02)
IC0163	F	2	4	24.0 ± 10.1	20.3	32.2	24.0 ± 23.4	30.7 (11.2)	0.25 ± 0.02 (0.14)	0.18 (0.11)	0.30 (0.12)
IC0167	G	1	4	27.7 ± 11.8	23.6	41.4	47.7 ± 6.2	42.3 (15.1)	0.60 ± 0.07 (0.21)	0.30 (0.19)	1.06 (0.08)
IC0529	M	2	5	19.4 ± 5.0	11.3	14.0	30.1 ± 7.7	21.6 (9.9)	0.16 ± 0.02 (0.05)	0.12 (0.06)	0.21 (0.04)
IC0718	F	2	1	53.5	–	53.5	53.5	53.5	0.21 ± 0.02	0.13	0.22
IC0749	F	2	3	24.2 ± 7.0	12.2	28.7	31.1 ± 2.4	26.7 (8.6)	0.36 ± 0.03 (0.06)	0.22 (0.06)	0.49 (0.01)
IC0758	F	2	2	27.9 ± 4.6	6.4	32.4	27.9 ± 4.6	27.7 (4.5)	0.25 ± 0.02 (0.06)	0.21 (0.05)	0.24 (0.05)
IC0769	G	1	9	11.6 ± 3.4	10.1	8.2	9.9 ± 5.0	20.5 (6.5)	0.16 ± 0.01 (0.03)	0.08 (0.04)	0.41 (0.14)
IC0797	F	2	3	19.0 ± 4.3	7.5	20.3	23.0 ± 2.7	20.8 (4.8)	0.26 ± 0.03 (0.07)	0.21 (0.06)	0.27 (0.09)
IC1067	M	2	4	19.6 ± 1.2	2.4	18.6	18.4 ± 0.2	19.6 (2.1)	0.12 ± 0.01 (0.05)	0.06 (0.03)	0.21 (0.01)
IC1125	M	2	3	28.1 ± 13.5	23.4	29.2	40.1 ± 10.9	38.8 (14.4)	0.27 ± 0.01 (0.03)	0.22 (0.03)	0.40
IC1158	F	2	2	11.0 ± 0.8	1.2	11.8	11.0 ± 0.8	10.9 (0.8)	0.20 ± 0.03	0.14	0.31
IC1447	F	2	5	13.2 ± 5.4	12.1	9.8	10.4 ± 0.5	17.2 (11.1)	0.08 ± 0.01 (0.01)	0.06 (0.01)	0.10 (0.01)
IC1933	M	2	4	28.7 ± 8.1	16.2	28.7	36.4 ± 14.6	33.1 (14.3)	0.24 ± 0.03 (0.03)	0.13 (0.01)	0.25 (0.03)

¹¹ Errors in the median pitch angle are not provided, since bootstrap resamplings are not appropriate for this work, given the small number of spiral segments per galaxy.

¹² The weighted standard deviation is computed as $\sqrt{\frac{\sum_{i=1}^n s_i \cdot (|\phi|_i - |\phi|_{\text{weighted}})^2}{\sum_{i=1}^n s_i}}$, using the same notation as in Eqs. 2 and 3.

IC1953	M	2	3	20.6 ± 9.6	16.6	11.2	11.0 ± 0.2	21.6 (13.8)	0.31 ± 0.04	0.26	0.31 (0.06)
IC1954	G	2	4	13.8 ± 4.2	8.3	16.0	19.9 ± 3.9	18.5 (6.0)	0.12 ± 0.01 (0.08)	0.10 (0.08)	0.21 (0.09)
IC1993	M	2	3	15.2 ± 1.9	3.2	14.8	13.5 ± 1.3	14.7 (2.4)	0.12 ± 0.01	0.08	0.19 (0.02)
IC2051	F	2	2	15.5 ± 4.5	6.4	20.0	15.5 ± 4.5	15.9 (4.5)	0.16 ± 0.01 (0.01)	0.12 (0.01)	0.35
IC2627	G	2	3	21.6 ± 5.8	10.1	24.5	27.2 ± 2.8	24.9 (7.8)	0.29 ± 0.03 (0.01)	–	0.59 (0.05)
IC3115	G	2	6	17.2 ± 5.1	12.5	14.8	13.0 ± 1.8	24.6 (11.2)	0.21 ± 0.02 (0.05)	0.08 (0.03)	0.50 (0.10)
IC3391	F	2	4	29.5 ± 9.5	19.1	41.2	45.7 ± 4.4	32.0 (16.9)	0.30 ± 0.04 (0.02)	–	0.20 (0.01)
IC4237	M	2	3	17.2 ± 2.8	4.8	19.0	16.2 ± 4.5	18.6 (3.2)	0.13 ± 0.01 (0.02)	0.09 (0.02)	0.26 (0.03)
IC4536	F	2	4	14.1 ± 1.8	3.5	12.6	16.0 ± 3.4	13.5 (2.5)	0.29 ± 0.03 (0.07)	0.13 (0.05)	0.31 (0.11)
IC4901	G	2	2	9.9 ± 1.1	1.5	11.0	9.9 ± 1.1	9.9 (1.0)	0.12 ± 0.01	0.11	0.45
IC5069	M	2	5	15.0 ± 6.0	13.5	10.8	22.8 ± 12.0	20.5 (10.1)	0.31 ± 0.03	0.27	0.44
IC5273	M	2	3	28.0 ± 1.9	3.3	29.5	27.2 ± 3.0	28.4 (2.6)	0.23 ± 0.02	0.20	0.23 (0.01)
IC5321	F	2	3	22.3 ± 8.9	15.4	28.1	31.0 ± 2.9	28.3 (7.5)	0.17 ± 0.01 (0.01)	0.13 (0.01)	0.34 (0.02)
IC5325	M	2	6	15.8 ± 2.4	6.0	18.9	21.5 ± 2.3	17.5 (5.0)	0.15 ± 0.01 (0.12)	–	0.20 (0.10)
IC5332	F	2	6	13.8 ± 2.5	6.0	16.7	16.8	12.2 (5.4)	0.11 ± 0.01 (0.05)	0.07 (0.02)	0.16 (0.05)
NGC0063	G	2	3	9.6 ± 5.7	9.8	5.1	13.0 ± 7.9	13.2 (8.5)	0.05 ± 0.01	0.04	0.16
NGC0157	M	2	7	15.6 ± 5.8	15.3	11.5	29.7 ± 5.6	26.8 (10.0)	0.41 ± 0.04 (0.10)	–	0.56
NGC0255	F	2	2	19.1 ± 5.1	7.3	24.3	19.1 ± 5.1	20.2 (5.0)	0.22 ± 0.02 (0.03)	0.12 (0.02)	0.19 (0.04)
NGC0298	F	2	3	40.3 ± 5.7	9.8	41.2	39.8 ± 9.8	41.4 (8.3)	0.26 ± 0.01	0.11 (0.02)	0.68 (0.09)
NGC0300	F	2	4	20.1 ± 5.3	10.6	23.6	25.9 ± 3.8	23.3 (3.9)	0.17 ± 0.02 (0.01)	0.09 (0.02)	0.30 (0.02)
NGC0406	F	2	3	29.2 ± 13.2	22.9	31.1	41.0 ± 10.0	37.3 (12.3)	0.25 ± 0.02 (0.03)	0.12 (0.05)	0.52 (0.17)
NGC0428	F	2	2	27.9 ± 10.2	14.4	38.1	27.9 ± 10.2	28.8 (10.2)	0.47 ± 0.05	0.20	0.68
NGC0514	M	2	5	19.2 ± 4.1	9.2	25.3	15.4 ± 9.8	22.7 (5.4)	0.12 ± 0.01 (0.03)	0.08 (0.02)	0.21 (0.05)
NGC0578	G	2	3	16.7 ± 3.1	5.3	14.3	18.5 ± 4.2	15.7 (3.9)	0.28 ± 0.04 (0.08)	0.21 (0.08)	0.30 (0.09)
NGC0613	M	2	8	22.7 ± 4.9	13.9	29.8	24.0 ± 5.8	27.4 (11.3)	0.36 ± 0.03 (0.11)	0.27 (0.11)	0.74 (0.18)
NGC0628	M	2	7	18.3 ± 3.3	8.8	20.3	11.8 ± 0.5	22.7 (7.8)	0.18 ± 0.02 (0.03)	–	0.40 (0.14)
NGC0658	F	2	4	18.1 ± 6.7	13.4	18.5	23.2 ± 13.8	25.2 (12.7)	0.04	0.03 (0.01)	0.25 (0.01)
NGC0685	M	2	3	18.5 ± 2.4	4.1	19.4	20.8 ± 1.4	18.7 (3.2)	0.29 ± 0.03 (0.06)	0.22 (0.08)	0.32 (0.08)
NGC0772	M	1	5	19.9 ± 4.3	9.7	16.5	27.5 ± 9.2	23.9 (10.7)	0.10 ± 0.01 (0.01)	0.08 (0.01)	0.33 (0.10)
NGC0864	M	2	5	24.4 ± 2.8	6.3	21.6	20.7 ± 0.9	24.8 (5.5)	0.29 ± 0.02 (0.06)	0.22 (0.05)	0.38 (0.12)
NGC0895	G	2	3	31.4 ± 6.9	12.0	33.5	30.4 ± 11.9	29.1 (9.3)	0.34 ± 0.03 (0.03)	0.20 (0.03)	0.61 (0.03)
NGC0908	G	2	5	21.8 ± 5.2	11.7	28.7	30.5 ± 1.8	25.2 (8.3)	0.17 ± 0.02 (0.01)	0.13 (0.01)	0.45 (0.23)
NGC0918	M	2	4	19.0 ± 2.2	4.3	20.6	21.3 ± 1.1	19.5 (3.6)	0.21 ± 0.03	0.16 (0.03)	0.26 (0.04)
NGC0986	G	2	2	28.8 ± 5.8	8.3	34.6	28.8 ± 5.8	29.4 (5.8)	0.50 ± 0.05 (0.01)	–	1.24
NGC0991	F	2	3	17.9 ± 3.8	6.6	21.2	15.8 ± 5.5	19.0 (4.8)	0.19 ± 0.02 (0.07)	0.13 (0.06)	0.15 (0.02)
NGC1042	F	2	2	13.2 ± 0.6	0.8	13.8	13.2 ± 0.6	13.2 (0.5)	0.60 ± 0.06 (0.04)	0.52 (0.03)	0.74
NGC1073	M	2	4	14.7 ± 4.4	8.7	18.9	10.4 ± 8.4	18.7 (3.1)	0.32 ± 0.04 (0.03)	–	0.35 (0.01)
NGC1084	F	2	3	18.2 ± 1.6	2.8	18.1	16.8 ± 1.3	19.1 (1.7)	0.31 ± 0.03 (0.08)	–	0.34 (0.09)
NGC1090	G	2	5	11.7 ± 3.7	8.4	8.9	7.6 ± 1.2	14.8 (7.1)	0.14 ± 0.01 (0.06)	0.10 (0.06)	0.20 (0.03)
NGC1179	M	2	3	25.7 ± 5.1	8.8	27.5	21.9 ± 5.6	26.5 (7.4)	0.19 ± 0.02 (0.01)	0.07 (0.02)	0.32 (0.02)
NGC1187	M	2	4	31.4 ± 8.8	17.5	32.4	32.1 ± 0.4	36.4 (13.0)	0.17 ± 0.02 (0.06)	0.11 (0.05)	0.43 (0.06)
NGC1232	M	2	7	21.4 ± 4.1	10.9	23.1	11.4 ± 1.1	23.4 (8.4)	0.16 ± 0.02 (0.01)	0.11	0.29 (0.02)
NGC1255	F	2	4	10.4 ± 1.7	3.4	11.3	12.9 ± 1.6	11.5 (3.0)	0.22 ± 0.02 (0.03)	0.17 (0.03)	0.28 (0.10)
NGC1299	F	2	3	28.0 ± 2.0	3.4	28.5	26.4 ± 2.1	27.6 (3.0)	0.17 ± 0.02 (0.02)	0.15 (0.02)	0.33
NGC1300	G	2	4	14.7 ± 5.4	10.7	21.7	5.8 ± 3.3	21.5 (5.4)	0.35 ± 0.03	0.20	0.74
NGC1309	M	2	5	20.4 ± 2.5	5.5	22.2	24.4 ± 1.2	20.4 (4.5)	0.21 ± 0.03 (0.09)	0.17 (0.08)	0.32 (0.14)
NGC1338	F	2	4	19.8 ± 5.9	11.7	25.6	10.6 ± 5.2	26.0 (7.6)	0.27 ± 0.02 (0.04)	0.24 (0.04)	0.32 (0.05)
NGC1347	M	2	3	13.3 ± 4.0	6.8	11.0	14.4 ± 6.6	15.2 (5.7)	0.17 ± 0.02 (0.01)	0.13 (0.02)	0.27 (0.07)
NGC1365	G	1	3	19.1 ± 5.2	9.0	24.2	24.3 ± 0.1	23.0 (4.3)	0.28 ± 0.03 (0.16)	–	0.96 (0.53)
NGC1385	F	2	3	13.4 ± 5.5	9.6	12.9	18.1 ± 5.2	17.5 (6.3)	0.34 ± 0.03 (0.16)	–	0.56 (0.20)
NGC1493	M	2	4	20.4 ± 2.6	5.2	21.9	21.0 ± 0.9	21.1 (4.3)	0.14 ± 0.02 (0.02)	0.02	0.20
NGC1494	M	2	5	35.4 ± 8.1	18.0	30.9	28.7 ± 17.5	37.7 (13.2)	0.20 ± 0.02 (0.02)	0.13 (0.02)	0.22 (0.07)
NGC1559	F	2	4	21.0 ± 8.3	16.5	20.0	25.5 ± 19.0	23.0 (13.1)	0.60 ± 0.06 (0.07)	–	0.59 (0.12)
NGC1566	G	1	4	26.5 ± 7.6	15.1	38.7	13.5 ± 2.8	36.5 (8.0)	0.26 ± 0.05 (0.09)	0.24 (0.08)	0.75 (0.42)
NGC1637	M	2	4	16.9 ± 3.1	6.1	20.2	18.7 ± 4.9	17.3 (4.6)	0.13 ± 0.01 (0.04)	0.11 (0.04)	0.26 (0.05)
NGC1703	M	2	5	20.6 ± 3.7	8.2	22.3	12.6 ± 2.0	22.0 (7.1)	0.17 ± 0.02 (0.04)	–	0.22 (0.04)
NGC1792	M	2	6	23.1 ± 5.3	13.0	23.1	37.7 ± 3.3	25.4 (11.4)	0.31 ± 0.03 (0.11)	–	0.41 (0.05)
NGC2460	G	2	3	8.5 ± 3.7	6.4	10.9	12.1 ± 1.2	11.2 (2.1)	0.09 ± 0.03	0.08	0.41
NGC2537	F	2	3	11.5 ± 2.8	4.9	9.2	13.1 ± 4.0	12.4 (4.1)	0.63 ± 0.08	–	0.47
NGC2543	G	1	4	14.9 ± 5.2	10.3	23.2	6.0 ± 0.6	22.1 (5.5)	0.25 ± 0.03 (0.06)	0.18 (0.05)	0.66 (0.07)
NGC2608	M	2	4	26.4 ± 11.8	23.6	44.6	46.8 ± 2.2	41.0 (14.2)	0.49 ± 0.05	0.39 (0.01)	0.76 (0.07)
NGC2633	G	1	4	19.7 ± 9.3	18.6	31.7	35.5 ± 3.8	27.9 (13.0)	0.10 ± 0.01 (0.03)	–	0.47 (0.16)
NGC2701	M	2	7	30.5 ± 7.4	19.7	24.6	55.4 ± 13.6	31.6 (20.0)	0.28 ± 0.03 (0.03)	0.22 (0.03)	0.27 (0.04)
NGC2710	G	1	3	20.3 ± 8.3	14.4	24.9	18.0 ± 13.8	29.1 (4.4)	0.29 ± 0.02	0.18	0.71
NGC2712	G	1	2	9.4 ± 1.2	1.6	10.5	9.4 ± 1.2	9.5 (1.1)	0.29 ± 0.03	0.22	0.58 (0.09)
NGC2742	M	2	7	22.1 ± 4.6	12.1	25.3	8.0 ± 5.1	28.2 (6.8)	0.18 ± 0.02 (0.06)	0.15 (0.05)	0.15 (0.04)
NGC2743	F	2	1	18.1	–	18.1	18.1	18.1	0.09 ± 0.01	0.09	0.23
NGC2750	M	1	4	19.8 ± 8.4	16.9	18.7	29.7 ± 12.3	27.8 (12.2)	0.32 ± 0.04	0.25	0.73
NGC2776	M	2	6	25.5 ± 4.0	9.7	29.3	15.5 ± 1.4	25.2 (8.4)	0.13 ± 0.02 (0.04)	0.04 (0.02)	0.33 (0.10)
NGC2854	G	2	4	16.7 ± 6.3	12.5	27.1	17.2 ± 10.6	22.1 (9.2)	0.08 ± 0.01 (0.02)	0.06 (0.02)	0.44 (0.12)
NGC2903	M	2	3	23.1 ± 1.9	3.4	23.1	23.0 ± 3.3	23.3 (2.7)	0.17 ± 0.02 (0.07)	0.15 (0.07)	0.47
NGC2906	M	2	4	18.0 ± 6.1	12.1	20.3	27.2 ± 7.0	20.7 (10.1)	0.13 ± 0.02 (0.01)	0.10 (0.01)	0.20 (0.02)
NGC2964	F	2	3	33.7 ± 7.2	12.5	27.1	37.0 ± 11.1	30.2 (8.2)	0.30 ± 0.03 (0.02)	–	0.40 (0.01)
NGC2967	F	2	4	16.0 ± 4.1	8.2	21.6	8.9 ± 0.6	19.3 (6.5)	0.22 ± 0.03 (0.03)	0.18 (0.03)	0.31 (0.01)
NGC2978	G	1	3	15.9 ± 1.6	2.7	15.3	17.0 ± 1.7	15.4 (1.9)	0.16 ± 0.02 (0.01)	0.15 (0.02)	0.45
NGC3020	F	2	3	18.0 ± 5.2	9.0	13.5	12.9 ± 0.7	23.1 (7.3)	0.28 ± 0.03 (0.15)	0.12	0.39 (0.29)
NGC3021	M	2	6	22.0 ± 6.1	15.0	19.0	28.0 ± 9.0	28.1 (13.6)	0.20 ± 0.01 (0.01)	–	0.38 (0.12)
NGC3031	G	1	2	12.5 ± 0.7	0.9	13.2	12.5 ± 0.7	12.6 (0.6)	0.07 ± 0.01	0.05	0.39

NGC3041	M	2	4	20.8 ± 4.7	9.4	23.3	28.0 ± 4.7	22.4 (8.0)	0.19 ± 0.02 (0.01)	0.13 (0.01)	0.33
NGC3055	M	1	4	16.3 ± 3.7	7.5	17.0	21.8 ± 4.8	18.2 (6.7)	0.17 ± 0.01 (0.06)	0.15 (0.06)	0.31 (0.11)
NGC3057	F	2	3	11.4 ± 3.3	5.7	12.1	11.0 ± 5.7	13.0 (4.1)	0.22 ± 0.02 (0.04)	0.11 (0.02)	0.27 (0.10)
NGC3061	F	2	2	14.7 ± 6.1	8.6	20.8	14.7 ± 6.1	17.2 (5.6)	0.25 ± 0.02	0.15 (0.01)	0.46 (0.02)
NGC3147	M	2	7	10.9 ± 1.5	3.9	9.5	9.3 ± 0.2	11.8 (3.3)	0.05 ± 0.01 (0.01)	0.04 (0.01)	0.15 (0.03)
NGC3153	F	2	3	24.7 ± 7.0	12.2	27.3	31.4 ± 4.1	25.0 (8.9)	0.13 ± 0.01 (0.01)	0.08 (0.02)	0.28
NGC3155	G	1	4	12.9 ± 3.7	7.4	15.9	7.0 ± 2.0	17.0 (5.3)	0.11 ± 0.01	0.08	0.38
NGC3162	M	2	4	23.4 ± 5.2	10.5	31.8	14.4 ± 1.3	26.7 (8.6)	0.23 ± 0.02 (0.05)	0.20 (0.05)	0.39 (0.02)
NGC3177	G	2	3	10.8 ± 4.3	7.5	11.8	14.8 ± 3.0	12.8 (4.2)	0.08 ± 0.01 (0.01)	–	0.24 (0.05)
NGC3184	M	2	5	24.3 ± 3.4	7.5	23.1	19.6 ± 3.5	23.0 (6.6)	0.20 ± 0.03 (0.07)	0.12 (0.05)	0.38 (0.09)
NGC3206	M	2	3	23.1 ± 1.7	3.0	24.8	22.2 ± 2.6	23.2 (2.4)	0.28 ± 0.04 (0.01)	0.10	0.45 (0.13)
NGC3225	F	2	3	28.0 ± 7.8	13.5	25.3	20.7 ± 4.6	31.8 (11.1)	0.12 ± 0.01	0.07	0.13 (0.04)
NGC3227	G	1	4	10.5 ± 4.8	9.7	17.4	18.8 ± 1.4	16.5 (6.0)	0.11 ± 0.01 (0.01)	–	0.22 (0.15)
NGC3246	F	2	4	16.8 ± 3.7	7.3	20.5	21.5 ± 0.9	18.6 (4.8)	0.16 ± 0.02 (0.01)	0.09	0.14
NGC3294	M	2	6	22.3 ± 4.2	10.2	26.9	26.4 ± 3.9	24.9 (6.4)	0.20 ± 0.02 (0.04)	0.16 (0.05)	0.35 (0.04)
NGC3310	G	2	2	47.6 ± 7.1	10.0	54.7	47.6 ± 7.1	47.3 (7.1)	0.20 ± 0.02	–	0.57
NGC3319	G	2	3	15.6 ± 7.3	12.7	15.4	9.2 ± 6.2	18.9 (6.7)	0.43 ± 0.04 (0.02)	0.16	0.76 (0.04)
NGC3320	M	1	4	30.0 ± 7.3	14.7	38.5	41.0 ± 2.5	36.0 (10.2)	0.16 ± 0.02	0.11	0.22 (0.09)
NGC3321	F	2	2	13.4 ± 0.8	1.1	14.1	13.4 ± 0.8	13.4 (0.7)	0.25 ± 0.03	0.12	0.34 (0.03)
NGC3338	G	1	2	11.6 ± 0.4	0.6	12.0	11.6 ± 0.4	11.6 (0.4)	0.14 ± 0.01 (0.01)	0.11 (0.01)	0.63
NGC3344	M	2	6	16.9 ± 4.3	10.5	21.8	13.7 ± 8.1	22.7 (8.5)	0.10 ± 0.01 (0.02)	0.05 (0.01)	0.22 (0.04)
NGC3346	F	2	4	13.0 ± 3.6	7.2	18.8	19.0 ± 0.2	15.3 (5.5)	0.17 ± 0.03 (0.04)	0.14 (0.04)	0.21 (0.09)
NGC3359	G	1	2	26.6 ± 8.4	11.9	35.0	26.6 ± 8.4	27.8 (8.3)	0.30 ± 0.02	0.21	0.73 (0.01)
NGC3364	M	2	5	23.7 ± 5.9	13.2	24.3	22.6 ± 15.6	28.4 (10.0)	0.12 ± 0.02	0.10 (0.01)	0.18
NGC3370	M	2	7	16.5 ± 3.1	8.2	13.4	7.7 ± 0.2	20.2 (6.3)	0.17 ± 0.01 (0.05)	0.13 (0.04)	0.30 (0.11)
NGC3381	F	2	2	22.0 ± 0.1	0.1	22.0	22.0 ± 0.1	21.9 (0.0)	0.23 ± 0.02 (0.04)	–	0.36
NGC3423	M	2	6	24.0 ± 6.6	16.3	28.1	30.3 ± 2.2	27.9 (13.5)	0.22 ± 0.04 (0.02)	0.13 (0.03)	0.26 (0.04)
NGC3430	M	2	4	17.6 ± 4.7	9.4	21.9	25.2 ± 3.4	20.9 (7.1)	0.14 ± 0.01 (0.06)	0.11 (0.06)	0.26 (0.08)
NGC3433	M	2	8	16.1 ± 4.1	11.7	13.2	6.2 ± 1.4	24.3 (9.0)	0.22 ± 0.02 (0.10)	0.07 (0.04)	0.41 (0.19)
NGC3455	M	2	5	25.6 ± 5.7	12.7	24.2	23.4 ± 15.1	30.5 (8.9)	0.22 ± 0.01	0.17	0.34 (0.08)
NGC3485	M	2	4	24.3 ± 7.9	15.8	31.7	37.4 ± 5.7	28.8 (12.7)	0.25 ± 0.02 (0.03)	0.13 (0.02)	0.62 (0.04)
NGC3486	F	2	9	25.7 ± 3.8	11.5	25.2	15.2 ± 3.0	28.6 (10.4)	0.08 ± 0.01 (0.01)	0.06 (0.02)	0.37 (0.06)
NGC3488	F	2	5	11.5 ± 2.9	6.4	13.9	9.0 ± 4.9	15.4 (4.9)	0.18 ± 0.02 (0.10)	0.15 (0.10)	0.17 (0.07)
NGC3507	G	1	4	16.1 ± 2.7	5.3	19.8	17.8 ± 2.8	16.9 (4.8)	0.11 ± 0.01 (0.04)	0.10 (0.04)	0.34 (0.04)
NGC3512	M	2	5	19.0 ± 5.0	11.2	14.9	21.2 ± 12.0	20.8 (9.8)	0.07 ± 0.01 (0.02)	0.04 (0.02)	0.17 (0.08)
NGC3513	G	1	3	21.1 ± 7.4	12.9	26.3	16.4 ± 9.9	27.6 (4.5)	0.42 ± 0.03	–	0.81
NGC3521	G	1	2	14.9 ± 0.8	1.1	15.6	14.9 ± 0.8	14.9 (0.7)	0.10 ± 0.01	0.08	0.57
NGC3547	F	2	4	15.6 ± 4.5	8.9	21.6	23.0 ± 1.4	18.9 (6.5)	0.18 ± 0.01 (0.03)	0.16 (0.03)	0.29 (0.03)
NGC3583	G	1	3	14.3 ± 6.3	10.9	19.8	20.5 ± 0.8	20.3 (2.8)	0.33 ± 0.03 (0.04)	0.27 (0.04)	0.82 (0.03)
NGC3596	G	1	4	14.6 ± 5.5	11.0	20.1	23.7 ± 3.6	18.2 (9.3)	0.15 ± 0.02 (0.01)	0.12 (0.01)	0.30 (0.09)
NGC3614	M	2	6	14.5 ± 4.5	10.9	16.4	10.6 ± 6.7	21.7 (8.9)	0.21 ± 0.02 (0.07)	0.14 (0.06)	0.40 (0.02)
NGC3627	M	1	4	21.0 ± 6.7	13.4	30.5	20.7 ± 9.8	30.7 (6.6)	0.19 ± 0.02 (0.02)	–	0.68 (0.18)
NGC3629	F	2	4	14.6 ± 4.1	8.3	19.4	21.3 ± 1.9	17.5 (5.9)	0.21 ± 0.02	0.12 (0.01)	0.28 (0.04)
NGC3631	M	2	6	26.2 ± 6.5	15.9	25.8	28.4 ± 3.2	31.2 (12.7)	0.27 ± 0.03 (0.05)	–	0.42 (0.15)
NGC3659	G	2	3	23.9 ± 8.8	15.3	24.3	16.3 ± 7.9	31.5 (9.4)	0.22 ± 0.01	0.18	0.28 (0.12)
NGC3673	M	2	5	15.7 ± 6.5	14.6	7.0	22.4 ± 15.4	25.1 (12.4)	0.21 ± 0.03 (0.11)	0.12 (0.09)	0.44 (0.13)
NGC3683A	M	2	5	21.7 ± 5.6	12.6	17.1	22.9 ± 11.6	23.6 (11.7)	0.09 ± 0.01 (0.01)	0.06 (0.01)	0.22 (0.08)
NGC3684	M	2	4	25.2 ± 6.2	12.3	27.0	16.2 ± 3.8	26.3 (12.2)	0.15 ± 0.02	0.14	0.22 (0.02)
NGC3686	G	2	4	19.6 ± 6.0	11.9	21.7	27.5 ± 5.8	20.7 (5.3)	0.14 ± 0.03 (0.07)	0.12 (0.06)	0.22 (0.01)
NGC3687	M	2	6	26.4 ± 3.0	7.2	30.0	30.2 ± 0.2	27.5 (6.5)	0.09 ± 0.01 (0.01)	0.04 (0.01)	0.24 (0.07)
NGC3689	G	2	5	22.2 ± 6.3	14.2	19.9	36.1 ± 4.1	24.1 (10.4)	0.18 ± 0.02 (0.02)	0.17 (0.02)	0.36 (0.04)
NGC3701	M	2	4	20.0 ± 2.9	5.9	20.1	16.0 ± 2.3	20.2 (5.5)	0.09 ± 0.01 (0.03)	0.07 (0.04)	0.20 (0.02)
NGC3715	M	2	4	23.9 ± 6.5	13.0	28.1	29.2 ± 10.2	25.7 (8.6)	0.14 ± 0.01	0.12	0.55 (0.09)
NGC3726	M	2	4	19.0 ± 4.8	9.6	22.6	19.5 ± 3.2	22.0 (6.4)	0.25 ± 0.03	0.17	0.39 (0.09)
NGC3752	F	2	3	20.8 ± 5.1	8.9	24.1	25.8 ± 1.7	23.7 (5.9)	0.27 ± 0.01 (0.03)	0.19 (0.03)	0.53 (0.11)
NGC3756	M	2	7	18.1 ± 3.1	8.3	18.0	14.9 ± 5.3	20.6 (6.5)	0.09 ± 0.01 (0.02)	0.06 (0.02)	0.10 (0.02)
NGC3780	M	1	4	16.4 ± 4.1	8.3	18.9	11.2 ± 6.6	20.2 (3.4)	0.22 ± 0.02	0.17	0.33
NGC3810	M	1	7	18.9 ± 2.3	6.2	15.6	14.6 ± 0.4	19.0 (6.0)	0.11 ± 0.01 (0.02)	0.09	0.28 (0.08)
NGC3887	M	2	4	21.5 ± 6.3	12.7	23.0	30.8 ± 7.8	24.2 (11.3)	0.31 ± 0.03	0.24 (0.01)	0.40 (0.02)
NGC3888	M	1	5	20.7 ± 7.2	16.1	18.1	34.5 ± 12.8	25.3 (16.2)	0.10 ± 0.01 (0.07)	–	0.23 (0.11)
NGC3893	M	1	7	14.7 ± 3.3	8.7	14.6	17.8 ± 1.1	18.8 (7.3)	0.28 ± 0.02 (0.05)	–	0.67 (0.20)
NGC3930	F	2	3	18.0 ± 7.2	12.5	17.9	11.8 ± 6.2	23.3 (8.1)	0.16 ± 0.02 (0.02)	0.09	0.31 (0.04)
NGC3938	M	2	6	14.9 ± 3.3	8.0	13.7	12.4 ± 1.3	17.3 (7.4)	0.11 ± 0.01 (0.02)	–	0.29 (0.10)
NGC3949	M	2	5	33.2 ± 8.1	18.0	42.3	13.9 ± 3.7	40.1 (12.6)	0.26 ± 0.03 (0.08)	0.25 (0.07)	0.24 (0.05)
NGC3953	M	1	6	16.7 ± 3.3	8.1	18.4	21.8 ± 3.4	19.3 (5.8)	0.09 ± 0.01 (0.01)	0.06 (0.01)	0.27 (0.04)
NGC3982	M	2	4	22.3 ± 5.0	9.9	29.1	21.7 ± 7.4	24.8 (8.4)	0.11 ± 0.01 (0.05)	0.09 (0.04)	0.20
NGC3985	F	2	2	11.9 ± 9.6	13.6	21.6	11.9 ± 9.6	16.1 (8.7)	0.21 ± 0.01	0.11	0.30
NGC3992	M	1	7	12.1 ± 3.5	9.1	11.0	10.0 ± 4.7	17.6 (9.1)	0.11 ± 0.01 (0.04)	0.08 (0.03)	0.27 (0.09)
NGC4030	M	2	8	14.4 ± 3.2	9.2	14.5	14.5 ± 7.7	20.0 (6.7)	0.08 ± 0.01 (0.03)	–	0.25 (0.10)
NGC4035	F	2	2	14.5 ± 6.3	8.8	20.7	14.5 ± 6.3	16.7 (5.8)	0.30 ± 0.09 (0.29)	–	0.34 (0.13)
NGC4041	M	2	7	21.6 ± 4.3	11.3	19.9	32.8 ± 1.3	25.5 (9.2)	0.07 ± 0.01 (0.05)	0.06 (0.05)	0.25 (0.07)
NGC4051	M	2	6	22.4 ± 6.4	15.6	33.1	34.1 ± 1.0	30.1 (8.5)	0.28 ± 0.03 (0.11)	0.18 (0.09)	0.62 (0.26)
NGC4067	M	2	5	14.9 ± 5.1	11.4	21.0	24.2	21.4 (6.0)	0.05	0.04 (0.01)	0.17 (0.04)
NGC4080	F	2	2	10.3 ± 2.4	3.4	12.7	10.3 ± 2.4	10.7 (2.4)	0.16 ± 0.01	0.04	0.32 (0.05)
NGC4108B	F	2	2	34.0 ± 18.9	26.7	52.9	34.0 ± 18.9	25.3 (16.8)	0.21 ± 0.02	0.01	0.16
NGC4123	M	2	3	21.1 ± 3.7	6.4	21.3	21.0 ± 6.3	21.0 (5.4)	0.24 ± 0.02 (0.09)	0.20 (0.08)	0.45 (0.15)
NGC4133	M	2	8	16.2 ± 3.7	10.6	10.9	21.0 ± 12.9	18.8 (10.6)	0.09 ± 0.01 (0.05)	0.06 (0.04)	0.30 (0.05)
NGC4136	F	2	4	19.0 ± 4.5	9.1	16.7	24.4 ± 7.7	19.7 (8.1)	0.18 ± 0.02	0.12 (0.03)	0.29 (0.01)

NGC4145	F	2	3	21.2 ± 2.7	4.7	23.8	23.9 ± 0.1	22.5 (3.2)	0.19 ± 0.02 (0.06)	0.15 (0.08)	0.30
NGC4152	M	2	5	29.2 ± 5.7	12.8	29.9	36.2 ± 6.3	34.8 (9.2)	0.25 ± 0.02 (0.03)	–	0.56 (0.11)
NGC4162	M	2	5	27.2 ± 4.5	10.1	26.7	29.5 ± 9.5	26.5 (8.1)	0.12 ± 0.01 (0.03)	0.11 (0.03)	0.16 (0.03)
NGC4165	G	2	6	14.2 ± 3.8	9.2	11.7	17.5 ± 8.5	20.1 (8.1)	0.19 ± 0.01 (0.03)	0.10 (0.02)	0.50 (0.04)
NGC4189	M	2	5	16.0 ± 4.5	10.0	18.6	22.5 ± 3.9	21.8 (6.4)	0.22 ± 0.02 (0.08)	0.14 (0.06)	0.31 (0.11)
NGC4193	G	2	2	11.0 ± 0.1	0.1	11.1	11.0 ± 0.1	11.0 (0.1)	0.11 ± 0.02	0.09	0.21
NGC4204	F	2	2	35.5 ± 1.9	2.7	37.4	35.5 ± 1.9	35.3 (1.9)	0.47 ± 0.04 (0.07)	0.11 (0.02)	0.68 (0.03)
NGC4210	M	2	4	10.7 ± 4.0	7.9	9.5	15.9 ± 6.4	12.2 (7.3)	0.05 ± 0.01 (0.02)	0.04 (0.02)	0.08 (0.01)
NGC4212	M	2	5	16.2 ± 4.1	9.2	11.2	21.5 ± 10.3	18.4 (9.3)	0.20 ± 0.01 (0.07)	0.18 (0.07)	0.33 (0.06)
NGC4237	G	2	4	16.0 ± 2.7	5.4	14.4	17.6 ± 6.2	15.9 (4.1)	0.08 ± 0.01	–	0.11 (0.04)
NGC4254	M	1	5	20.8 ± 6.8	15.1	21.9	17.1 ± 10.0	29.3 (10.6)	0.23 ± 0.02 (0.05)	–	0.49 (0.15)
NGC4273	M	2	3	20.1 ± 4.2	7.3	17.7	23.0 ± 5.3	20.1 (5.4)	0.11 ± 0.01	–	0.36
NGC4276	F	2	2	24.2 ± 4.4	6.3	28.6	24.2 ± 4.4	25.6 (4.2)	0.33 ± 0.02 (0.01)	0.31 (0.01)	0.37 (0.03)
NGC4294	M	2	4	29.4 ± 9.5	19.1	26.6	41.5 ± 14.9	30.3 (13.3)	0.26 ± 0.02 (0.08)	0.19 (0.08)	0.35 (0.04)
NGC4303	M	2	5	23.0 ± 6.5	14.4	16.5	38.6 ± 1.1	24.9 (12.6)	0.30 ± 0.03 (0.16)	–	0.51 (0.04)
NGC4314	G	2	4	23.2 ± 12.5	25.0	44.4	44.8 ± 0.4	34.7 (18.2)	0.21 ± 0.03 (0.07)	0.09 (0.04)	0.60 (0.18)
NGC4319	G	2	4	18.0 ± 6.0	11.9	19.7	22.1 ± 12.0	20.1 (10.8)	0.14 ± 0.02	–	0.64
NGC4321	M	2	4	21.4 ± 5.0	10.1	26.5	29.8 ± 3.3	26.0 (8.1)	0.23 ± 0.02 (0.10)	0.20 (0.11)	0.64 (0.09)
NGC4390	G	2	6	17.9 ± 5.7	14.0	16.7	26.6 ± 18.3	23.9 (14.0)	0.23 ± 0.02 (0.02)	0.18 (0.01)	0.21 (0.05)
NGC4411A	G	2	3	11.4 ± 5.1	8.8	11.0	15.7 ± 4.7	13.8 (5.5)	0.29 ± 0.02 (0.01)	0.13 (0.01)	0.60 (0.01)
NGC4411B	M	2	6	14.1 ± 2.9	7.2	17.7	12.2 ± 7.8	17.1 (4.7)	0.15 ± 0.01 (0.02)	0.12 (0.03)	0.23 (0.12)
NGC4412	G	2	3	17.3 ± 8.0	13.9	11.8	9.4 ± 2.4	22.4 (12.2)	0.34 ± 0.04 (0.12)	0.28 (0.10)	0.37 (0.04)
NGC4413	G	2	2	11.3 ± 0.4	0.6	11.7	11.3 ± 0.4	11.3 (0.4)	0.14 ± 0.01 (0.01)	0.11 (0.01)	0.36 (0.03)
NGC4414	M	2	5	28.9 ± 6.0	13.4	30.5	32.3 ± 1.9	31.4 (7.8)	0.06 ± 0.01 (0.01)	–	0.09 (0.04)
NGC4428	M	2	6	21.6 ± 3.9	9.5	20.8	15.0 ± 0.9	22.1 (7.4)	0.12 ± 0.01 (0.02)	0.10 (0.01)	0.29 (0.10)
NGC4430	F	1	3	9.6 ± 4.3	7.5	7.5	12.7 ± 5.2	15.4 (4.7)	0.20 ± 0.02	0.14	0.27
NGC4480	M	2	5	18.4 ± 4.8	10.8	16.8	17.2 ± 0.4	20.8 (11.3)	0.14 ± 0.01 (0.01)	0.11 (0.02)	0.21 (0.06)
NGC4487	M	2	5	32.0 ± 4.2	9.5	27.1	41.5 ± 5.1	30.1 (7.7)	0.20 ± 0.03 (0.01)	0.16 (0.02)	0.25
NGC4501	M	2	8	19.2 ± 3.9	10.9	18.5	15.8 ± 2.7	22.3 (9.2)	0.07 ± 0.01	0.06 (0.01)	0.24 (0.11)
NGC4504	G	2	4	15.4 ± 3.7	7.5	19.3	15.8 ± 8.1	16.5 (6.2)	0.15 ± 0.02 (0.01)	0.08 (0.02)	0.21 (0.03)
NGC4519	M	2	4	21.8 ± 6.5	13.0	22.3	29.1 ± 8.9	25.3 (10.3)	0.29 ± 0.03 (0.07)	0.23 (0.08)	0.37 (0.18)
NGC4535	M	2	6	17.8 ± 4.8	11.7	17.7	14.6 ± 3.2	23.8 (9.1)	0.24 ± 0.03 (0.10)	0.12 (0.08)	0.53 (0.14)
NGC4536	M	2	4	25.0 ± 5.6	11.2	25.5	32.8 ± 7.2	27.5 (9.0)	0.21 ± 0.02 (0.05)	–	0.72 (0.10)
NGC4545	M	2	4	22.8 ± 5.0	10.1	19.3	27.2 ± 10.5	22.7 (9.0)	0.22 ± 0.02	0.17	0.26
NGC4548	G	2	5	8.6 ± 2.2	5.0	9.1	8.8 ± 5.9	11.3 (3.3)	0.14 ± 0.02 (0.07)	0.11 (0.06)	0.28 (0.17)
NGC4559	M	2	4	21.8 ± 5.2	10.5	19.1	18.3 ± 0.8	20.8 (8.6)	0.19 ± 0.02 (0.01)	0.13 (0.04)	0.42 (0.09)
NGC4561	F	2	2	22.1 ± 5.1	7.3	27.3	22.1 ± 5.1	22.8 (5.1)	0.21 ± 0.02 (0.12)	0.06 (0.05)	0.26 (0.06)
NGC4567	F	2	3	16.6 ± 4.8	8.4	14.0	20.0 ± 5.9	17.1 (6.3)	0.25 ± 0.03 (0.05)	0.22 (0.04)	0.32 (0.02)
NGC4568	M	2	4	22.8 ± 5.1	10.1	24.9	22.5 ± 12.2	26.0 (7.1)	0.18 ± 0.02 (0.03)	–	0.41 (0.17)
NGC4571	F	2	3	12.7 ± 2.9	5.0	12.3	10.1 ± 2.2	13.5 (3.2)	0.16 ± 0.02 (0.02)	0.09 (0.03)	0.21 (0.01)
NGC4647	F	2	4	17.5 ± 2.2	4.4	21.0	21.2 ± 0.2	16.9 (3.9)	0.15 ± 0.03 (0.05)	–	0.31 (0.04)
NGC4651	M	2	4	9.8 ± 1.8	3.6	12.0	10.4 ± 1.6	11.2 (2.4)	0.06	0.05	0.22 (0.05)
NGC4653	G	2	7	15.3 ± 4.1	10.8	12.7	17.3 ± 11.2	21.2 (7.1)	0.32 ± 0.03 (0.13)	0.14 (0.02)	0.48 (0.20)
NGC4654	M	2	4	23.8 ± 7.3	14.6	33.8	28.6 ± 6.9	29.3 (7.6)	0.37 ± 0.05	0.29	0.65
NGC4658	F	2	2	24.8 ± 5.1	7.3	29.9	24.8 ± 5.1	25.4 (5.1)	0.24 ± 0.02 (0.05)	0.22 (0.05)	0.48
NGC4680	G	2	1	21.4	–	21.4	21.4	21.4	0.28 ± 0.02	–	0.55
NGC4682	M	2	7	13.6 ± 3.4	9.0	13.5	9.6 ± 3.9	18.1 (6.4)	0.07 ± 0.01 (0.02)	0.06 (0.02)	0.12 (0.03)
NGC4701	F	2	3	17.7 ± 7.0	12.1	12.1	21.8 ± 9.7	21.2 (10.1)	0.09 ± 0.01	–	0.16
NGC4713	F	2	4	25.3 ± 7.5	15.0	33.4	12.8 ± 1.6	30.6 (12.4)	0.31 ± 0.03 (0.03)	0.26 (0.01)	0.35 (0.12)
NGC4731	F	2	2	29.7 ± 1.1	1.6	30.8	29.7 ± 1.1	29.5 (1.1)	0.83 ± 0.10 (0.01)	0.43 (0.01)	1.02
NGC4775	F	2	4	21.0 ± 4.0	8.1	23.2	21.5 ± 1.7	21.5 (6.3)	0.25 ± 0.03 (0.04)	–	0.27 (0.08)
NGC4779	M	2	5	14.5 ± 2.5	5.5	16.8	12.9 ± 4.8	16.1 (4.4)	0.40 ± 0.04 (0.11)	0.28 (0.10)	0.59 (0.13)
NGC4781	M	2	6	16.9 ± 4.2	10.2	22.3	16.4 ± 7.3	21.3 (7.8)	0.25 ± 0.02 (0.02)	0.22 (0.04)	0.39 (0.14)
NGC4800	F	2	6	19.6 ± 3.2	7.8	21.9	23.5 ± 6.4	21.3 (5.3)	0.07 ± 0.01	0.06	0.27 (0.01)
NGC4806	F	2	5	15.4 ± 3.7	8.3	17.4	18.0 ± 0.7	18.1 (6.6)	0.16 ± 0.03 (0.02)	0.14 (0.03)	0.27 (0.10)
NGC4814	F	2	4	15.6 ± 4.6	9.2	23.3	23.6 ± 0.3	19.1 (7.1)	0.09	0.03 (0.01)	0.58 (0.05)
NGC4897	F	2	2	7.9 ± 0.5	0.7	8.4	7.9 ± 0.5	7.9 (0.5)	0.05	0.04 (0.02)	0.22
NGC4899	F	2	4	14.1 ± 4.3	8.7	20.5	21.2 ± 0.7	16.7 (5.9)	0.14 ± 0.02 (0.04)	0.13 (0.04)	0.24
NGC4902	M	1	6	19.7 ± 4.5	11.1	19.9	23.0 ± 3.8	23.8 (9.4)	0.12 ± 0.01 (0.05)	0.08 (0.04)	0.25 (0.09)
NGC4904	F	2	5	23.8 ± 7.7	17.2	17.1	29.2 ± 12.1	28.7 (14.2)	0.33 ± 0.02 (0.17)	0.28 (0.16)	0.41 (0.22)
NGC4928	F	2	3	21.7 ± 9.5	16.5	14.2	25.4 ± 15.2	30.5 (13.3)	0.26 ± 0.02 (0.06)	–	0.57 (0.18)
NGC4965	F	2	2	19.0 ± 3.7	5.2	22.7	19.0 ± 3.7	19.4 (3.6)	0.31 ± 0.04	0.25	0.36
NGC4981	M	2	6	20.6 ± 6.0	14.8	15.9	9.3 ± 6.6	25.6 (13.0)	0.11 ± 0.01 (0.01)	0.10 (0.01)	0.33 (0.20)
NGC4995	M	2	6	11.7 ± 4.3	10.5	13.0	13.0 ± 6.7	18.2 (7.6)	0.27 ± 0.02 (0.05)	0.26 (0.05)	0.39 (0.04)
NGC5012	M	2	7	18.8 ± 3.4	9.0	17.8	26.1 ± 11.0	23.5 (10.3)	0.12 ± 0.01 (0.02)	0.09 (0.03)	0.34 (0.06)
NGC5016	F	2	3	10.7 ± 2.3	4.0	9.1	12.1 ± 3.0	9.2 (2.0)	0.09 ± 0.01 (0.02)	0.08 (0.02)	0.17 (0.05)
NGC5033	M	2	7	18.8 ± 3.7	9.8	22.3	25.1 ± 0.1	23.6 (6.0)	0.12 ± 0.01 (0.03)	0.08 (0.04)	0.54 (0.21)
NGC5042	F	2	3	13.6 ± 6.1	10.6	11.8	18.4 ± 6.6	17.2 (7.3)	0.21 ± 0.02 (0.07)	0.14 (0.07)	0.24 (0.14)
NGC5054	M	1	7	19.7 ± 5.3	14.0	17.7	31.9 ± 2.1	28.3 (8.5)	0.11 ± 0.01 (0.05)	0.07 (0.04)	0.27 (0.11)
NGC5055	M	2	7	8.1 ± 2.6	7.0	5.5	16.9 ± 3.5	11.6 (6.5)	0.05 ± 0.01 (0.02)	0.04 (0.02)	0.15 (0.05)
NGC5085	G	2	6	15.3 ± 3.6	8.8	17.6	22.0 ± 4.4	18.3 (5.8)	0.13 ± 0.01 (0.01)	0.09 (0.03)	0.34 (0.13)
NGC5105	F	2	5	19.8 ± 4.8	10.7	20.3	11.5 ± 7.8	24.8 (7.1)	0.26 ± 0.02 (0.02)	0.12 (0.02)	0.46 (0.07)
NGC5112	M	2	5	37.6 ± 5.3	11.8	36.5	42.3 ± 5.8	38.8 (9.4)	0.46 ± 0.05	0.25	0.44
NGC5194	G	1	6	14.9 ± 2.5	6.2	15.8	15.6 ± 0.2	17.0 (4.1)	1.18 ± 0.19 (1.62)	–	0.87 (0.68)
NGC5205	G	2	2	15.5 ± 1.1	1.6	16.6	15.5 ± 1.1	15.9 (1.0)	0.23 ± 0.01 (0.01)	0.16 (0.01)	0.47 (0.01)
NGC5236	M	2	4	18.1 ± 4.9	9.8	21.3	10.6 ± 3.3	20.6 (6.9)	0.31 ± 0.03 (0.11)	0.23 (0.10)	0.42
NGC5240	F	2	5	15.5 ± 4.5	10.0	14.5	12.4 ± 2.1	18.7 (8.2)	0.09 ± 0.01 (0.04)	0.07 (0.03)	0.15 (0.07)
NGC5247	M	1	5	24.2 ± 6.7	15.1	25.1	39.1 ± 0.4	30.7 (10.9)	0.55 ± 0.06 (0.05)	–	0.75 (0.06)

NGC5248	M	2	7	23.6 ± 6.1	16.2	15.7	25.8 ± 19.8	34.1 (12.1)	0.33 ± 0.04 (0.15)	0.24 (0.11)	0.97 (0.33)
NGC5254	M	2	6	15.3 ± 5.5	13.5	14.6	13.6 ± 1.0	21.7 (12.6)	0.24 ± 0.02 (0.03)	0.17 (0.03)	0.26 (0.06)
NGC5300	M	2	4	17.8 ± 1.8	3.6	17.7	15.8 ± 1.9	18.4 (3.2)	0.15 ± 0.02 (0.03)	0.10 (0.02)	0.14 (0.03)
NGC5313	M	2	4	20.2 ± 9.6	19.2	34.6	20.9 ± 13.7	32.5 (10.0)	0.17 ± 0.01	0.15	0.36 (0.05)
NGC5320	F	2	4	20.7 ± 5.0	10.1	24.8	21.8 ± 2.9	22.7 (7.0)	0.17 ± 0.01 (0.05)	0.11 (0.04)	0.26 (0.04)
NGC5334	F	2	3	13.3 ± 3.4	6.0	16.2	16.7 ± 0.5	15.5 (3.2)	0.09 ± 0.02 (0.02)	0.06 (0.03)	0.22 (0.14)
NGC5339	F	2	3	13.5 ± 4.2	7.3	15.5	17.5 ± 2.0	15.0 (5.0)	0.39 ± 0.05 (0.21)	0.33 (0.18)	0.56 (0.08)
NGC5350	F	2	4	25.5 ± 7.8	15.7	27.4	36.8 ± 9.4	24.1 (11.5)	0.22 ± 0.02 (0.06)	0.18 (0.06)	0.31 (0.06)
NGC5364	G	1	4	15.5 ± 4.1	8.2	14.1	20.9 ± 6.8	11.4 (4.1)	0.12 ± 0.02 (0.01)	0.10 (0.02)	0.41 (0.29)
NGC5371	G	1	5	13.4 ± 7.0	15.8	5.9	11.6 ± 5.7	23.1 (13.2)	0.17 ± 0.02 (0.04)	0.10 (0.04)	0.60 (0.21)
NGC5375	M	2	5	18.5 ± 6.0	13.4	15.0	26.8 ± 11.8	23.4 (10.3)	0.17 ± 0.02 (0.02)	0.11 (0.02)	0.45
NGC5376	M	2	3	10.7 ± 1.1	1.9	10.2	9.7 ± 0.5	10.5 (1.5)	0.03	0.03 (0.01)	0.09 (0.01)
NGC5426	M	2	4	19.7 ± 3.9	7.8	25.4	26.4 ± 1.0	22.0 (6.3)	0.25 ± 0.05 (0.10)	0.19 (0.09)	0.50 (0.09)
NGC5427	G	1	7	23.0 ± 6.0	16.0	21.1	42.5 ± 8.5	21.2 (11.8)	0.15 ± 0.02 (0.06)	0.08 (0.01)	0.46 (0.12)
NGC5430	G	1	2	12.9 ± 2.0	2.8	14.8	12.9 ± 2.0	12.9 (1.9)	0.15 ± 0.01 (0.04)	–	0.38 (0.04)
NGC5452	F	1	3	20.1 ± 7.4	12.8	15.5	25.0 ± 9.5	18.8 (9.0)	0.16 ± 0.01	0.10	0.20 (0.02)
NGC5457	M	2	6	19.2 ± 3.7	9.0	24.2	18.5 ± 8.3	20.1 (7.1)	0.22 ± 0.01 (0.03)	0.15 (0.02)	0.47 (0.26)
NGC5468	M	2	7	28.2 ± 5.9	15.5	32.5	42.8 ± 3.5	33.3 (8.5)	0.30 ± 0.03 (0.05)	–	0.32 (0.04)
NGC5480	F	2	2	38.8 ± 0.1	0.1	38.9	38.8 ± 0.1	38.9 (0.0)	0.26 ± 0.02	0.20	0.66 (0.07)
NGC5584	M	2	6	23.6 ± 3.7	9.0	21.3	34.4 ± 2.5	23.5 (7.5)	0.38 ± 0.05 (0.10)	0.28 (0.08)	0.28 (0.11)
NGC5595	M	2	5	22.4 ± 4.2	9.3	26.7	20.0 ± 11.2	25.5 (6.1)	0.30 ± 0.03 (0.07)	0.28 (0.07)	0.43 (0.05)
NGC5600	F	2	2	16.1 ± 10.7	15.1	26.7	16.1 ± 10.7	19.3 (10.1)	0.16 ± 0.01 (0.02)	–	0.33 (0.05)
NGC5660	F	2	4	27.6 ± 7.4	14.7	38.2	15.2 ± 3.9	35.7 (9.2)	0.31 ± 0.04 (0.21)	–	0.33 (0.16)
NGC5668	F	2	3	17.4 ± 5.6	9.7	18.3	22.5 ± 4.2	21.2 (6.5)	0.17 ± 0.02 (0.04)	–	0.45 (0.01)
NGC5669	F	2	3	18.1 ± 7.3	12.6	21.0	25.0 ± 4.0	24.2 (6.1)	0.35 ± 0.05 (0.13)	0.22 (0.11)	0.47 (0.02)
NGC5676	G	2	5	16.6 ± 3.5	7.9	18.0	16.1 ± 2.7	19.1 (6.4)	0.20 ± 0.02 (0.05)	0.18 (0.05)	0.36 (0.05)
NGC5693	F	2	2	21.9 ± 3.7	5.2	25.6	21.9 ± 3.7	23.8 (3.2)	0.22 ± 0.02	0.19	0.26
NGC5768	F	2	2	19.8 ± 4.9	6.9	24.6	19.8 ± 4.9	19.4 (4.8)	0.12 ± 0.01 (0.02)	0.06 (0.02)	0.34
NGC5774	F	2	4	17.8 ± 2.8	5.6	20.0	15.1 ± 4.9	19.1 (4.2)	0.16 ± 0.02 (0.03)	0.13 (0.05)	0.28 (0.07)
NGC5783	F	2	4	23.1 ± 5.1	10.1	30.8	31.9 ± 1.1	22.7 (8.6)	0.33 ± 0.02 (0.01)	0.21 (0.02)	0.32 (0.01)
NGC5832	F	2	1	9.0	–	9.0	9.0	9.0	0.21 ± 0.01	0.08	0.39
NGC5861	G	2	5	15.7 ± 3.6	8.1	16.0	17.0 ± 1.0	18.5 (5.2)	0.29 ± 0.03 (0.02)	0.21 (0.02)	0.51 (0.27)
NGC5885	M	2	5	20.4 ± 4.3	9.6	21.6	29.4 ± 3.0	23.2 (7.2)	0.15 ± 0.01	0.14 (0.01)	0.22 (0.05)
NGC5892	F	2	5	17.0 ± 3.2	7.2	15.6	24.2 ± 1.0	15.4 (5.3)	0.20 ± 0.02 (0.02)	0.16 (0.03)	0.27 (0.02)
NGC5915	F	2	3	20.6 ± 10.4	18.0	20.1	29.5 ± 9.3	25.1 (11.8)	0.35 ± 0.02 (0.13)	–	0.85 (0.10)
NGC5921	F	1	4	17.3 ± 4.3	8.6	20.4	23.8 ± 3.4	22.4 (6.4)	0.26 ± 0.03 (0.13)	–	0.47 (0.28)
NGC5937	F	2	3	22.9 ± 4.1	7.1	27.0	27.0 ± 0.1	25.4 (4.2)	0.12 ± 0.01 (0.07)	–	0.30 (0.04)
NGC5950	G	2	2	15.3 ± 2.2	3.1	17.5	15.3 ± 2.2	15.9 (2.1)	0.40 ± 0.05 (0.06)	0.32 (0.05)	0.49 (0.03)
NGC5956	M	2	4	23.9 ± 6.0	11.9	26.5	30.0 ± 7.9	26.6 (8.7)	0.07 ± 0.01 (0.02)	0.04 (0.02)	0.17 (0.03)
NGC5957	M	2	5	21.9 ± 6.6	14.7	21.1	36.0 ± 3.8	27.0 (10.6)	0.15 ± 0.02 (0.06)	–	0.36 (0.12)
NGC5962	F	2	4	16.8 ± 4.2	8.3	23.2	24.0 ± 0.8	19.5 (6.6)	0.16 ± 0.01 (0.08)	0.15 (0.08)	0.28 (0.14)
NGC5963	F	2	4	14.5 ± 7.4	14.8	27.1	27.3 ± 0.2	24.1 (8.2)	0.11 ± 0.01	0.09	0.26
NGC5964	M	2	4	28.4 ± 4.4	8.8	31.8	31.0 ± 0.8	29.7 (7.1)	0.29 ± 0.02 (0.11)	0.23 (0.11)	0.46 (0.03)
NGC5970	M	2	5	14.9 ± 2.1	4.7	15.8	16.3 ± 0.5	15.8 (3.4)	0.12 ± 0.01 (0.04)	0.10 (0.04)	0.27 (0.02)
NGC5985	M	2	6	11.7 ± 2.1	5.0	10.5	7.6 ± 0.1	14.2 (4.9)	0.09 ± 0.01 (0.04)	0.06 (0.02)	0.17 (0.07)
NGC6063	G	2	4	13.9 ± 2.4	4.9	16.8	18.0 ± 1.2	13.2 (4.1)	0.14 ± 0.01 (0.03)	0.10 (0.03)	0.18 (0.03)
NGC6070	M	2	5	22.2 ± 2.7	6.1	20.7	28.5 ± 0.3	23.3 (5.3)	0.18 ± 0.02 (0.06)	0.14 (0.06)	0.28 (0.08)
NGC6106	F	2	3	14.7 ± 2.7	4.7	16.0	14.0 ± 4.6	16.1 (3.5)	0.21 ± 0.02 (0.03)	0.16 (0.06)	0.29 (0.02)
NGC6181	G	2	4	25.6 ± 5.6	11.2	26.4	33.0 ± 6.6	28.6 (9.7)	0.24 ± 0.02 (0.09)	–	0.55 (0.09)
NGC6207	F	2	3	21.9 ± 5.4	9.4	24.7	27.2 ± 2.4	24.3 (7.1)	0.24 ± 0.02	0.21 (0.01)	0.39 (0.06)
NGC6339	M	2	3	23.4 ± 6.4	11.1	24.6	29.2 ± 4.7	27.0 (8.2)	0.35 ± 0.03 (0.11)	0.24 (0.09)	0.41 (0.09)
NGC6412	F	2	2	13.5 ± 1.2	1.6	14.6	13.5 ± 1.2	13.5 (1.1)	0.33 ± 0.03	0.19	0.41
NGC6923	M	2	5	21.6 ± 5.7	12.7	25.7	22.0 ± 3.7	27.6 (4.9)	0.13 ± 0.01	0.10 (0.01)	0.41 (0.18)
NGC7070	F	2	4	20.7 ± 8.7	17.3	33.0	35.6 ± 2.6	30.6 (11.9)	0.19 ± 0.02 (0.04)	0.08 (0.04)	0.32 (0.04)
NGC7163	G	2	2	5.1 ± 2.5	3.5	7.5	5.1 ± 2.5	5.7 (2.4)	0.12 ± 0.02 (0.01)	0.09 (0.01)	0.34 (0.02)
NGC7167	G	2	2	16.6 ± 5.0	7.1	21.6	16.6 ± 5.0	17.4 (4.9)	0.17 ± 0.02	0.13	0.23 (0.02)
NGC7171	G	2	4	13.0 ± 2.9	5.7	11.5	16.5 ± 5.0	12.2 (4.3)	0.15 ± 0.01 (0.04)	0.11 (0.03)	0.30 (0.05)
NGC7205	F	2	2	13.1 ± 1.0	1.4	14.1	13.1 ± 1.0	13.2 (1.0)	0.17 ± 0.02	0.14	0.26
NGC7247	M	1	7	15.1 ± 3.6	9.5	10.1	7.6 ± 2.5	21.3 (9.2)	0.09 ± 0.01 (0.03)	–	0.18 (0.06)
NGC7254	G	2	2	17.0 ± 4.7	6.6	21.7	17.0 ± 4.7	18.8 (4.3)	–	–	–
NGC7371	G	2	2	6.2 ± 0.8	1.2	7.0	6.2 ± 0.8	6.3 (0.8)	0.06 ± 0.01 (0.01)	0.04	0.12
NGC7412	M	1	7	22.1 ± 3.9	10.3	21.3	34.8 ± 4.9	24.8 (8.7)	0.26 ± 0.02 (0.07)	0.18 (0.06)	0.54 (0.05)
NGC7418	F	2	4	19.5 ± 5.5	10.9	25.1	24.5 ± 3.8	23.5 (4.9)	0.18 ± 0.02 (0.08)	0.15 (0.08)	0.26 (0.08)
NGC7424	F	2	2	15.8 ± 1.2	1.8	17.0	15.8 ± 1.2	15.6 (1.2)	0.24 ± 0.03	0.10	0.45
NGC7437	F	2	2	15.1 ± 1.6	2.3	16.8	15.1 ± 1.6	14.9 (1.6)	0.26 ± 0.03	0.18	0.20
NGC7448	M	2	4	21.0 ± 4.7	9.4	21.1	15.9 ± 5.2	22.5 (6.6)	0.26 ± 0.04 (0.03)	–	0.26 (0.05)
NGC7531	M	2	3	18.0 ± 1.8	3.1	16.9	19.2 ± 2.3	18.5 (2.6)	0.15 ± 0.02 (0.02)	0.12 (0.02)	0.38 (0.08)
NGC7661	F	2	4	29.3 ± 15.8	31.6	54.9	56.7 ± 1.8	49.0 (19.0)	0.24 ± 0.02 (0.02)	0.13 (0.02)	0.31
NGC7689	M	2	3	26.6 ± 7.4	12.9	21.0	19.2 ± 1.8	26.7 (10.5)	0.25 ± 0.03	0.19	0.26
NGC7723	F	2	3	22.5 ± 8.0	13.8	19.3	28.4 ± 9.1	21.2 (10.0)	0.14 ± 0.01 (0.05)	0.11 (0.05)	0.20 (0.04)
NGC7724	G	2	3	11.4 ± 2.6	4.5	13.5	9.9 ± 3.7	11.8 (3.3)	0.12 ± 0.02 (0.06)	0.09 (0.05)	0.20 (0.07)
NGC7741	F	2	3	9.6 ± 4.4	7.6	9.3	13.4 ± 4.1	13.3 (4.5)	0.33 ± 0.03 (0.11)	0.20 (0.10)	0.39 (0.15)
NGC7743	G	2	6	22.2 ± 4.0	9.7	20.4	34.2 ± 2.2	23.1 (9.0)	0.17 ± 0.03	–	0.46 (0.01)
NGC7757	M	2	5	23.8 ± 4.6	10.4	24.1	31.3 ± 7.2	27.5 (8.4)	0.26 ± 0.02 (0.04)	0.25 (0.05)	0.52 (0.07)
NGC7764	F	2	3	23.6 ± 7.7	13.3	20.4	29.3 ± 8.9	25.2 (10.4)	0.41 ± 0.04 (0.27)	0.38 (0.25)	0.39 (0.17)
NGC7793	F	2	2	11.4 ± 1.2	1.6	12.5	11.4 ± 1.2	11.5 (1.1)	0.15 ± 0.02 (0.01)	0.12 (0.02)	0.24
NGC7798	M	2	5	16.9 ± 5.2	11.6	16.0	13.6 ± 3.0	19.4 (10.6)	0.14 ± 0.01 (0.02)	–	0.41 (0.12)
PGC011367	F	2	2	18.5 ± 0.2	0.2	18.6	18.5 ± 0.2	18.4 (0.1)	0.19 ± 0.03	0.09	0.26

PGC012664	F	2	3	14.3 ± 3.4	5.9	11.8	11.0 ± 0.8	18.9 (4.2)	0.25 ± 0.03 (0.07)	0.14 (0.05)	0.19 (0.05)
PGC027616	F	2	5	17.5 ± 3.1	6.9	15.3	19.2 ± 3.9	18.4 (5.8)	0.26 ± 0.02 (0.05)	0.08 (0.02)	0.33 (0.03)
PGC028380	F	2	2	16.9 ± 1.5	2.1	18.4	16.9 ± 1.5	16.7 (1.5)	0.27 ± 0.03 (0.01)	0.13 (0.01)	0.37 (0.01)
PGC032091	M	2	3	21.4 ± 9.2	16.0	24.7	30.1 ± 5.4	27.1 (8.7)	0.19 ± 0.01	0.09	0.22
PGC043345	F	2	2	18.8 ± 2.2	3.1	21.0	18.8 ± 2.2	18.8 (2.2)	0.21 ± 0.02	0.11	0.32 (0.02)
PGC043458	F	2	2	28.4 ± 1.1	1.6	29.5	28.4 ± 1.1	28.4 (1.1)	0.31 ± 0.03	0.17	0.38
PGC045958	G	2	2	9.9 ± 0.0	0.1	9.9	9.9	9.8 (0.0)	0.15 ± 0.02	–	0.17
PGC047721	G	2	3	9.6 ± 5.3	9.2	7.0	13.4 ± 6.5	11.3 (7.1)	0.11 ± 0.01 (0.03)	0.01	0.46 (0.16)
PGC048087	F	2	2	21.2 ± 2.2	3.2	23.5	21.2 ± 2.2	21.2 (2.2)	0.18 ± 0.02	0.09	0.20
PGC048179	F	2	3	14.6 ± 5.0	8.7	15.8	19.2 ± 3.4	16.0 (5.1)	0.30 ± 0.03 (0.07)	0.25 (0.06)	0.32 (0.11)
PGC069448	M	2	4	27.2 ± 4.5	9.0	33.5	34.5 ± 1.0	28.8 (7.3)	0.31 ± 0.04 (0.05)	0.23 (0.05)	0.34 (0.11)
UGC02081	F	2	2	12.3 ± 0.9	1.3	13.2	12.3 ± 0.9	12.3 (0.9)	0.13 ± 0.02	0.07	0.17
UGC02443	F	2	5	16.4 ± 5.2	11.6	21.0	23.3 ± 2.3	22.9 (7.5)	0.16 ± 0.03	0.11	0.16
UGC04151	M	2	4	24.4 ± 2.5	5.0	23.6	26.9 ± 4.8	24.7 (4.3)	0.13 ± 0.03	0.08	0.16
UGC04169	M	2	5	31.6 ± 9.7	21.6	20.1	27.3 ± 8.8	31.1 (16.8)	0.20 ± 0.02 (0.01)	0.10 (0.01)	0.35 (0.05)
UGC04549	F	2	3	13.5 ± 4.0	7.0	16.1	17.5 ± 1.3	15.4 (4.2)	0.13 ± 0.01 (0.04)	0.08 (0.03)	0.18 (0.03)
UGC04841	F	2	2	16.2 ± 0.8	1.1	17.0	16.2 ± 0.8	16.2 (0.8)	0.22 ± 0.02	0.17 (0.01)	0.32
UGC04867	F	2	4	15.7 ± 7.2	14.4	27.1	28.2 ± 1.1	25.5 (7.9)	0.37 ± 0.02	0.10 (0.02)	0.57 (0.04)
UGC05358	F	2	2	11.3 ± 6.8	9.6	18.1	11.3 ± 6.8	15.3 (5.5)	0.33 ± 0.04	0.11	0.60
UGC05707	F	2	3	13.0 ± 5.1	8.8	13.1	17.4 ± 4.3	16.4 (5.1)	0.27 ± 0.03	0.10 (0.03)	0.62
UGC06023	F	2	2	14.3 ± 2.2	3.1	16.5	14.3 ± 2.2	14.6 (2.2)	0.15 ± 0.01	0.12	0.27
UGC06194	F	2	3	18.2 ± 5.8	10.1	18.3	18.2 ± 10.1	23.0 (7.2)	0.18 ± 0.02 (0.03)	0.14 (0.04)	0.17 (0.04)
UGC06335	F	2	4	13.9 ± 4.1	8.2	18.2	19.7 ± 1.5	16.3 (3.7)	0.15 ± 0.01 (0.01)	0.15 (0.01)	0.23
UGC06903	F	2	3	16.9 ± 5.9	10.2	14.0	21.1 ± 7.1	15.3 (6.5)	0.19 ± 0.02 (0.07)	0.09 (0.05)	0.26 (0.13)
UGC06930	F	2	2	47.7 ± 9.6	13.6	57.3	47.7 ± 9.6	48.0 (9.6)	0.27 ± 0.03	0.17	0.34
UGC07133	M	2	3	30.1 ± 4.6	8.0	33.5	28.3 ± 7.4	30.5 (6.3)	0.19 ± 0.02 (0.02)	0.09 (0.04)	0.18
UGC07848	F	2	3	16.0 ± 4.8	8.3	11.2	18.4 ± 7.2	12.9 (4.7)	0.13 ± 0.01 (0.02)	0.07 (0.01)	0.12 (0.01)
UGC08041	M	2	4	20.5 ± 5.1	10.3	20.4	14.4 ± 6.0	22.9 (7.8)	0.33 ± 0.06 (0.05)	0.14 (0.03)	0.29 (0.03)
UGC08516	F	2	2	17.6 ± 3.8	5.3	21.4	17.6 ± 3.8	18.1 (3.7)	0.25 ± 0.02	–	0.20
UGC08658	F	2	4	14.6 ± 3.9	7.9	19.8	21.2 ± 1.4	15.1 (6.7)	0.12 ± 0.01 (0.03)	0.06 (0.02)	0.25 (0.03)
UGC08909	F	2	2	21.2 ± 1.4	2.0	22.6	21.2 ± 1.4	21.2 (1.4)	0.09 ± 0.01	0.02	0.14
UGC09569	F	2	2	17.5 ± 0.3	0.4	17.8	17.5 ± 0.3	17.5 (0.3)	0.27 ± 0.02 (0.03)	0.17 (0.02)	0.63
UGC09730	F	2	2	24.7 ± 2.8	4.0	27.5	24.7 ± 2.8	24.4 (2.8)	0.25 ± 0.02 (0.08)	0.08 (0.04)	0.34
UGC09837	M	2	3	18.1 ± 1.0	1.8	17.5	17.0 ± 0.4	18.2 (1.5)	0.16 ± 0.03	0.09	0.20
UGC10020	F	2	3	36.3 ± 10.5	18.2	37.2	27.5 ± 9.8	41.7 (10.0)	0.08 ± 0.01 (0.02)	0.07 (0.02)	0.17 (0.12)
UGC10445	F	2	2	18.0 ± 3.7	5.2	21.7	18.0 ± 3.7	19.6 (3.3)	0.24 ± 0.03	0.11	0.30 (0.13)
UGC10721	M	2	5	27.1 ± 6.1	13.5	31.2	34.6 ± 3.4	31.1 (6.2)	0.25 ± 0.01	0.19	0.59 (0.08)
UGC10803	F	2	1	37.4	–	37.4	37.4	37.4	0.09 ± 0.02	0.07	0.15

Table A.1. Average pitch angles and spiral amplitudes.

Appendix B: Bar strength versus spiral strength: extended analysis

In Sect. 7.2 we showed a correlation between the bar strength and the mean strength of the spirals. Here we test this dependence when only the mean of the amplitude the two innermost and the two outermost spiral segments are considered (see Fig. B.1). We only use galaxies with more than four measured spiral segments. The strength of the spiral segments is measured from the $m = 2$ Fourier density amplitudes (left), tangential-to-radial forces (centre), and also torques corrected for the halo-dilution (right).

In Fig. B.2 we confirm the same trends when using bar-only forces (see Sect. 4.1). Interestingly, the correlation between the amplitude of the bar and that of the spiral modes holds in these extreme radial ranges.

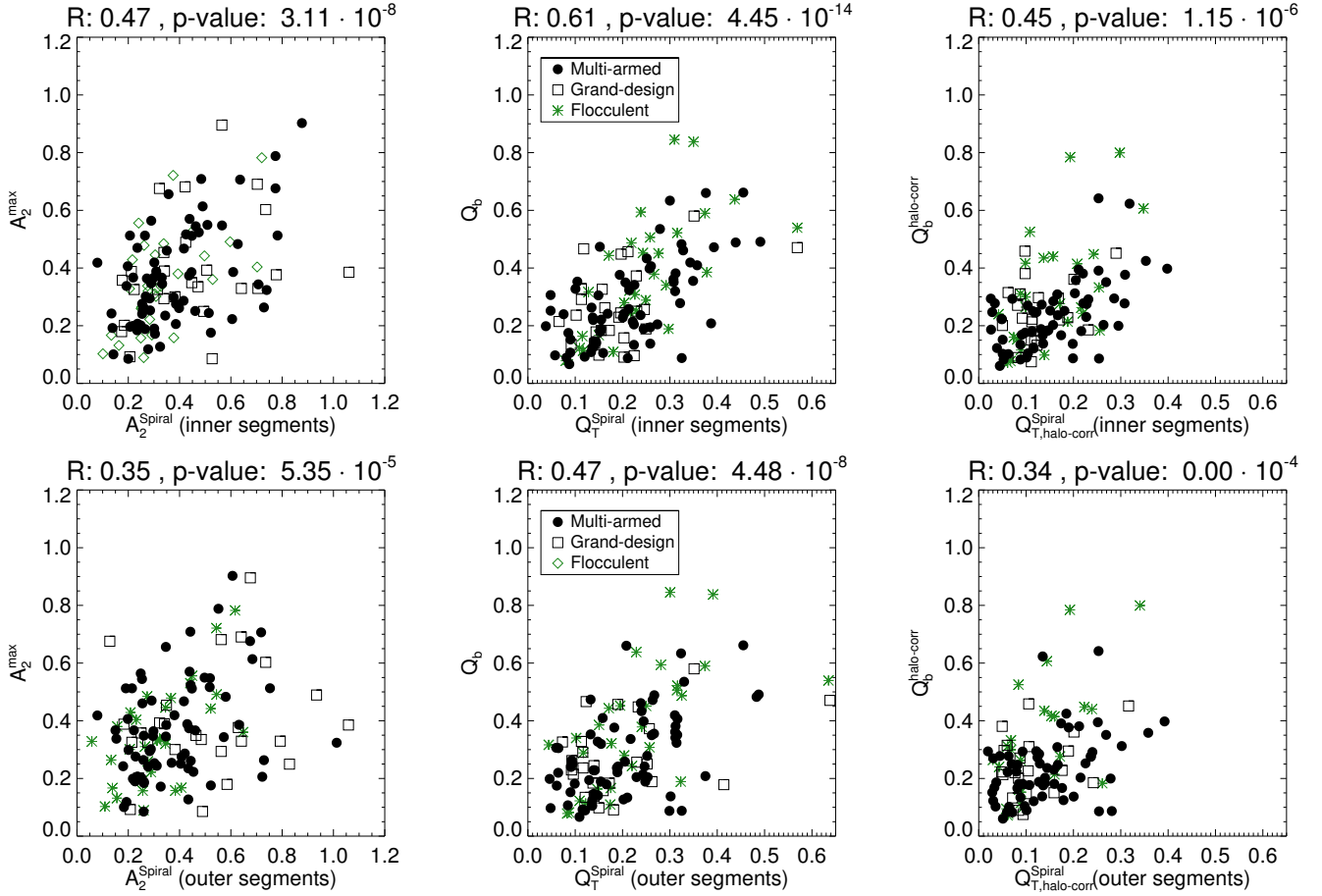


Fig. B.1. As in Fig. 14, but taking the mean of the maximum amplitude of the two innermost (*upper panels*) and outermost (*lower panels*) spiral logarithmic segments.

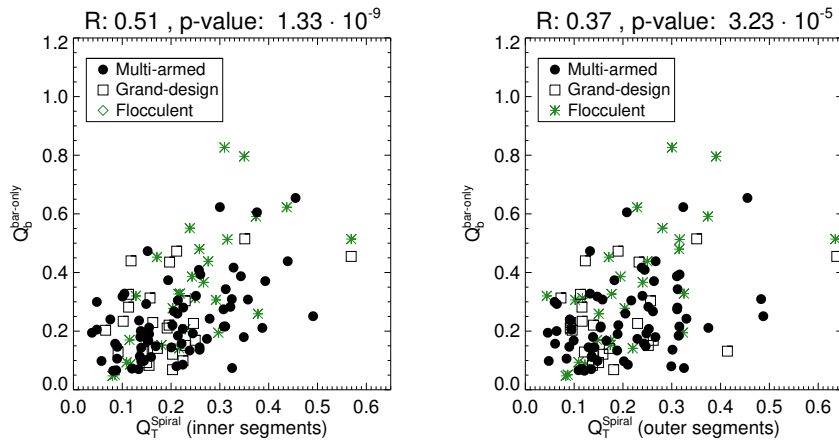


Fig. B.2. As in Fig. B.1, but eliminating the spiral contribution to the bar gravitational torque.

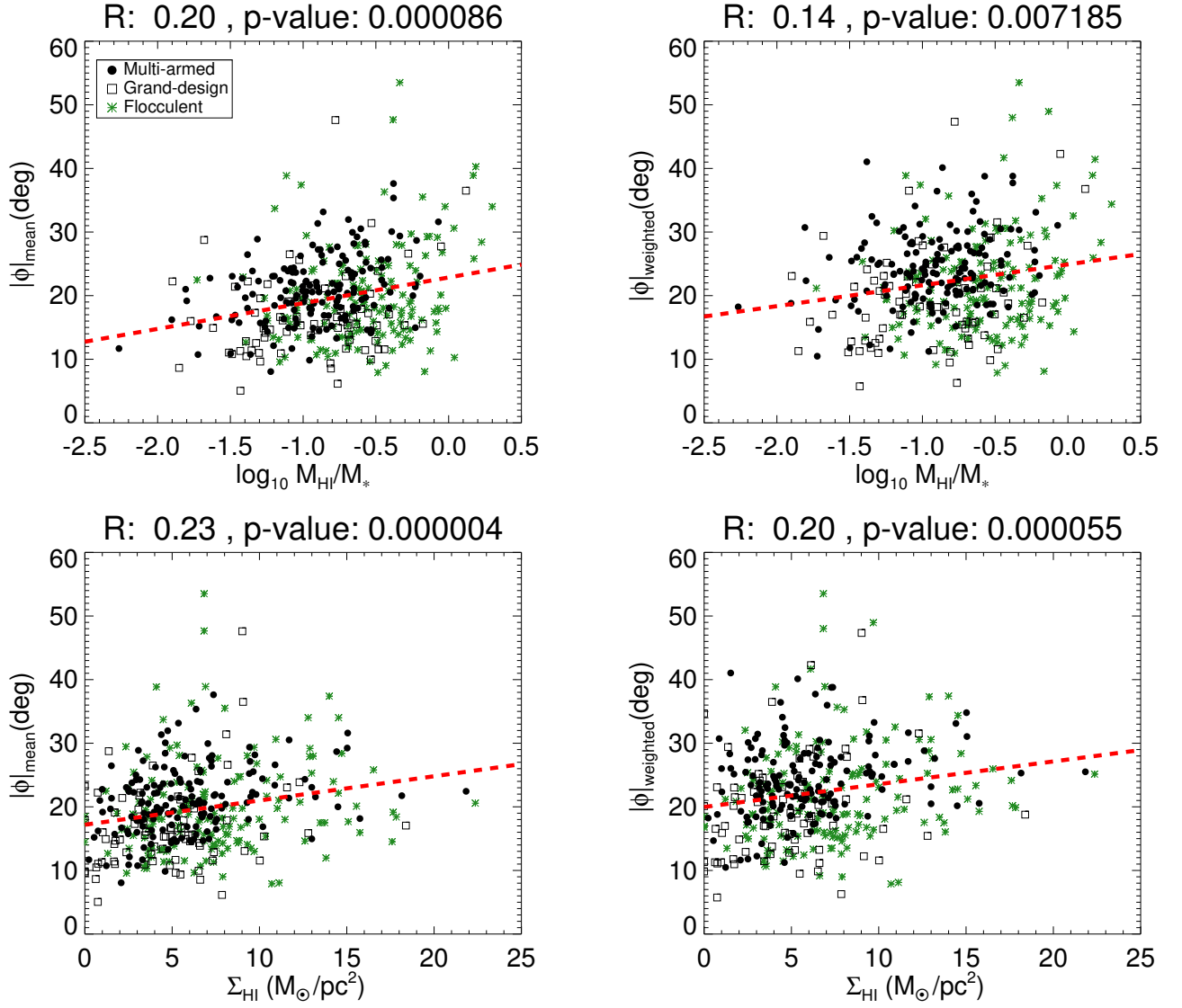


Fig. C.1. Pitch angle versus H I gas fraction (*upper panels*) and H I surface density (*lower panels*) for S⁴G galaxies with inclination < 65°, including barred and non-barred and all types of spirals (multi-armed, flocculent, and grand-design). The Spearman’s correlation coefficient and significance are indicated on top of the plots. Different spiral types are shown with different colours and symbols, as indicated in the legend. The red line shows a linear fit to the cloud of points.

Appendix C: Pitch angle as a function of the relative mass of cold gas

Here we assess a possible dependence between $|\phi|$ and the relative content of gas (e.g. Davis et al. 2015). Atomic gas masses are estimated as (e.g. Giovanelli & Haynes 1988; Erwin 2018):

$$M_{\text{HI}} = 2.356 \cdot 10^5 \cdot D^2 \cdot 10^{0.4 \cdot (17.4 - m_{21c})}, \quad (\text{C.1})$$

where m_{21c} is the corrected 21-cm line flux in magnitude from HyperLEDA, D is the distance to the galaxy (in megaparsecs) adopted by Muñoz-Mateos et al. (2015). H I surface gas densities are obtained as follows:

$$\Sigma_{\text{HI}} = M_{\text{HI}} / (\pi \cdot R_{25.5}^2), \quad (\text{C.2})$$

where $R_{25.5}$ indicates the isophotal radii at the surface brightness 25.5 mag arcsec⁻² in the 3.6 μm images. The pitch angles of the spirals in the S⁴G are weakly correlated with gas fraction or density (Fig. C.1). A slightly tighter trend is seen when we take only multi-armed and grand-design spiral galaxies.

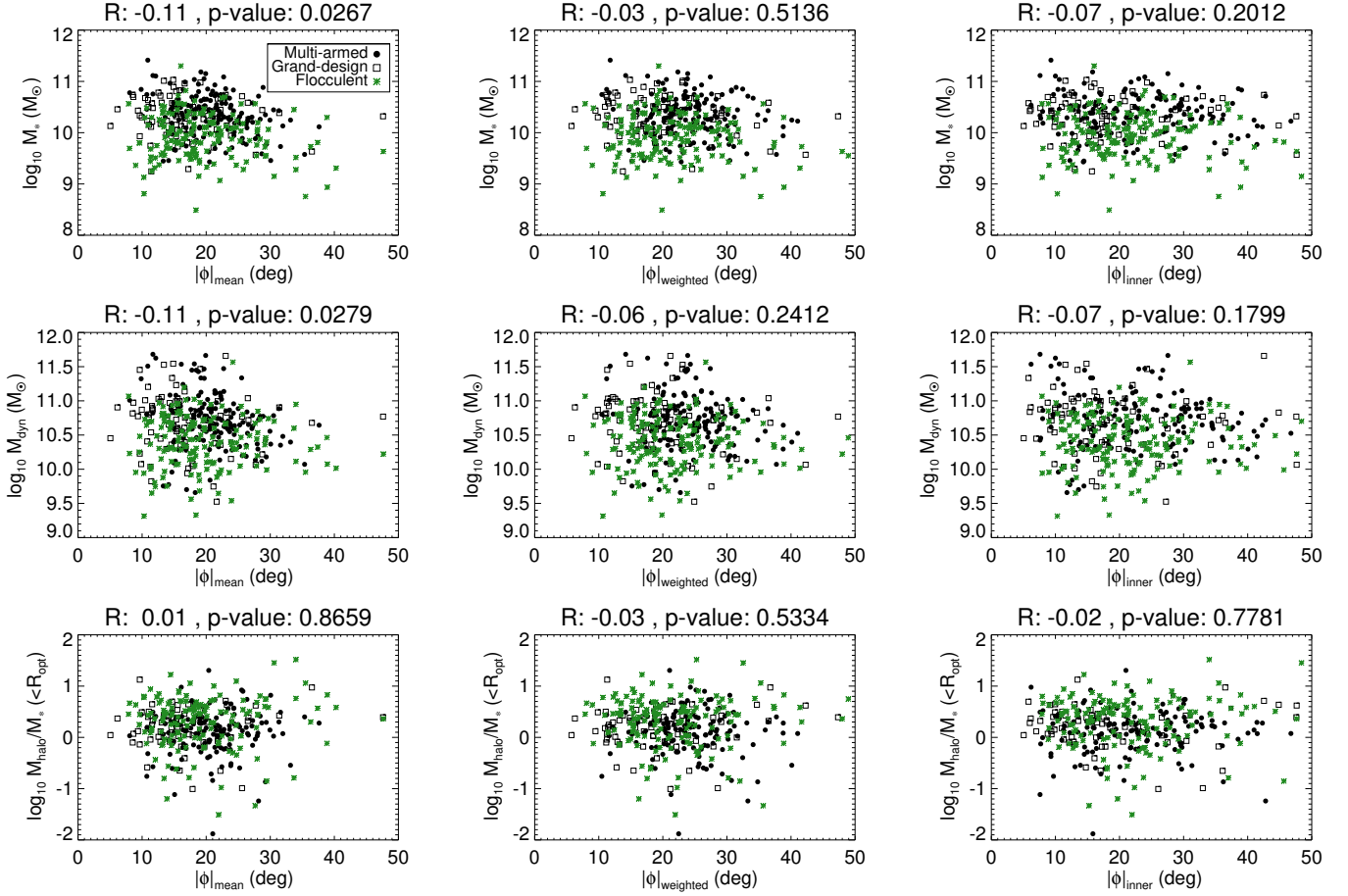


Fig. D.1. Galaxy mass versus pitch angle. We plot the total stellar mass (*upper row*), dynamical mass (*central row*), and halo-to-stellar mass ratio (*lower row*) versus the mean pitch angle (*left column*), mean weighted by the arc length of the arms (*central column*), and mean of the innermost logarithmic segments (*right column*). Different colours and symbols represent different types of spirals, as indicated in the legend of the upper left panel (as in Fig 14).

Appendix D: Pitch angle as a function of galaxy mass

We test a possible dependence of the spiral pitch angle on the total stellar mass of the galaxies, estimated by Muñoz-Mateos et al. (2015), and on dynamical mass (M_{dyn}) and (dark) halo-to-stellar mass ratio (M_{halo}/M_*). Díaz-García et al. (2016b) derived a first-order estimate of M_{halo}/M_* within the optical radius ($R_{\text{opt}} \sim 3.2 \cdot h_R$), which we use here¹³:

$$M_{\text{halo}}/M_*(< R_{\text{opt}}) \approx 1.34 \cdot \left(\frac{(V_{\text{HI}}^{\text{max}})^2}{V_{3.6\mu\text{m}}^2(R_{\text{opt}})} - 1 \right), \quad (\text{D.1})$$

where $V_{\text{HI}}^{\text{max}}$ refers to the inclination-corrected HI velocity amplitude from HyperLEDA and $V_{3.6\mu\text{m}}$ corresponds to the stellar component of the circular velocity (inferred from $3.6 \mu\text{m}$ imaging). We also estimate the dynamical mass within R_{opt} (assuming a spherical mass distribution):

$$M_{\text{dyn}}(< R_{\text{opt}}) \approx \frac{(V_{\text{HI}}^{\text{max}})^2 \cdot R_{\text{opt}}}{G}, \quad (\text{D.2})$$

where G is the Newtonian constant of gravitation.

No dependence of the global spiral pitch angle on total stellar mass, dynamical mass, or halo-to-stellar mass ratio is found in the S⁴G (Fig. D.1). This questions the effect of the global mass distribution in determining the winding angle of the arms (e.g. Kennicutt 1981; Kennicutt & Hodge 1982; Seigar & James 1998b; Seigar et al. 2006; Grand et al. 2013).

¹³ Under the assumption that the halo within the optical disc contributes approximately a constant fraction of the total halo mass ($\sim 4\%$), Díaz-García et al. (2016b,c) found that the trend of the M_{halo}/M_* versus M_* relation agreed with the prediction of ΛCDM models, fitted at $z \approx 0$ based on abundance matching and halo occupation distribution methods (e.g. Moster et al. 2010).

Appendix E: Strength versus pitch angle of spiral segments

In Sect. 7.2 we showed a correlation between the mean pitch and the mean strength of the spirals (see Fig. 17). Here we confirm this dependence when all the individual logarithmic segments (often several per galaxy) are used (Fig. E.1).

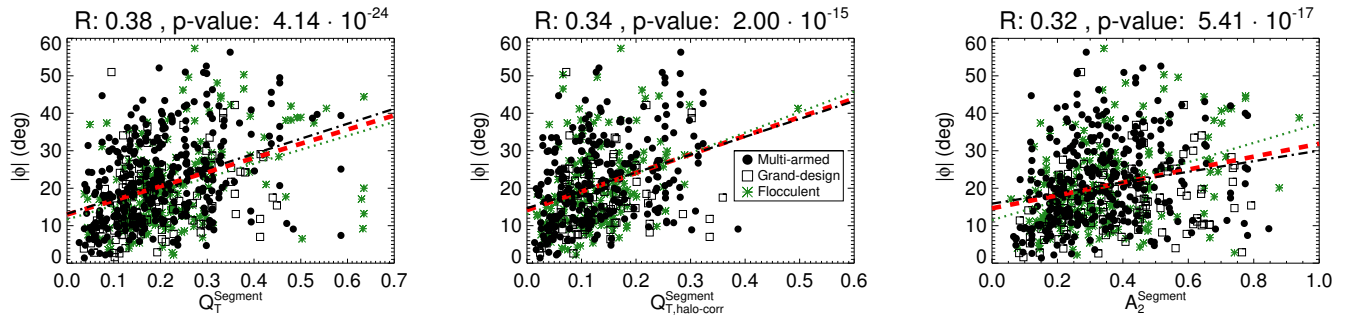


Fig. E.1. As in Fig. 17 but using the strength of all the spiral segments, instead of the mean, and showing also the $m = 2$ Fourier density amplitude of the spirals (*right panel*).

Appendix F: Pitch angle versus shear

We calculate the shear (Γ) from H I and H α rotation curves – $V(r)$ – from the SPARC compilation (Lelli et al. 2016) as follows (e.g. Fujii et al. 2018):

$$\Gamma = -d\ln\Omega/d\ln r, \quad (\text{F.1})$$

where $\Omega = V/r$ is the angular velocity. The shear is obtained for the 17 SPARC galaxies with reliable measurements of the pitch angle in Herrera-Endoqui et al. (2015). Specifically, Γ was calculated in the same radial ranges where $|\phi|$ was fitted, and thus several measurements per galaxy are provided. We do not find any correlation between Γ and $|\phi|$.

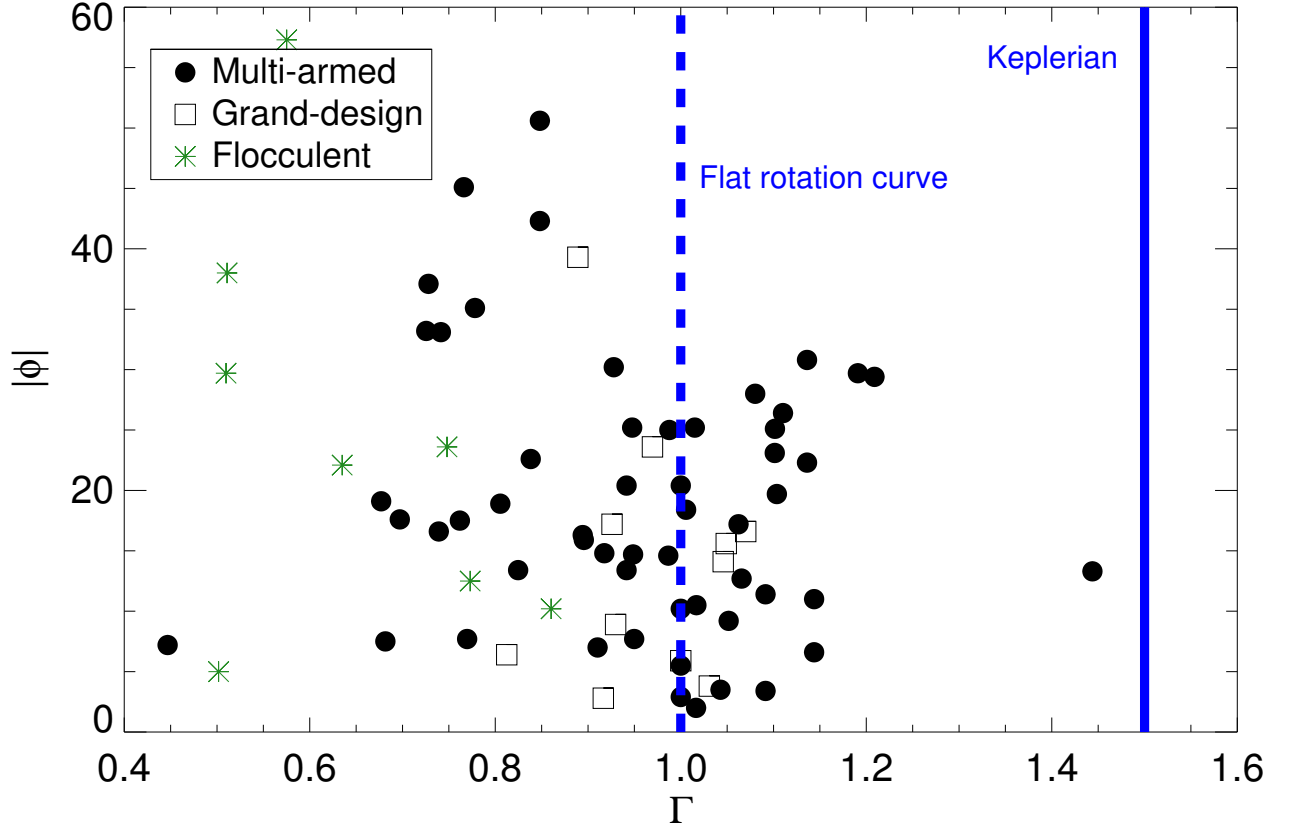


Fig. F.1. Pitch angle versus shear for a sample of 17 galaxies. Every point (72) corresponds to a logarithmic segment. In green we show the flocculent spirals, while black squares and filled circles correspond to grand-design and multi-armed galaxies, respectively (see legend). The dashed (solid) lines show the expected value of Γ for a flat (Keplerian) rotation curve.